ABSTRACT

Title of Dissertation: HIGH PRESSURE DRIVEN EVOLUTION OF CHARGE AND STRUCTURAL ORDER IN NEMATIC SUPERCONDUCTOR, $Ba_{1-x}Sr_xNi_2As_2$

John Califf Collini
Doctor of Philosophy, 2023

Dissertation Directed by: Professors Johnpierre Paglione and Nicholas Butch
Department of Physics

The desire for a complete understanding of high temperature unconventional superconductivity has illustrated a necessity for the study of non-magnetic sources of superconducting enchantment, such as nematically driven fluctuations and charge order fluctuations. $BaNi_2As_2$, a non-magnetic counterpart to high T_c superconductor $BaFe_2As_2$, shows a six-fold superconducting enhancement neighboring charge and nematic orders, positioning it as an excellent candidate for studying the interactions between charge order, nematic order, and enhanced superconductivity. In this thesis, I will present X-ray diffraction and electrical transport evidence for the development of complex charge order within the system as functions of isovalent chemical substitution via $Ba_{1-x}Sr_xNi_2As_2$ and applied hydrostatic pressure. The discovery of three separate charge orders will be detailed: an incommensurate charge order at $Q = 0.28$ and two commensurate charge orders at $Q = 0.33$ and $Q = 0.5$. X-ray diffraction measurements of the $Q = 0.28$ charge order will be used to show a strong correlation between it and a previously established nematic order for $Ba_{1-x}Sr_xNi_2As_2$. Applied pressure of $BaNi_2As_2$ up to 10.4 GPa will detail the development of all three charge

orders and be used to show a correlation between pressure and isovalvent substitution in $BaNi_2As_2$. The critical substitution of 71% Sr and the critical pressure of 9 ± 0.5 GPa will be directly compared by X-ray measurements of their lattice parameters, revealing a collapsed tetragonal phase. This phase is shown to be analogous to the collapsed tetragonal phase of the Fe-pnictide superconductors, likely playing a key role seen at the critical substitution and pressure of $BaNi_2As_2$.

HIGH PRESSURE DRIVEN EVOLUTION OF CHARGE AND STRUCTURAL ORDER IN NEMATIC SUPERCONDUCTOR, $Ba_{1-x}Sr_xNi_2As_2$

by

John Califf Collini

Dissertation submitted to the Faculty of the Graduate School of the
University of Maryland, College Park in partial fulfillment
of the requirements for the degree of
Doctor of Philosophy
2023

Advisory Committee:
Richard L. Green
Jeffery Lynn
Ichiro Takeuchi
Nicholas Butch
Johnpierre Paglione

© Copyright by
John Califf Collini
2023

Foreword

I have contributed to the following works during my time at the University of Maryland. The results of this thesis are largely presented in [1–4] which will be marked here with a dagger †.

Publications

- † *Absence of precursor incommensurate charge order in electronic nematic Ba0.35Sr0.65Ni2As2*. **John Collini**, Sangjun Lee, Stella X.-L. Sun, Chris Eckberg, Daniel Campbell, Peter Abbamonte, Johnpierre Paglione. Physical Review B **106**, 054107 (2022)

- *C-axis transport in UTe2: Evidence of three-dimensional conductivity component*. Yun Suk Eo, Shouzheng Liu, Shanta R. Saha, Hyunsoo Kim, Sheng Ran, Jarryd A. Horn, Halyna Hodovanets, **John Collini**, Tristin Metz, Wesley T. Fuhrman, Andriy H. Nevidomskyy, Jonathan D. Denlinger, Nicholas P. Butch, Michael S. Fuhrer, L. Andrew Wray, and Johnpierre Paglione. Physical Review B . **106**, L060505 (2022)

- *Multicomponent superconducting order parameter in UTe2*. IM Hayes, Di S Wei, T Metz, Jian Zhang, YS Eo, Sheng Ran, SR Saha, **J Collini**, NP Butch, DF Agterberg, A Kapitulnik, J Paglione. Science **373** 6556 (2021)

- *Topologically driven linear magnetoresistance in helimagnetic FeP*. DJ Campbell, **J Collini**, J Sławińska, C Autieri, L Wang, K Wang, B Wilfong, YS Eo, P Neves, D

Graf, EE Rodriguez, NP Butch, M Buongiorno Nardelli, J Paglione. NPJ Quantum Materials. **6** 38 (2021)

- † *Multiple Charge Density Waves and Superconductivity Nucleation at Antiphase Domain Walls in the Nematic Pnictide Ba(1-x)Sr(x)Ni2As2*. Sangjun Lee, **John Collini**, Stella X.-L. Sun, Matteo Mitrano, Xuefei Guo, Chris Eckberg, Johnpierre Paglione, Eduardo Fradkin, and Peter Abbamonte. Physical Review Letter **127**, 027602 (2021)

- *Effect of chemical substitution on the skyrmion phase in Cu2OSeO3*. Paul M Neves, Dustin A Gilbert, Sheng Ran, I-Lin Liu, Shanta Saha, **John Collini**, Markus Bleuel, Johnpierre Paglione, Julie A Borchers, Nicholas P Butch. Physicak Review B **102** 13 (2020)

- *Sixfold enhancement of superconductivity in a tunable electronic nematic system*. Chris Eckberg, Daniel J Campbell, Tristin Metz, **John Collini**, Halyna Hodovanets, Tyler Drye, Peter Zavalij, Morten H Christensen, Rafael M Fernandes, Sangjun Lee, Peter Abbamonte, Jeffrey W Lynn, Johnpierre Paglione. Nature Physics **16** 3 (2019)

- † *Unconventional Charge Density Wave Order in Pnictide Superconductor Ba(Ni1-xCox)2As2*. Sangjun Lee, Gilberto De La Penã, Stella X-L Sun, Matteo Mitrano, Yizhi Fang, Hoyoung Jang, Jun-Sik Lee, Chris Eckberg, Daniel Campbell, **John Collini**, Johnpierre Paglione, FMF De Groot, Peter Abbamonte. Physical Review Letters **122**, 14 (2019)

Manuscripts in progress

- † *Charge Order Evolution of Superconducting $BaNi_2As_2$ Under High Pressure*.

  John Collini, Daniel J. Campbell, Daniel Sneed, Prathum Saraf, Christopher Eckberg, Jason Jeffries, Nicholas Butch, and Johnpierre Paglione

Dedication

This thesis is dedicated to my mother, Hazel M. Collini, who gave and sacrificed countless hours to raising me and supporting me wherever my interests took me. Her love, fiery passion, intellectual curiosity, and persistent drive continues to inspire and guide me. I have never felt alone in my journey thus far, and I never will for the years ahead. Thank you, mom. I love you for always.

March 17 1960 • November 4 2022

Acknowledgments

It takes a village to produce a PhD graduate and I am grateful for all the help and support I have received on my path here. First I would to thank my advisors, Johnpierre Paglione and Nicholas Butch, for their years of support and advisement during my development at the University of Maryland. Through them, I was particularly fortunate to have access to a large array of equipment, opportunity for travel, and scientific support. Thank you Johnpierre for supporting me through particularly challenging efforts of my experiments and for encouraging me to apply for so many traveling fellowships. Thank you Nick for many insightful conversations on my scientific problems and my career development.

My laboratory peers were instrumental in providing support and encouragement over the course of my experiments. I am grateful for the co-supporting relationship I have developed with Prathum Saraf, who started in this program at the same time as me. Daniel Campbell, who mentored me as a graduate student and then later as a post doc during my travels to Lawrence Livermore National Laboratory. Corey Frank and Silvia Lewin, post docs of Nick's group, who provided me many hours of conversation and teamwork on experiments and life advise. Christopher Eckberg, a previous graduate student, who mentored me and layed the scientific foundations for much of the work in this thesis.

During my travels I have cultivated a variety of experiences that have shaped me greatly as a scientist. The summer undergraduate program at the NIST Center of Nuetron

Research with Julie Borchers, committee member Jeffry Lynn, and my advisor Steve Disseler was particularly instrumental in cementing my inspiration to pursue experimental condensed matter physics research, and, heavily influenced my decision to apply to University of Maryland. My travels to University of Illinois at Urbana-Champaign at Peter Abbamonte's lab informed a great deal of my scattering knowledge thanks to support from the students there, Sangjun Lee and Stella Sun. I also want to thank Jason Jeffries of Lawrence Livermore National Laboratory for hosting me in his lab for many months and Daniel Sneed and Daniel Campbell for teaching me the ways of diamond anvil pressure work.

These accomplishments would not be possible if not for support from outside the lab as well. I'm eternally grateful to my parents, Hazel and John, for supporting and pushing me to be the best I can be. Despite neither one of them being a scientist or a college graduate, they have unconditionally supported me and loved me throughout this process. I also thank my partner, Rowan Tanner, for believing in me, supporting me, giving me great joy, and loving me throughout the last years of my program. Lastly, I need to thank the DC west coast swing community at large for being my home away from the laboratory. Having a community and hobby outside the lab with so many supporting people has made my adventure through graduate school possible.

Table of Contents

List of Tables

List of Figures

List of Abbreviations

CDW	Charge Density Wave
SDW	spin density wave
EPC	electron-phonon coupling
IC-CDW	incommensurate charge density wave at Q_{tet}=0.27 in $Ba_{1-x}Sr_xNi_2As_2$
C-CDW1	commensurate charge density wave at Q_{tri}=0.33 in $Ba_{1-x}Sr_xNi_2As_2$
C-CDW2	commensurate charge density wave at Q_{tri}=0.5 in $Ba_{1-x}Sr_xNi_2As_2$
QMC	Quantum Materials Center at University of Maryland, College Park
UIUC	University of Illinois at Urbana-Champaign
EPEC	Equilibrium Physics at Extreme Conditions
APS	Advanced Photon Source at Argone National Laboratory
ICAM	Institute for Complex Adaptive Matter
DAC	Diamond Anvil Cell
PPMS	Physics Property Measurement System
T_c	Superconducting transition temperature
r.l.u	reciprocal lattice units
CT	collapsed tetragonal phase

Chapter 1: Introduction

1.1 Superconductivity

Superconductivity was first discovered by cryogenics pioneer Heike Kamerlingh Onnes in 1911 while investigating the low temperature resistance of pure mercury [5]. He observed a sudden drop in electrical resistance from a finite value to zero upon cooling through 4.2 K, the superconducting transition (T_c) temperature for mercury. In the years to follow, superconductivity would continue to be found in many more elements and compounds at low temperatures. It was found through further study that superconductivity has three unique properties: zero resistance, the ability to expel magnetic fields (the Meissner effect) [6], and macroscopic quantum coherence. All three of these characteristics show extraordinary technological promise and invite significant fundamental physical research. However more than 100 years later, we have yet to see a technological leap inspired by superconductivity primarily because all known superconductor transition temperatures are well below room temperature at ambient pressures.

The desire for both high temperature superconductivity and a complete understanding of superconductivity has inspired a century's long study into new superconductors and their underlying mechanisms. Notable to these efforts are the 1957 works of John Bardeen, Leon Cooper, and Robert Shrieffer, whose microscopic theory of superconductivity successfully

explained the behavior for the vast majority of known superconductors at the time [7]. Following this theory in 1986, a particularly notable discovery of superconductivity was discovered in a class of copper-oxide "cuprate" compounds [8], which would later show significantly higher transition temperatures than all previously discovered superconductors. Crucially, some of these cuprate superconducting transition temperatures reached above 77 K, the liquid nitrogen boiling point, granting superconductivity a new level of technological accessibility. Not long after their discovery was it found that the mechanism responsible for the cuprate's superconducting phase was distinctly different than all previously known superconductors. This spurred a widespread investigation into it's superconducting mechanism that continues to this day. Cuprates would stand alone as the only materials class capable of high T_c superconductors until 2008 with the discovery of high temperature superconductivity in the iron-pnictides [9]. As with the cuprate class of superconductors, it was also found that the iron-pnictide possess a superconducting mechanism differing from the conventional mechanism seen in many low temperature superconductors. The discovery and widespread study of these unconventional superconducting classes have indicated that our understanding of superconductivity remains incomplete. Such gaps in knowledge have helped inspire the bevy of works found in quantum materials research pertaining to the study of new exotic superconductors and other exotic quantum materials.

This thesis aims to shed light on the particular case of a nickel-pnictide superconductor, $BaNi_2As_2$, a non-magnetic conventional superconductor with unconventional superconductivity enhancement from neighboring charge ordered and nematically ordered phases. The remainder of this chapter will continue with an introduction to superconductivity followed by introductions to charge density waves, nematicity, and an outline to the remaining

chapters of this thesis.

1.1.1 BCS Theory and Conventional Superconductivity

From the time of superconductivity discovery to the mid 1900s, researches remained in the dark on the microscopic origins of superconductivity. These origins were first illuminated by John Bardeen, Leon Cooper, and Robert Shrieffer (BCS) in 1957. The following is a simple and brief introduction to their results, as well as, their immediate applications to conventional superconductivity. These results are presented for the purposes of illuminating the few superconducting measurements in this work. Treatment discussed below of BCS theory is inspired by Tinkham [10], where a a detailed derivation can be found.

We begin by noting the macroscopic experimental evidence on superconductivity up until the mid 1900s that motivated BCS theory. Measurements in electrical transport of course note the rapid transition into a zero resistance state at T_c. Heat capacity is shown to have a discontinuous jump at T_c followed by an exponential decay, implying the presence of an energy gap in the superconducting state that narrows and eventually closes at T_c. Measurements in field noted a critical field at which the superconducting state would vanish. Magnetic field penetration studies demonstrated an exponential decay of field into the bulk superconductors, which was argued to require long range quantum coherence. The microscopic BCS theory therefore needed to satisfy zero resistance, determine an energy gap, explain the specific heat jump at T_c, exponentially screen magnetic fields, find the critical field, and include long range quantum coherence.

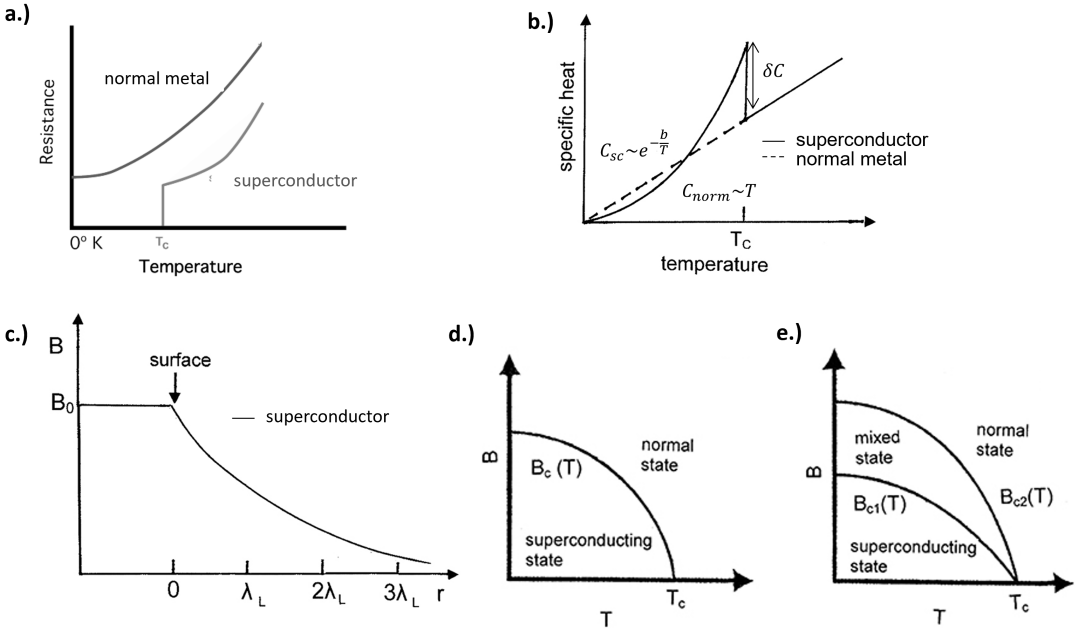

Figure 1.1: Idealized characteristic measurements and diagrams for conventional superconductivity. **a.)** resistance at low temperatures for a normal metal and a superconductor with a superconducting transition at T_c. **b.)** Specific heat as a function of temperature for a superconductor and a normal metal. **c.)** Magnetic field strength penetration decay into a superconductor with a natural decay rate, $_L$, otherwise known as London penetration depth. **d.)** and **e.)** Magnetic field vs temperature phase diagrams for a type I and type II superconductor respectively. Type I shows an upper critical field $B_c(T)$ and type II shows separate critical fields of $B_{c1}(T)$ and $B_{c2}(T)$. Figures have been adapted from [11, 12].

BCS theory stems from a few starting assumptions and demonstrations. First in the development of electron pairs near the Fermi level, E_f, experiencing an attractive potential, $V_{k,k'}$ with momentum $\mathbf{k}$ and $\mathbf{k}'$. Only electrons within a small energy range, $E_c = \hbar\omega_c$ are chosen to experience the attractive potential, $V_{k,k'}$. Cooper had shown that the formation of such pairs is unstable at the Fermi surface and a great number of generated pairs would open a gap. Each pair is also given zero net momentum, assigning the individual momenta as $\mathbf{k}$ and $-\mathbf{k}$, as well as, opposing spins to form a singlet pair. In the limit of weak interaction (small V present for states within a narrow energy range of $\hbar\omega_c$), the energy of a pair is given as,

$$E = 2E_f - 2\hbar\omega_c e^{\frac{-2}{N(0)V}} \tag{1.1}$$

where $N(0)$ is the electronic density of states at E_f. Because this energy is lower than the normal state energy of two independent electrons, $2E_f$, the state is energetically favorable.

Solving the system of many pairs gives an equation for energy gap in the superconducting state,

$$\Delta = 2\hbar\omega_c e^{\frac{-1}{N(0)V}} \tag{1.2}$$

The energy gap can be shown to be directly related to T_c for this weakly interacting limit as,

$$\frac{\Delta}{k_B T_c} = 1.764 \tag{1.3}$$

The temperature dependence of Δ remains mostly constant until the temperature begins to approach T_c. This can be approximately modeled as,

$$\Delta(T) \approx 1.74(1 - \frac{T}{T_c})^{1/2}\Delta(0) \tag{1.4}$$

Interestingly, the gap is not found to be a function of $\mathbf{k}$, implying the gap is symmetric on the Fermi surface.

From solving the gap as a function of temperature, the fermionic excitation energies can be determined and used to find entropy, and therefore, specific heat. BCS theory succeeds in finding the experimentally measured discontinuity for specific heat at T_c, noting the gap size, δC, correctly as,

$$\delta C = 1.43 C_{norm}(T_c) = 1.43(\frac{2\pi^2}{3} N(0) k_B^2 T_c) \tag{1.5}$$

where C_{norm} is the normal state electronic specific heat of a metal above T_c. Below the transition temperature, BCS also correctly guesses the low temperature exponential form of C as,

$$C(T) \propto e^{\frac{-2\Delta(0)}{k_B T}} \tag{1.6}$$

BCS theory is able to make strong predictions about the characteristics of superconductors based upon the assumption of a present interaction potential, $\mathbf{V}_{\mathbf{k},\mathbf{k}'}$ but it is not specific

about that interaction's origin. For many of the superconductors discovered at this time, that interaction is rooted in the exchange of phonons. Assuming the weak coupling limits of BSC theory, equations 1.2 and 1.3 can be combined to show

$$k_B T_c = 1.13 \hbar \omega_D e^{\frac{-1}{\lambda}} \tag{1.7}$$

where ω_D is the Debye frequency for a given superconducting material and λ is a constant related to the strength of the electron-phonon coupling and the electronic density of states.

The combination of BCS theory and the introduction of an electron-phonon coupling interaction makes up conventional superconductivity. The core makeup of such superconductors are: a symmetric superconducting gap independent of $\mathbf{k}$ on the Fermi surface (i.e. s-wave), spin singlet pairing, a specific heat modeled via equations 1.5 and 1.6, and phonon mediated pairs with a relationship governed by equation 1.7.

1.1.2 Unconventional and High Temperature Superconductivity

As successful as the conventional superconductor model of phonon mediated pairing was for many early discovered superconductors, there would come classes of superconductors later that would show significantly different behavior. These classes would include the cuprates, iron-pnictides, heavy fermions, Sr_2RuO_4, UTe_2, and topological superconductors to name some. This section will focus on the behaviors of the cuprates and iron-pnitcides as their physics will provide the best point of comparison to $BaNi_2As_2$.

Both the curprates and iron-pnictides are magnetic and non-superconducting compounds

in their unperturbed states. However, both are capable of high temperature superconductivity (with transition temperatures sometimes reaching above liquid N_2) through chemical substitution and applied pressure. Such perturbations reveal incredibly complex phase diagrams including magnetic order, charge order (in the cuprates), nematicity (in the iron-pnictides), and more in addition to the aforementioned high temperature superconducting phases (Figure 1.2).

The high transition temperatures of these compounds cannot be solely attributed to phonon mediated pairing. Measurements of the electron-phonon coupling strength in the iron-pnictides predict a T_c that is tens of times smaller than the experimentally measured results [15, 16]. However, measurements of the isotope effect in the iron-pniticdes indicates that phonon-meditation may be playing at least a partial role in pairing [17]. In the cuprates, the picture becomes more complicated with many competing theories and measurements ranging from electron-phonon coupling not being strong enough [18–20], actively working against pairing [21, 22], a key contributing factor in pairing [23–25], or possibly part of a new phonon-spin-charge interaction model rather than the conventional BCS model [26–28]. While conventional electron-phonon interactions cannot completely explain these superconducting phases, they cannot be completely disregarded either.

Additional evidence for the unconventional pairing mechanisms in the cuprates and iron-pnictides can be found in their phase diagrams (Figure 1.2). Through the perturbations of chemical substitution and applied pressure, long range magnetic order in these compounds becomes suppressed towards a zero temperature quantum critical point. It is about this magnetic quantum critical point that we find superconductivity emerges and becomes

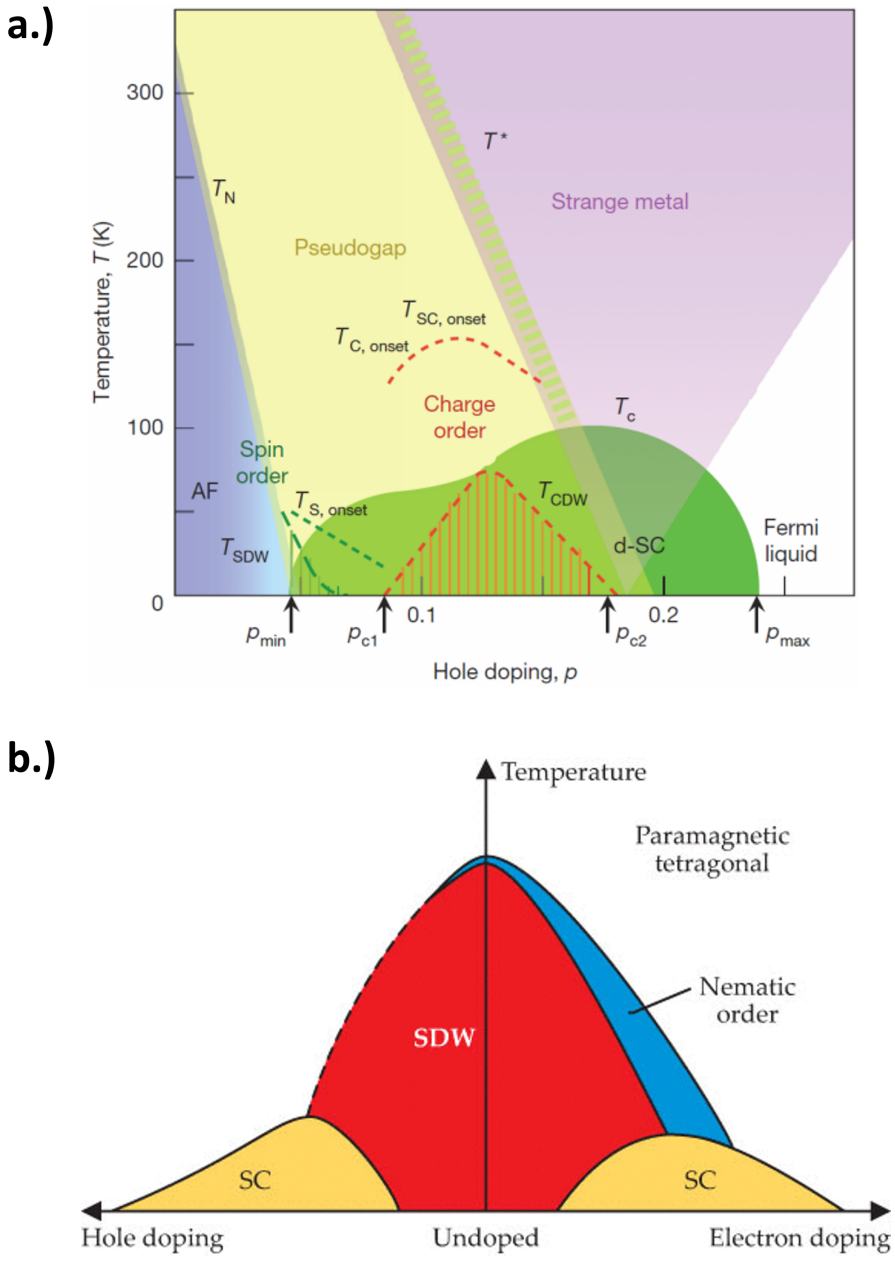

Figure 1.2: Generic phase diagrams for the cuprates [13] and the iron-pnictide [14] systems.

maximized. It has been suggested from their phase diagrams and many experimental probes that magnetic excitations play a key role in their pairing. A particularly strong piece of experimental evidence for this comes from the observation of a linear correlation between T_c and magnetic excitation energies taken from inelastic neutron scattering on the cuprates and iron-pntictdies [29,30]. This phenomena of high temperature superconductivity within close proximity of magnetism is quite surprising when remembering that superconductivity is generally at odds with magnetism.

The phase diagrams of the cuprates additionally suggest charge ordering as a possible influence on the superconducting pairing mechanism. Likewise for the iron-pnitices, nematicity also could play a role on it's superconducting pairing mechanism. Theoretical work has demonstrated that fluctuations associated with an electronically nematic quantum critical phase can enhance superconducting phases with few requirements [31,32]. Directly examining the role of these electronic interactions on the pairing mechanisms within these compounds becomes challenging when considering the close proximity to the magnetic phases, as well as, the high upper critical fields of 10's and sometimes 100's of Telsas needed to suppress the superconducting phases in the iron-pnictides and cuprates respectively.

The subject of this study, $BaNi_2As_2$, is a superconductor that has shown unconventionally strong superconducting enhancement within proximity to charge order and nematicity without any detected magnetism, making it an excellent candidate for studying the possibility of charge order and nematic driven pairing enhancement. Introductions to both charge ordering and nematicity will be given in the upcoming sections. An introduction to $BaNi_2As_2$ will be presented in Chapter 3.

1.2 Charge Order

The observation and manipulation of charge order via charge density waves (CDW) played a critical role in my studies of $BaNi_2As_2$. This chapter aims to provide a modern introduction to charge density waves for the reader. This introduction is inspired by the reviews and works of refs [33–37].

1.2.1 Introduction and the Peierls Transition

Broadly, a charge density wave is a periodic reconstruction of the electron density within a crystal that differs from the periodicity of the underlying lattice. Sometimes CDWs will also accompany a periodic distortion of the atomic lattice. There are a few known mechanisms responsible for producing CDWs with more mechanisms remaining unknown that will be describing in the following sections.

One of the simplest CDW producing mechanism to understand is a method first theorized by Peierls in his book, *Quantum Theory of Solids* [38] (Figure 1.3). First, take a one dimensional chain of N atoms spaced a distance apart filled to a Fermi momentum, k_f. The band energy of the system can be described by a tight binding energy, $E(k)$, and by a periodic electron density that peaks at each atomic center [33, 35–37, 39]. Peierls theorized that the total energy of the system could be further lowered by introducing a periodic lattice distortion. This distortion sees each atom moving closer to one neighbor and further away from another neighbor in an alternating periodic fashion (Figure 1.3 gray panel). This distortion causes the electron density periodicity to double, earning the phase it's name of charge density wave. The introduction of this distortion lowers the overall

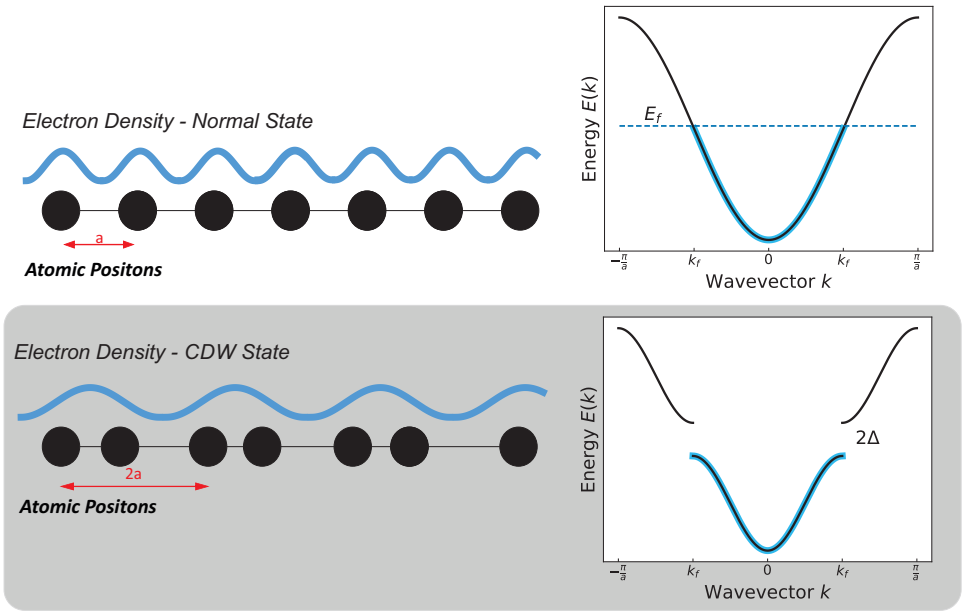

Figure 1.3: Illustration showing the occurrence of Peierls type charge density wave on a one dimensional toy model. In the normal state, a crystal is represented by a one dimensional chain of atoms all separated by a distance a. The electronic band structure is described by a tight binding model with one electron per site, placing the Fermi energy level, E_f, halfway to the maximum and intersecting points in k space at $k_f = \pm\pi/2a$. Electron density is slightly peaked at each atomic position. When the charge density wave state is entered (gray panel), several physical changes from the normal state occur. A structural distortion onsets, slightly moving each atom periodically close to one neighbor and further away from another, creating a new periodicity in the system of $2a$. A gap is opened at E_f, creating an overall energy savings relative to the normal state and inducing a metal insulator transition. The electron density reacts to the structural distortion by creating a new larger periodicity relative to the normal state (a superstructure) at a wavevector of $2k_f$, nesting the gap formed in the electronic structure.

system energy by introducing a gap at the Fermi energy. Here the electrons closest to the Fermi energy have "folded over" yielding a lower energy compared to the previous normal state. This gap formed therefore predicts that Peierls CDWs have a metal-insulator (or potentially, a metal-semiconductor) transition accompanying them. Additionally, the atomic lattice and electron density develop a new periodicity of $2a$ in real space with an associated Q_{CDW} vector, $Q_{CDW} = 2k_f = \pi/a$, which also connects the energy gap points formed in momentum space. This phenomenon is otherwise known as "Fermi nesting", in which the Q_{CDW} formed by the new state neatly connects the gap points created on the Fermi surface (or, Fermi "line" for this 1D example). A Peierls-like CDW may form in real materials if the energy savings of entering the CDW state overcome the energy cost needed to reconstruct the atoms and electron density below some transition temperature, and if the Fermi surface geometries are favorable for nesting at Q_{CDW}. The temperature at which this transition into a CDW state occurs will be denoted in this work as T_{CDW}.

1.2.2 Kohn Anomaly

An additional effect also occurs in the Q-dependent phonon spectra for Peierls transitions known as the Kohn anomaly. As the temperature is lowered towards T_{CDW}, all phonon energies at Q_{CDW} begin to decay to zero. These phonons hit zero energy at T_{CDW} and below this point become imaginary, indicating a static reconstruction of the lattice has occurred as a result of a CDW phase. Kohn anomaly also acts as indication of the strength of electron-phonon coupling strength associated with the CDW [33]. An idealized example and a real material example of Kohn anomaly can be seen in Figure

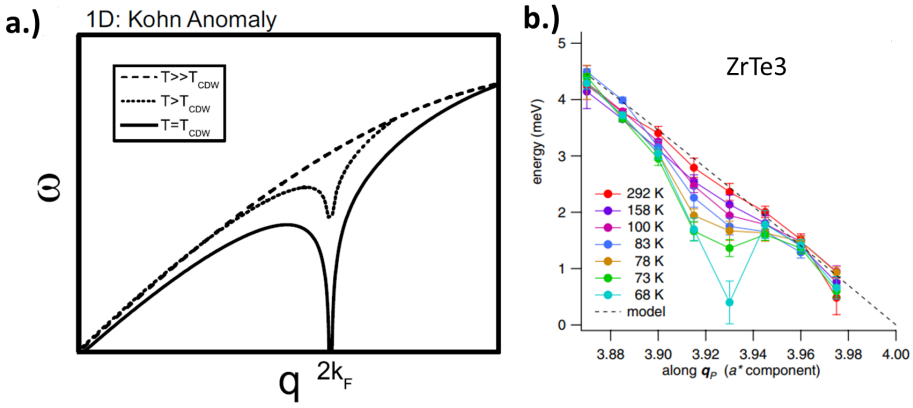

Figure 1.4: **a.)** A one dimensional idealized picture of Kohn anomaly for a CDW. This example normal state Q dependent phonon spectra (thick dashed lines) is shown at higher temperatures. As temperature is lowered towards T_{CDW} (think dashed lines), the spectra begins to dip centered on $Q_{CDW} = 2k_f$. When T_{CDW} is reached (solid line), the spectra has sharply dipped and reached zero energy at $2k_f$. This example plot is borrowed from ref [34]. **b.)** A real example of Kohn anomaly as observed in $ZrTe_3$ ($T_{CDW} = 63$ K) via inelastic x-ray scattering [40]. At room temperature, a slight dip can already be observed at $2k_f$. As temperature is lowered towards T_{CDW}, the phonon softening becomes more pronounced.

1.4.

1.2.3 Charge Density Wave Characterization

To properly characterize a CDW, a wide array of experimental techniques must be used. X-ray, neutron, and electron diffraction are used to determine the Q_{CDW} and T_{CDW}. Electrical transport can also sometimes determine the T_{CDW}, as well as, the associated metal-insulator transition (if it exists). Angle resolved photoemission spectroscopy (ARPES) is used to determine the band structure and view the Fermi surface contours. Scanning tunnel microscopy (STM) and spectroscopy are used to find the wavelength of the charge

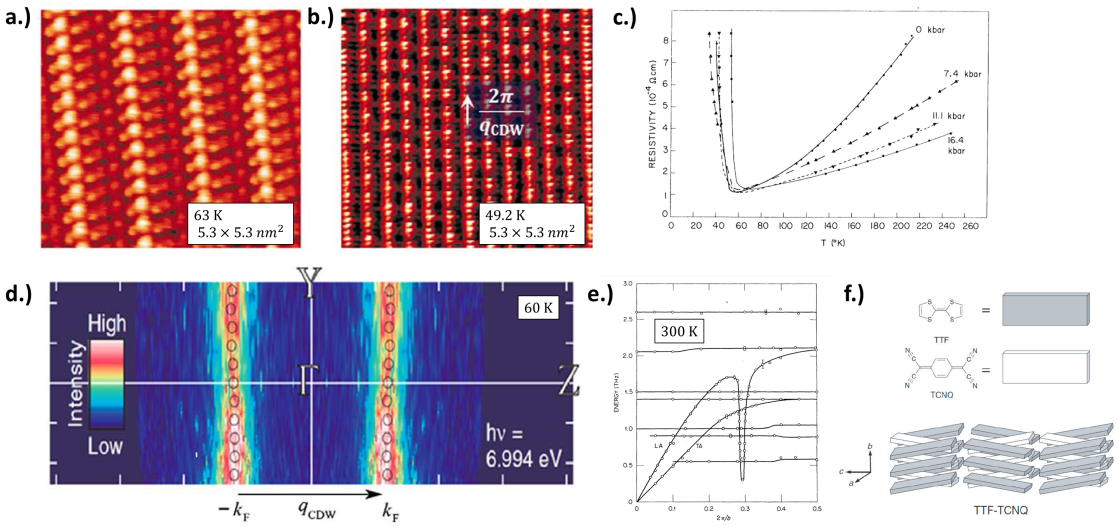

Figure 1.5: Example CDW characterization measurements of TTF-TCNQ ($T_{CDW} = 54$ K). **a.)** and **b.)** STM characterization above and below T_{CDW} [46]. The real space reconstruction of the charge and the lattice in the CDW phase can be seen. **c.)** Resistivity vs temperature measurements at different pressures showing the Peierls metal-insulator transition at T_{CDW} [41]. **d.)** ARPES measurements just above T_{CDW} showing the Fermi surface just before becoming gaped and nested by Q_{CDW} [42]. **e.)** Inelastic nuetron measurements displaying a Kohn anomaly at Q_{CDW} for specifically the longitudinal acoustic (LA) phonon mode [43]. It should be noted upon further review, these measurements were called into question by the authors [44], but are still shown for this thesis for pedagogical completeness. **f.)** The orthorhombic crystal structure of TTF-TCNQ consisting of parallel stacks of the organic compounds TTF and TCNQ along the b axis [45].

modulation and the electronic transition temperature. Inelastic X-ray and neutron scattering can measure the temperature dependence of the phonon dispersion needed for Kohn anomaly. A series of example CDW characterization measurements for a real Peierls material, Tetrathiofulvalinium Tetracyanoquinodimethane (TTF-TCNQ) ($T_{CDW} = 54$ K), is shown in Figure 1.5 [34, 41–45].

Determination of Q_{CDW} can be performed using X-ray or electron diffraction by

finding CDW induced superstructure peaks in the diffraction pattern at low temperatures when compared to high temperatures. These superstructure peaks appear at fractional Miller indices ($[HKL]$) between neighboring Bragg peaks in what are known as satellites peaks (Miller indices will be expanded upon in Chapter 2.1.2). The fractional value of these satellite peak locations the Q_{CDW}, and therefore the periodicity, of the CDW. As an example, we can examine an electron diffraction study of a CDW material $Dy_5Ir_4Si_{10}$ in Figure 1.6 [47]. In this study, diffraction patterns of $Dy_5Ir_4Si_{10}$ are taken in the b-c plane at a high temperature, 298 K, and low temperature, 100 K. The high temperature diffraction pattern shows the normal state with only the Bragg peaks from the crystalline structure visible. At low temperatures new peaks have formed in-between the Bragg peaks corresponding to the new CDW state. Along the c direction new peaks are seen at 1/4 of the way to the next Bragg peak (such as ($[0, 0, 1/4]$, $[0, 2, 1/4]$, $[0, -2, 1/4]$) and 1/2 of the way to the next Bragg peak. The peaks positioned at 1/4 of the way to the next peak correspond to a CDW at $Q_{CDW} = [0, 0, 1/4]$, meaning that this CDW has a periodicity of 4 unit cells along the c direction when compared to the room temperature crystalline structure. This CDW can be referred to as a commensurate CDW, because its' satellite peaks occurs at a rational fractional values of $[HKL]$, meaning it's periodicity corresponds to an integer multiple of the underlying unit cell periodicity. Incommensurate CDWs are also possible, whose satellite peaks instead occur at irrational fractional values of $[HKL]$, corresponding to a periodicity that is uncorrelated with it's underlying lattice. The peaks positioned at halfway between each Bragg peak correspond to a structural transition that has occurred in $Dy_5Ir_4Si_{10}$ causing a unit cell doubling along the c direction.

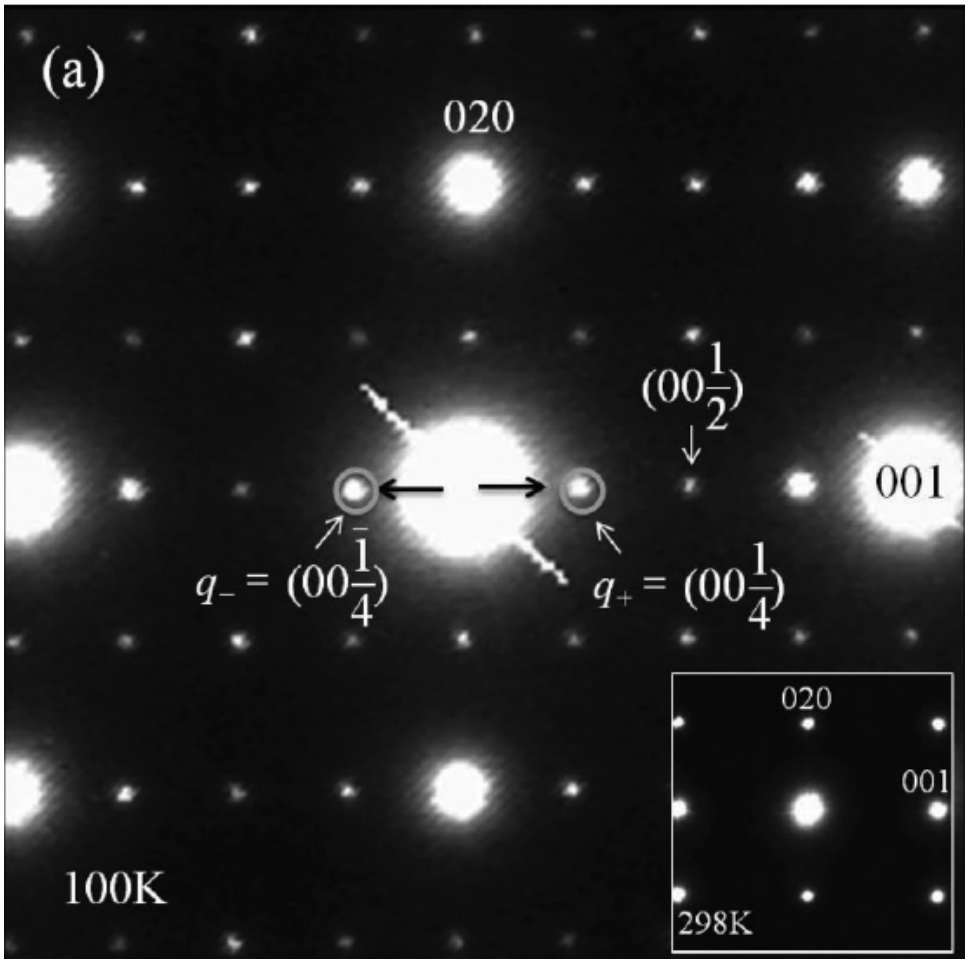

Figure 1.6: Electron diffraction patterns of $Dy_5Ir_4Si_{10}$ taken at 100 K and 298 K (Insert) [47].

1.2.4 Types of Charge Density Waves

Recent studies have challenged the Peierls picture for the origin of CDWs in a majority of real materials, noting that many studied CDW materials do not experience key Peierls CDW features, such transition metal dichalcogenides $NbSe_2$, $TaSe_2$, and $CeTe_3$. As an example, ARPES measurements of the $NbSe_2$ Fermi surface do not show Q_{CDW} properly nested within it. A Kohn anomaly does occur, however, the phonon softening occurs over a vastly larger range of Q space than what is expected for Peierls transitions. Additionally, and resistivity vs temperature measurements do not show much change at T_{CDW}, indicating no metal-insulator transition has occurred [33, 37] (Figure 1.7).

Instead, it would seem features in the Q dependent electron-phonon coupling (EPC) are a stronger determining factor for the origin of CDWs in many real materials rather than a Peierls transition. Direct measurements of the electron-phonon coupling matrix $|g(\mathbf{Q})|^2$ are presently not possible. However, the strength of the electron-phonon interaction as a function Q can be inferred from measurements of the phonon energies, phonon linewdiths, and quasiparticle interactions [33, 34, 48–52]. For these types of EPC driven CDWs, one should expect a large response in the phonon energies and linewdiths with no direct relationship to nesting.

This divergent view of many CDWs separated from the Peierls picture and instead focused on Q dependent EPC is rather new as of the writing of this thesis. As such, there does not yet appear to be a standard method by which one would measure and quantify the relationship of a CDW to the EPC mechanism. While Zhu [33, 34] does offer ways to approximately calculate the EPC matrix element, $|g(\mathbf{Q})|^2$, from experimental

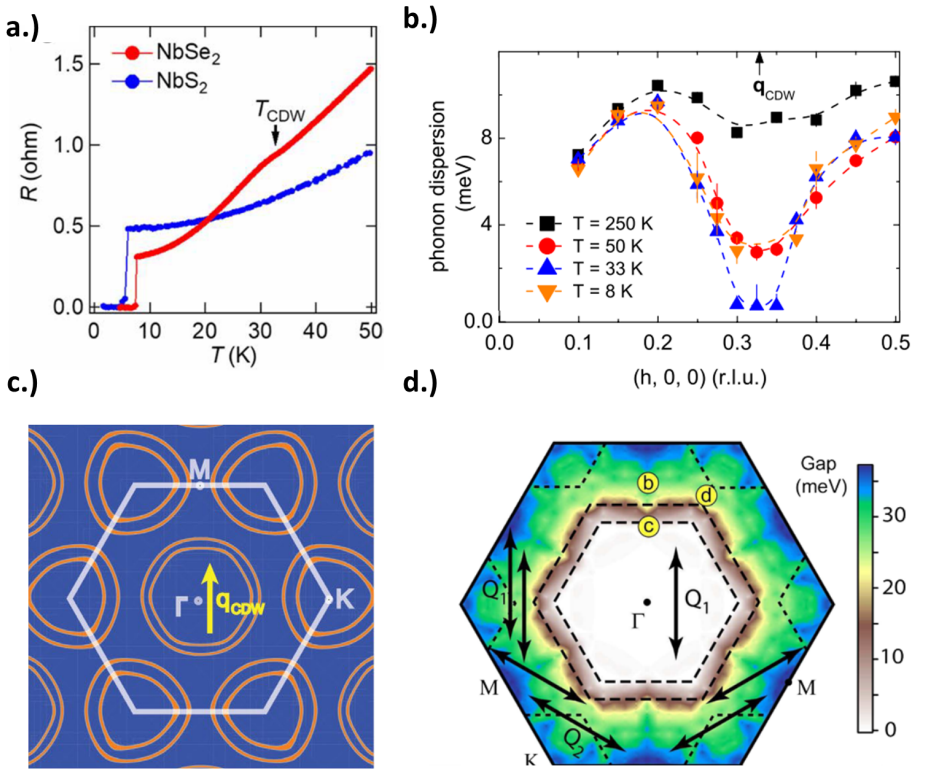

Figure 1.7: Measurements probing the NbSe2 CDW. **a.)** Low temperature resistance showing a small anomaly at T_{CDW} as well as, a superconducting transition [53]. **b.)** Phonon energies about Q_{CDW} [48]. **c.)** and **d.)** ARPES measurements showing the lack of Fermi surface nesting and gapping related to Q_{CDW} [33, 34, 49].

measurements of the phonon linewidths and energies, such methods have not been widely adopted. In the literature, each author studying a CDW material dependent on a EPC mechanism shows evidence for their claims using different measurements and calculations. Such examples would be wide Kohn anomalies and phonon linewidths [33, 34, 48], peaks in the photoemission spectra [54], and in some cases, phonon energies hardening instead of softening at Q_{CDW} [55]. As the interest continues to build for CDW materials, a need presents itself for a matured methodology and language for measuring and discussing Q dependent EPC driven CDW phases.

CDWs have also been detected in the high T_c family of cuprates where they are believed to be at competition with the superconducting phase. The mechanisms for charge ordering in the cuprates further stray from both the Peierls picture and the EPC picture [34]. In this high T_c family, several different forms of charge ordering have been detected, such as a stripe phase in $La_{1.6-x}Nd_{0.4}Sr_xCuO$ [56, 57], a checkerboard phase in $Bi_2Sr_2CaCu_2O_{8+\delta}$ [58, 59], and long ranged CDWs in $YBa_2Cu_3O_{6+x}$ [60]. Comin et al. have shown that FSN cannot be the driving force behind charge order in the cuprates [61]. Zhu et al. have also shown that EPC in the cuprates is not strong enough to drive a Kohn anomaly or charge order [33]. It therefore becomes clear here that charge ordering in the cuprates is derived from neither Fermi Surface Nesting (FSN) or EPC. STM studies [62] have shown instead that these charge ordered phases are unconventional, in that they are more likely driven by antiferromagnetic and Coulombic interactions.

Thus, we can categorize CDWs into three types based on their underlying mechanisms [33,34]. Type I being Peierls-like CDWs, which usually materialize in quasi-one dimensional systems. Type II being EPC driven CDWs, with no strong ties to Fermi surface nesting

and are unrelated to metal-insulator transitions, such as in $NbSe_2$, $TaSe_2$, $CeTe_3$. Type III are unconventional CDWs with no clear Peierls or EPC signatures, such as in the Curprates. Discussion on which type $BaNi_2As_2$ charge order is will occur in Chapter 5

1.3 Electronic Nematicity

New measurements in electronic nematicity are not included in this thesis. However, an understanding of basic nematicity is critical to understanding the impact of the research presented. Here, I will give a brief introduction to electronic nematic susceptibility and electronic nematic order tailored to understanding the physics at play in $BaNi_2As_2$.

A nematic transition is one that breaks rotational symmetry. Important to the discussion to rotational symmetry breaking is the mathematical formalism of point groups. These groups are sets of mathematical operations that map one space to another space that keep a single point fixed that obey the axioms of closure, invertibility, identity, and associativity. Within the application of real materials, these point groups are used to describe the set of operations, such as rotations and reflections, upon a single molecule or unit cell that preserves the original locations of the atoms present. Common ways to examine the characteristics of a point group are through a multiplication table and a character table. As an example, we can examine the C_{2v} point group multiplication table and character table, representative of the H_2O molecule.

The elements used in the C_{2v} point group include E, the identity, C_2, a 180 degree rotation, and σ_{ab}, the reflections, about a given ab plane (Figure 1.8). All of these operations represent a complete group of symmetries for the H_2O molecule. A set of

Table 1.1: C_{2V} Multiplication Table

C_{2v}	E	C_2	σ_{xz}	σ_{yz}
E	E	C_2	σ_{xz}	σ_{yz}
C_2	C_2	E	σ_{yz}	σ_{xz}
σ_{xz}	σ_{xz}	σ_{yz}	E	C_2
σ_{yz}	σ_{yz}	σ_{xz}	C_2	E

irreducible representations can be calculated from this table, representing a basis set of the group. These irreducible representations of a given point group are well known and described by a character table.

Table 1.2: C_{2V} Character Table

Γ_i	E	C_2	σ_{xz}	σ_{yz}	
A_2	1	1	1	1	x^2, y^2, z^2
A_2	1	1	-1	-1	xy
B_1	1	-1	1	-1	xz
B_2	1	-1	-1	1	yz

Here, each symbol in the left most column is a name for each irreducible representations, Γ_i of C_{2v} while the following columns represent the different elements of C_{2v}. The far most right column shows the functional form of that irreducible representation. Each irreducible representation for C_{2v} is able to represent a vibrational mode, translational mode, or rotational mode of H_2O with the shape of each mode matching the functional form of it's given representation and can be detected in infrared or Raman spectroscopy.

$BaNi_2As_2$ has a tetragonal unit cell structure, meaning, $a = b \neq c$ and $\alpha = \beta = \gamma = 90$. More specifically, it's belongs to the $ThCr_2Si_2$-type crystal structure family (Figure 3.1). The point group associated with $BaNi_2As_2$ is D_{4h}, representing an inversion symmetric tetragonal system. This point group has 16 unique operations, including, the

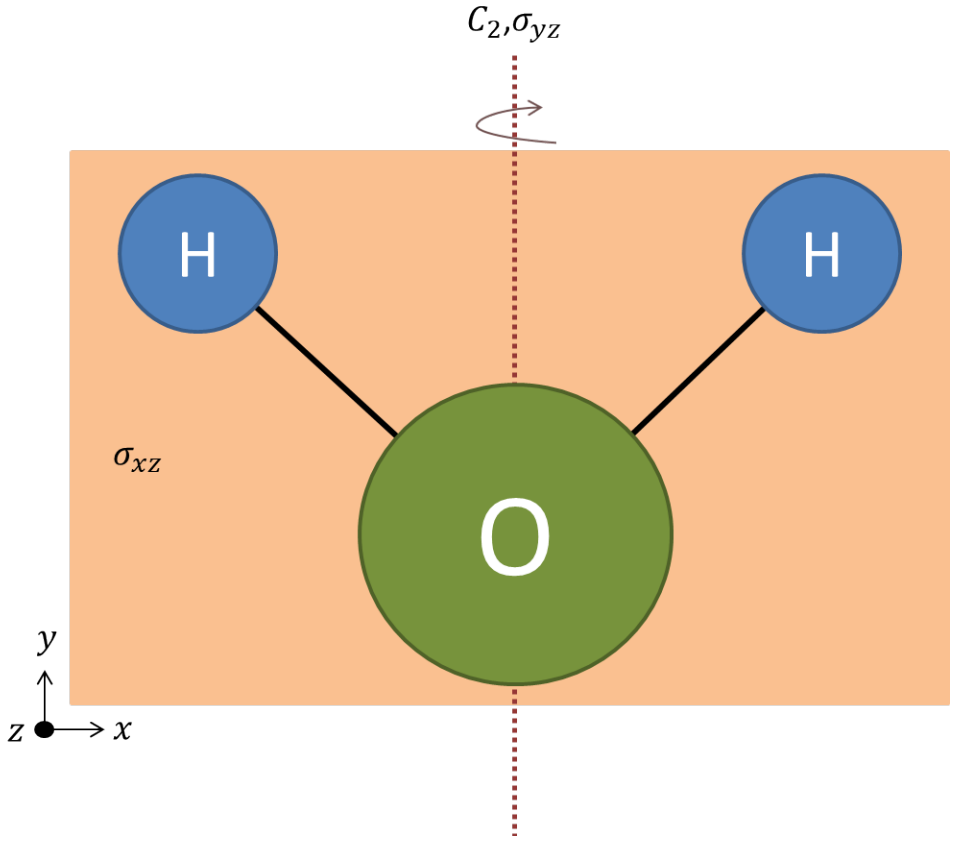

Figure 1.8: Diagram of the H_2O molecule and it's C_{2v} group elements. The pale orange plane shows the σ_{xz} reflection plane. The dashed red line indicates the σ_{yz} reflection planes as well as the C_2 rotation axis.

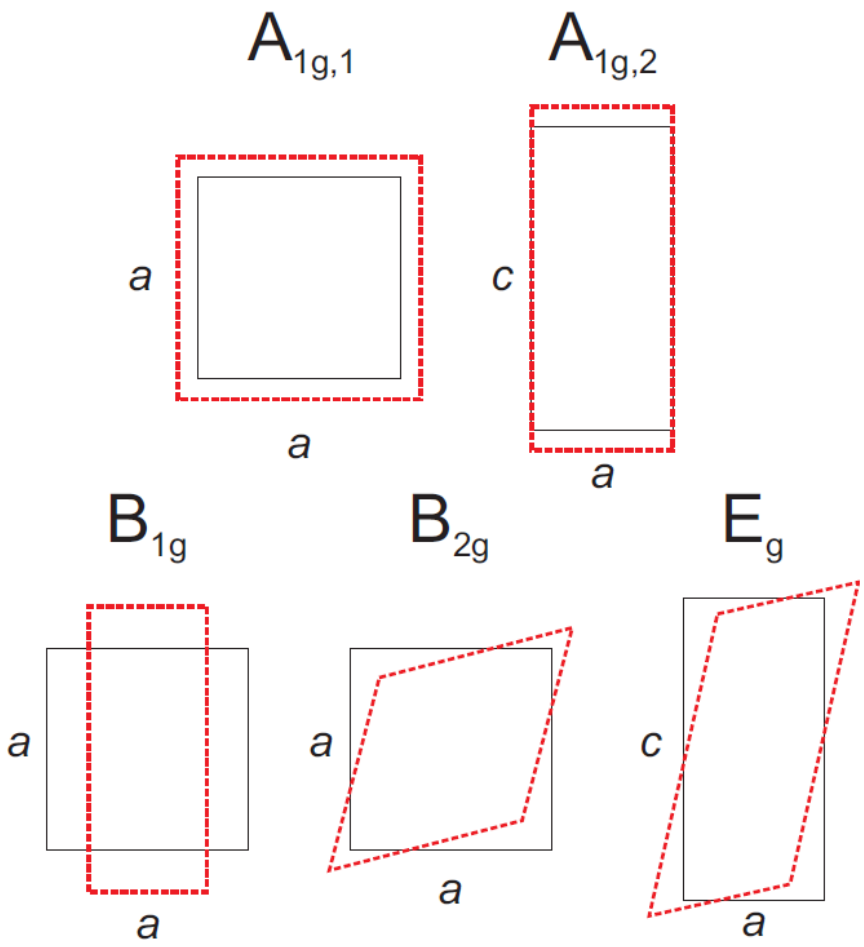

Figure 1.9: The allowed normal modes of vibration for the D_{4h} system as represented by specific characters of the D_{4h} group. The black solid line represents the static shape of the structure and the red dashed line represents the shape of a vibration of that shape for a given character. Figure shown here is taken from [63]

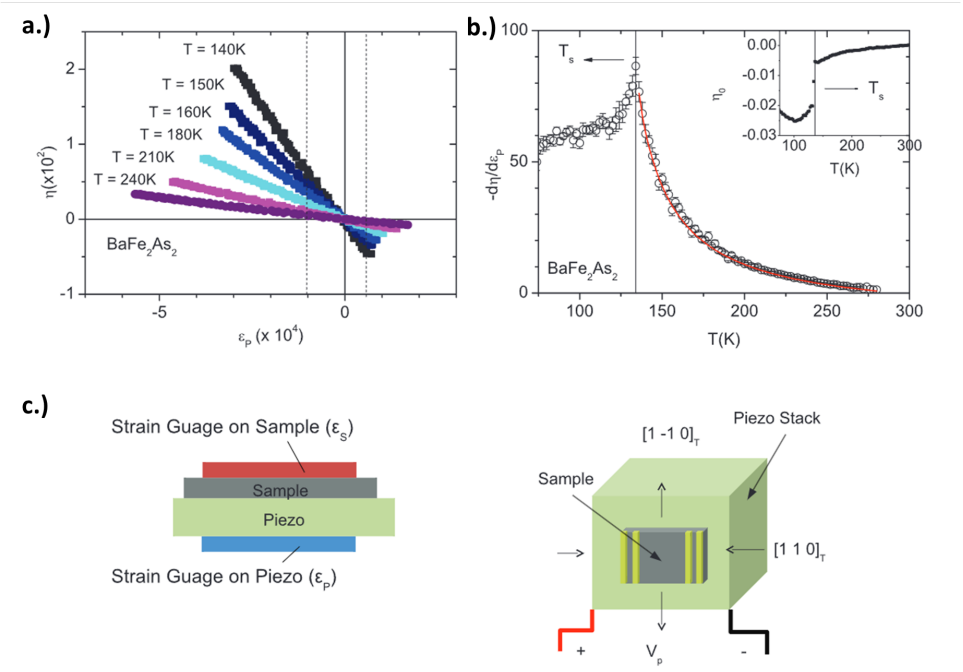

Figure 1.10: Example elastoresistance showing a nematic susceptibility signal in $BaFe_2As_2$ (in the D_{4h} group) [64]. **a.)** Elastoresistance (η) measured as a function of strain for temperatures between 240 K and 140 K. **b.)** nematic susceptibility as a function of temperature taken as the slope of η. **c.)** diagram of the experimental set-up used for elastoresistance on $BaFe_2As_2$. A sample is placed on top of a piezoelectric stack with strain gauges placed on top of the sample and below the piezo. The sample is wired for a four-wire resistance measurement and aligned such that strain is accessing the B_{2g} symmetry channel (Figure 1.9) with I along $[1, 1, 0]$ and perpendicular to $[1, -1, 0]$.

identity, a 90 degree rotation, 180 degree rotations, reflections, improper rotations, and an inversion. Within the D_{4h} point group there are two characters that will be of great for interest my discussion into $BaNi_2As_2$: the B_{1g} character representing the $x^2 - y^2$ normal mode and the B_{2g} character representing xy normal mode (Figure 1.9).

One way to detect nematicity is by performing elastoresistance measurements as outlined by Chu in $BaFe_2As_2$ [64] and Eckberg in $BaNi_2As_2$ [65] (Figure 1.10). In this measurement a sample is wired for resistance and placed on top of a piezoelectric

device or other form of strain applying device. The sample is specifically placed to apply stain along a particular symmetry channel of interest from the material's allowed point group characters. Resistance is then measured as a function of applied strain for a set of temperatures of interest. A change in resistance of the sample as a function of strain (if present) can then be attributed to a nematic susceptibility.

1.4 This Work

In this thesis, I describe the evolution of charge order and crystal structure in $Ba_{1-x}Sr_xNi_2As_2$ and pressurized $BaNi_2As_2$ and show how the charge order system in this material is related to nematicity and superconductivity enhancement. This works will further demonstrate why $BaNi_2As_2$ is an excellent candidate to study superconductive enhancement from non-magnetic sources.

In Chapter 2, I will discuss the experimental methods I used to characterize and study the charge order and the crystal structure of $Ba_{1-x}Sr_xNi_2As_2$. This will include a description of cryogenic techniques and technologies I used, resistivity measurements, elastic x-ray diffraction, high pressure piston cell electrical transport experiments, and high pressure diamond anvil x-ray diffraction experiments.

In Chapter 3, I will present my findings contributing towards a complete phase diagram for charge order and crystalline structure in $Ba_{1-x}Sr_xNi_2As_2$ as detected from elastic x-ray diffraction measurements. Highlighted in this Chapter will be a detailed description for three separate charge orders detected in the $Ba_{1-x}Sr_xNi_2As_2$ system: an incommensurate charge density wave in the tetragonal system at $Q_{tet} = 0.28$ (IC-CDW),

a commensurate charge density wave in the triclinic system at $Q_{tri} = 0.33$ (C-CDW1), and an additional commensurate charge density wave in the triclinic system at $Q_{tri} = 0.5$ (C-CDW2). Included will also be a discussion on how the IC-CDW is strongly correlated to the nematic order in $Ba_{1-x}Sr_xNi_2As_2$.

In Chapter 4, I will present my findings on and a complete phase diagram for charge order and crystal structure in pressurized $BaNi_2As_2$ as detected by x-ray diffraction and electrical transport. Descriptions on the evolution of each charge density wave, IC-CDW, C-CDW1, and C-CDW2 under pressure will be highlighted here.

In Chapter 5, I will present an analysis comparing the $Ba_{1-x}Sr_xNi_2As_2$ and pressurized $BaNi_2As_2$ systems. Additional data on the lattice constants of both systems will also be presented here for this analysis.

Chapter 2: Methods

The results I present in this thesis were obtained through a variety of different experimental techniques including low temperature electronic transport, x-ray diffraction, piston cell high pressure transport, and diamond anvil cell single crystal and powder x-ray diffraction.

All crystals of $Ba_{1-x}Sr_xNi_2As_2$ used here were grown by previous student Dr. Christopher Eckberg at the Quantum Materials Center (QMC) of the University of Maryland. Electrical transport and high pressure piston cell transport of $Ba_{1-x}Sr_xNi_2As_2$ was performed at QMC. Here I lead the piston cell efforts of QMC.

X-ray diffraction of $Ba_{1-x}Sr_xNi_2As_2$ was performed at the University of Illinois at Urbana-Champaign (UIUC) in collaboration with professor Peter Abbamonte's lab during two separate fellowship funded visits via the Institute for Complex Adaptive Matter (ICAM). While visiting UIUC, Sangjun Lee and Stella Sun taught me how to use their laboratory's custom X-ray diffraction system. I then co-lead the experiments on $Ba_{0.35}Sr_{0.65}Ni_2As_2$with students Sangjun and Stella. Data analysis was primarily handled by myself once back at UMD with technical support from Sangjun. During my second ICAM sponsored visit to UIUC, we began *in-situ* strain and X-ray diffraction experiments on $Ba_{1-x}Sr_xNi_2As_2$. During this trip I also assisted in further developing their X-ray data reciprocal space

mapping software in Python, where I was able to speed up their algorithum by roughly 75 %.

High pressure diamond anvil cells for studying $BaNi_2As_2$ were prepared in collaboration with Equilibrium Physics at Extreme Conditions (EPEC) group of Livermore National Laboratory during a fellowship funded visit via the Department of Energy's Graduate Research Fellowship. X-ray diffraction of these DACs were performed at the Argonne Advanced Photon Source (APS) via additional fellowship funding support from ICAM. While visiting EPEC, post-doctorates Daniel Sneed and Daniel Campbell instructed me on how to prepare their DACs for X-ray diffraction experiments. After using these lessons to build my own DACs, I used them at the 16-BMD beamline at APS to perform X-ray diffraction measurements under pressure and at low temperatures with technical support from the 16-BMD beamline staff and EPEC group leader, Jason Jeffries

In this chapter, I will describe and outline the experimental techniques I used to complete this work.

2.1 X-ray Diffraction

Critical to the success of this work is the use of X-ray diffraction for observing charge density waves and structural phase transitions. X-ray scattering is a vast topic with a myriad of experimental techniques and uses. As such, this section will only cover the basics of elastic x-ray diffraction required for understanding crystal structure and charge density wave identification.

2.1.1 Bragg's Law

Pivotal to the practice of X-ray diffraction is Bragg's Law, which governs the condition for constructive interference between X-ray wavelength, incident X-ray angle, and atomic layer spacing. Bragg's Law is a deceptively simple relationship that can be derived using a basic geometrical constructive interference argument (Figure 2.1). Imagine a beam of X-rays from a lab source incident on a single crystal sample surface at angle θ. This single crystal is made up of a periodic lattice of atoms with atomic planes all spaced at a distance, d, from one another. As the X-rays penetrate this sample, each layer passed will have the beam partially reflect some X-rays back out of the sample at the same angle θ. In order for the reflected beams to constructively interfere and exit the sample, the path lengths traveled by each beam must be an integer multiple of the X-ray wavelength. This path length traveled at each reflection between layers is $2d\sin(\theta)$. Knowing this, we can arrive at Bragg's Law

$$n\lambda = 2d\sin(\theta) \tag{2.1}$$

2.1.2 Miller Indices and Momentum Space

Bragg's Law shows a condition for constructive interference from scattering between periodic atomic planes, but it alone shares no information for which specific set of atomic planes are involved in the process. Instead, Bragg's Law naturally involves the periodic spacing, d, between a group of crystal planes. Therefore, translating the language of

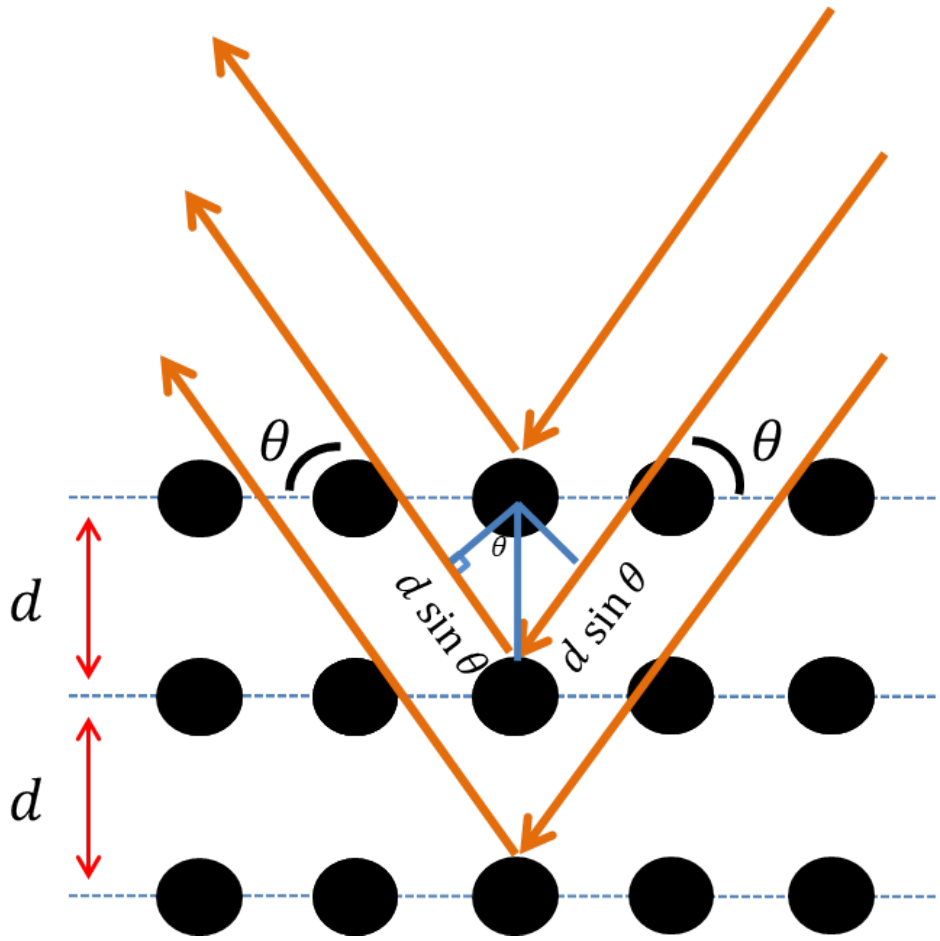

Figure 2.1: Illustration showing geometry of Bragg's Law for X-ray diffraction. Incident X-rays penetrate the sample at an angle θ relative to the sample's normal. Each horizontal atomic layer is spaced a distance d apart. Reflected X-rays from each atomic layer exit the sample at the same angle θ. Each reflected beam travels an extra path length of $2d\sin(\theta)$ relative to reflected X-rays of the layer above.

crystals from real space to " spacial frequency" space becomes a convenient coordinate system when examining diffraction data, as well as, a multitude of other characteristics of crystals. This frequency space is typically denoted reciprocal space or momentum space.

The following description of how to construct reciprocal space is adapted from Stephen H. Simon's *The Oxford Solid State Basics* [39]. Given a crystal structure with lattice vectors, $\mathbf{a}, \mathbf{b}, \mathbf{c}$, one can give the real space position of any point in a crystal as,

$$\mathbf{R} = n_1\mathbf{a} + n_2\mathbf{b} + n_3\mathbf{c} \tag{2.2}$$

A set of reciprocal lattice vectors, $\mathbf{b}$, can then be formed if they satisfy the relationship,

$$\mathbf{a_i} \cdot \mathbf{b_j} = 2\pi\delta_{ij} \tag{2.3}$$

The reciprocal lattice vectors can be formed using vector product relationships, and follow the general relationship of

$$\mathbf{b_i} = \frac{2\pi \mathbf{a_j} \times \mathbf{a_k}}{\mathbf{a_1} \cdot \mathbf{a_2} \times \mathbf{a_3}} \tag{2.4}$$

Note that for orthogonal unit cell structures, such as cubic, tetragonal, and orthorhombic, this relationship shows a clear reciprocal relationship, with each reciprocal space vector being proportional to the inverse to the corresponding real space vector.

$$\mathbf{b_i} = \frac{2\pi}{a_i}\hat{\mathbf{a}}_\mathbf{i} \tag{2.5}$$

We can now express any position in reciprocal space as a linear combination of

these reciprocal space vectors.

$$\mathbf{G} = H\mathbf{b_1} + K\mathbf{b_2} + L\mathbf{b_3} \tag{2.6}$$

the coefficients used here, $[H, K, L]$, are known as the Miller indices (Figure 2.2). These indices are used commonly as coordinates for describing crystal planes, charge density waves, diffraction peaks, and any other form of periodic geometry or physics that occurs within crystals. For orthogonal crystal systems, H, K and L can intuitively be thought of as spacial frequencies along each crystallographic direction, $\mathbf{a}, \mathbf{b}$ and $\mathbf{c}$ in reciprocal lattice units (r.l.u). For example, [1,0,0] would describe the set of crystal planes that repeat once every unit cell along $\mathbf{a}$ but do not repeat along $\mathbf{b}$ and $\mathbf{c}$. [2,0,0] describes the set of crystal planes that repeat twice every unit cell along $\mathbf{a}$ but do not repeat along $\mathbf{b}$ and $\mathbf{c}$. [2,2,0] describes the set of crystal planes that repeat twice along $\mathbf{a}$ and $\mathbf{b}$ but do not repeat along $\mathbf{c}$.

Importantly for this work, $[H, K, L]$ can have fractional values, and therefore correspond to periodicities larger than the unit cell, also known as superstructures. These fractional values correspond to two cases, commensurate and incommensurate. Commensurate $[H, K, L]$ are rational fractions and correspond to superstructures that repeat for an integer numbers of unit cells. For example, [$\frac{1}{2}$,0,0] is commensurate and corresponds to a superstructure that repeats every 2 unit cells along the $\mathbf{a}$ direction. Incommensurate $[H, K, L]$ are irrational fractions and correspond to superstructures that do not repeat for an integer number of unit cells. For example, [0.27,0,0] is incommensurate (as we can usually only accurately measure out to two or three decimal places of reciprocal space) and

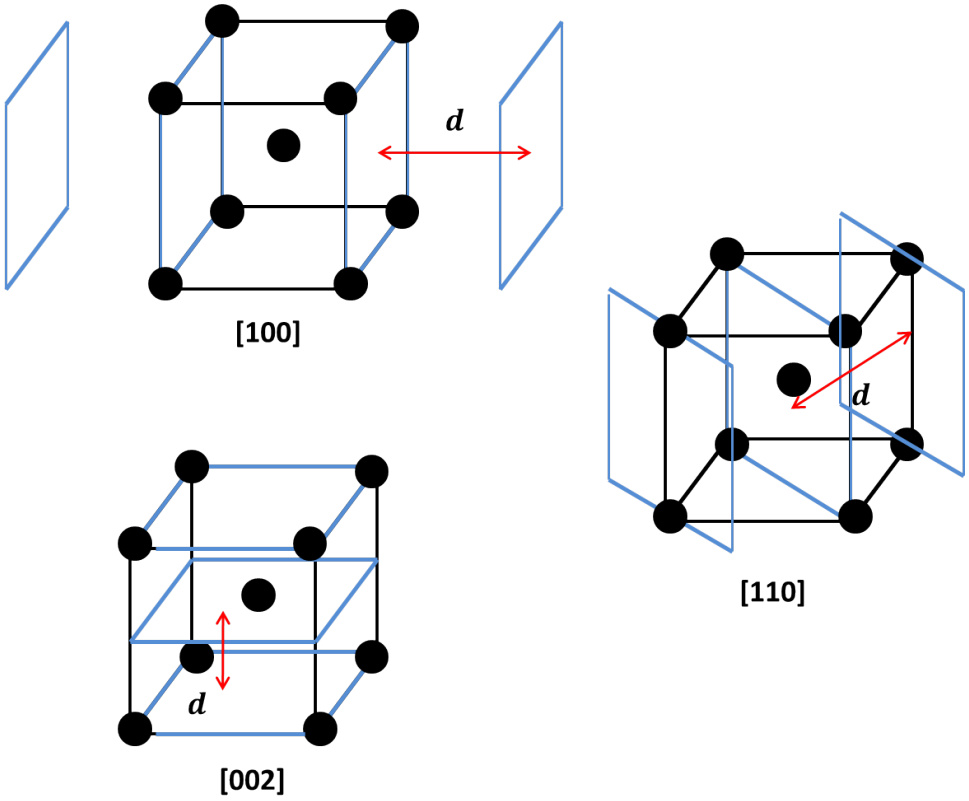

Figure 2.2: Geometric examples of perioidic crystal planes for a simple body-centered cubic lattice described using Miller indecies. The [1,0,0], [1,1,0] and [0,0,2] crystal planes are shown. For each set of crystal planes, the associated d spacing used in Bragg's Law is shown.

corresponds to a superstructure that repeats roughly every $\frac{1}{0.27} = 3.703703...$ unit cells along the $\mathbf{a}$ direction, never quite matching up to the underlying lattice grid.

2.1.3 Laue condition

Using the knowledge of reciprocal space, an equally valid and informative model to Bragg's Law can be formed for describing X-ray diffraction known as the Laue condition. First, we can use definition of a real space vector given by equation 2.2 and the definition of a reciprocal space vector given in equation 2.6 along with equation 2.3 to create a relationship between any new real and reciprocal space vectors,

$$\mathbf{G} \cdot \mathbf{R} = 2\pi m \tag{2.7}$$

where m is an integer. Next, we can describe a generalized scattering event as an incident X-ray upon a crystalline sample of wavevector $\mathbf{k}$ and an exiting X-ray of wavevector $\mathbf{k}'$. A generalized scattering event can be described by Fermi's golden rule, which is typically covered in most graduate level quantum mechanics courses,

$$\Gamma(r) = \frac{2\pi}{\hbar} |\langle \mathbf{k}' | \, V \, | \mathbf{k} \rangle|^2 \delta(E_{\mathbf{k}'} - E_{\mathbf{k}}) \tag{2.8}$$

where Γ is the transition rate per unit time of a partical scattering from $\mathbf{k}$ into $\mathbf{k}'$ and we have chosen to model the sample as a potential, V. We'll select $|\mathbf{k}| = |\mathbf{k}'|$ to account for the delta function, meaning we will be conserving energy between the incident and exiting X-rays (otherwise known as elastic scattering). We can now write the matrix element as

$$\langle \mathbf{k}' | \, V \, | \mathbf{k} \rangle = \int d\mathbf{r} \frac{e^{-i\mathbf{k}'\cdot\mathbf{r}}}{\sqrt{\nu}} V(\mathbf{r}) \frac{e^{i\mathbf{k}\cdot\mathbf{r}}}{\sqrt{\nu}} = \int d\mathbf{r} \frac{e^{i(\mathbf{k}'-\mathbf{k})\cdot\mathbf{r}}}{\nu} V(\mathbf{r}) \tag{2.9}$$

noting that the ν is the crystal volume and just accounts for normalizing the wavefunction. Seeing that $\mathbf{r}$ is any real space position in the crystal, we can rewrite $\mathbf{r}$ in terms of a real space lattice vector, $\mathbf{R}$, plus the remainder, $\mathbf{x}$. Doing this we can now rewrite the matrix element as,

$$\langle \mathbf{k}' | \, V \, | \mathbf{k} \rangle = \frac{1}{\nu} \sum_{\mathbf{R}} \int d\mathbf{x} e^{i(\mathbf{k}'-\mathbf{k})\cdot(\mathbf{R}+\mathbf{x})} V(\mathbf{R}+\mathbf{x})) \tag{2.10}$$

Because the crystal is spatially periodic with $\mathbf{R}$, we assume the potential must also be periodic. This gives us $V(\mathbf{R}+\mathbf{x}) = V(\mathbf{x})$. We can now rewrite the matrix element as,

$$\langle \mathbf{k}' | \, V \, | \mathbf{k} \rangle = \frac{1}{\nu} \left[\sum_{\mathbf{R}} e^{i(\mathbf{k}'-\mathbf{k})\cdot\mathbf{R}} \right] \int d\mathbf{x} e^{i(\mathbf{k}'-\mathbf{k})\cdot\mathbf{x}} V(\mathbf{x}) \tag{2.11}$$

From complex analysis, the bracketed term will become zero unless

$$(\mathbf{k}' - \mathbf{k}) \cdot \mathbf{R} = 2\pi n \tag{2.12}$$

where n is any integer. Using equation 2.7, we can select $n = m$ and find the condition on the X-rays and the reciprocal lattice,

$$\begin{aligned} \mathbf{k}' - \mathbf{k} &= \mathbf{G} \\ |\mathbf{k}| &= |\mathbf{k}'| \end{aligned} \tag{2.13}$$

This is the Laue condition for X-ray diffraction. Note that these are simply a

statements on the conservation of momentum and energy of the incident and outgoing X-rays. Sometimes you will hear X-ray diffraction experts refer to this as "the conservation of crystal momentum".

This condition can also be shown to be equivalent to Bragg's Law. To do this, multiply each side of equation 2.13 by $\mathbf{G}$ remembering the geometry shown in Figure 2.1 and knowing $k = \frac{2\pi}{\lambda}$ as well as $G = \frac{2\pi}{d}$.

$$(\mathbf{k}' - \mathbf{k}) \cdot \mathbf{G} = \mathbf{G} \cdot \mathbf{G}$$

$$\frac{2\pi}{\lambda}(\sin\theta' - \sin\theta)\frac{2\pi}{d} = G^2$$

$$\frac{4\pi^2}{\lambda d}(2\sin\theta) = \frac{4\pi^2}{d^2}$$

$$\frac{1}{\lambda}(2\sin\theta) = \frac{1}{d}$$

$$\lambda = 2d\sin\theta$$

Thus we now have two different but equivalent ways to view X-ray diffraction: Bragg Law's geometric and constructive interference interpretation and Laue's quantum scattering and momentum interpretation. Both views of X-ray diffraction can be helpful to consider for different situations.

2.1.4 X-ray Instrumentation and Tools

The X-ray experiments I performed on $Ba_{1-x}Sr_xNi_2As_2$ at ambient pressure occurred at Peter Abbamonte's UIUC X-ray lab using their group's Huber 4-circle diffractometer (Figure 2.3). The X-ray source for the system is a Xenocs GeniX3D Mo K_α microspot source. It provides 2.5×10^7 photons/sec with a beam size of 130 μm at the sample location. The intensity profile as a function of energy is given in Figure 2.3-b, showing most of the intensity peaked at 17.48 keV, corresponding to the Mo $K_{\alpha 1}$ emission peak. Experiments performed on $Ba_{1-x}Sr_xNi_2As_2$ used this Mo $K_{\alpha 1}$ peak with scattering from the $K_{\alpha 2}$ and K_β peaks excluded from data analysis. The samples were enclosed in a closed-cycle helium cryostat with working base temperature of 8.9 K. The dome of the cryostat was made of Be, allowing X-ray transmission into and out of the sample environment. X-ray diffraction images were collected using a Mar345 image plate detector with an active area of 345 nm in diameter and single photon sensitivity.

The X-ray experiments I performed on $BaNi_2As_2$ under pressure occurred at the Advanced Photon Source using the 16-BMD beamline (Figure 2.4). This beamline is primarily designed for High-pressure X-ray diffraction, X-ray absorption spectroscopy, and X-ray transmission computed tomography. The beamline is capable of an energy range between 6 and 60 KeV with an intensity profile as a function of energy given in Figure 2.4 and in [66]. The energy is selected by the user upstream from the DAC using Si monochrometers. While the raw intensity of the beam peaks for 20 KeV, it peaks after transmission through DACs at 25 KeV. For my experiments, I selected 30 KeV, as it was the best compromise between beam intensity and number of Brillouin zones present on

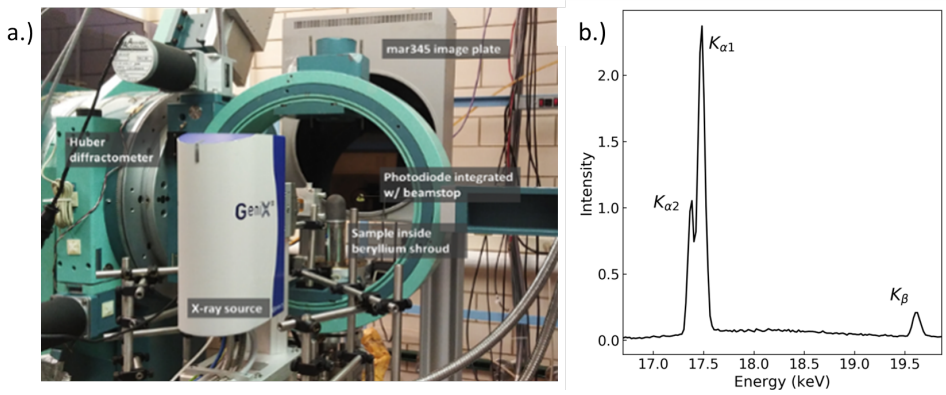

Figure 2.3: **a.)** Single crystal X-ray diffractometer used to measure XRD on $Ba_{1-x}Sr_xNi_2As_2$ in Peter Abbamonte's Lab. A 4-circle Huber diffractometer is used to control θ for the sample. The sample is enclosed within an X-ray transparent Be shroud and vacuumed sealed. Cooling power is brought to the sample via the closed circle cryostat underneath it. Diffracted X-rays are counted on the mar345 Image plate. Direct, undiffracted X-rays are stopped and measured by a photodiode. X-rays are sourced to the sample by a Xenocs GeniX3D Mo K_α microspot source. **b.)** The output energy spectrum of the X-ray source.

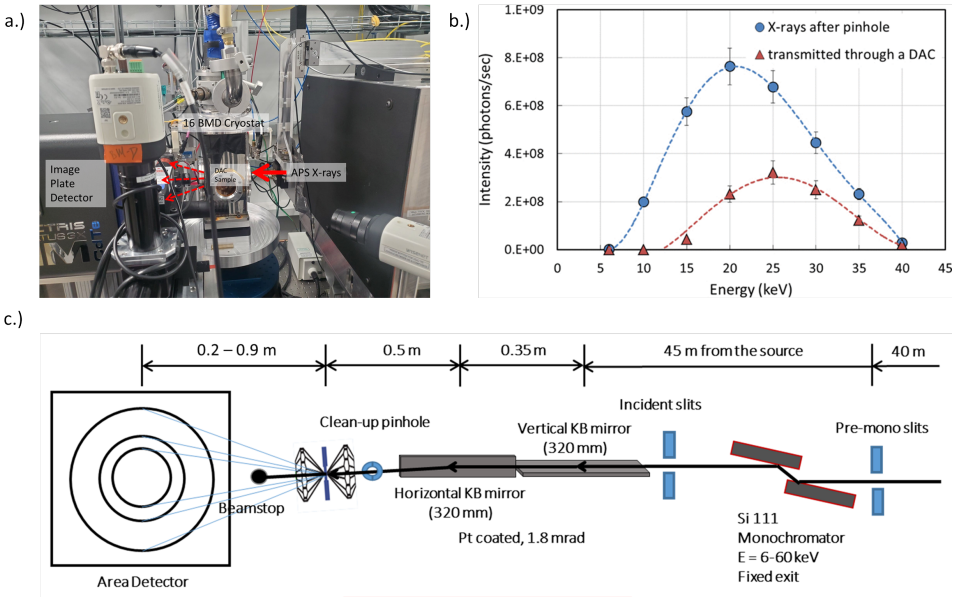

Figure 2.4: **a.)** 16-BMD beamline used to measure single crystal x-ray diffraction of $BaNi_2As_2$under pressure. The DAC and sample are housed in an on-beamline closed cycle cryostat. A motor stage below rotates the cryostat through θ. **b.)** Energy spectrum of the 16-BMD beamline post-pinhole (blue) and after transmission through a DAC (red) [66]. The energy spectrum peaks at 20 keV post-pinhole but is reduced and upshifted towards higher energies after transmission through a DAC. **c.)** The path of X-rays from the APS source to the 16-BMD beamline [66]. Energy of the beam is selected upstream using Si [1,1,1] monochrometers. The beam is then shaped using a collection of X-ray optics before arriving at the sample stage for diffraction.

the detector. A Pilatus 1M detector was used with a size of 1043×981 pixels. This beamline allowed me to change the DAC pressure via a gas inlet on top of the DAC, change the temperature of the cryostat, and move all relevant motors from outside the hutch

2.1.5 Reciprocal Space Mapping

Reciprocal space mapping is the procedure of converting X-ray data from pixels on a detector to X-ray data in $[H, K, L]$ space. During my experiments, samples were staged on 6-circle geometry instruments at Peter Abbamonte's UIUC lab, as well as, and the 16-BMD line at the Advanced Photon Source. In both labs, a 2D plate detector was used to capture single crystal X-ray diffraction images. Typically for this set-up, the sample stage would rotate θ from a starting to ending point in small increments, taking X-ray diffraction images at each stop point. For experiments performed on $Ba_{1-x}Sr_xNi_2As_2$ in Abbamonte's lab, I rotated θ from 0° to 20° in 0.05 ° steps for each temperature, creating 400 images per temperature. For each 400 image set, I created a "θ integrated" image by assigning each pixel on that new image with the maximum X-ray intensity value for that pixel across the 400 image set (Figure 2.5). For experiments performed at 16-BMD on $BaNi_2As_2$ under pressure, I was limited in my range for θ due to the windows on the pressure cell and the cryostat. I rotated θ from -4.5 ° to 4.5 ° in 0.3 ° steps for each temperature and pressure, creating 30 images per temperature and pressure. For these experiments, I also took long exposures while slowly rotating from -4.5 ° to 4.5 ° in order manually obtain θ integrated images.

Each X-ray data set for a given temperature and pressure contains X-ray intensity data as a function of (x_{pixel},y_{pixel},n) where n is the image number within a set. A reciprocal space mapping was built for each temperature and pressure to convert data from pixel coordinates (x_{pixel},y_{pixel},n) to angular coordinates (δ,γ,θ) and finally to reciprocal space coordinates $[H, K, L]$. The geometry used for pixel to angular coordinate conversion is

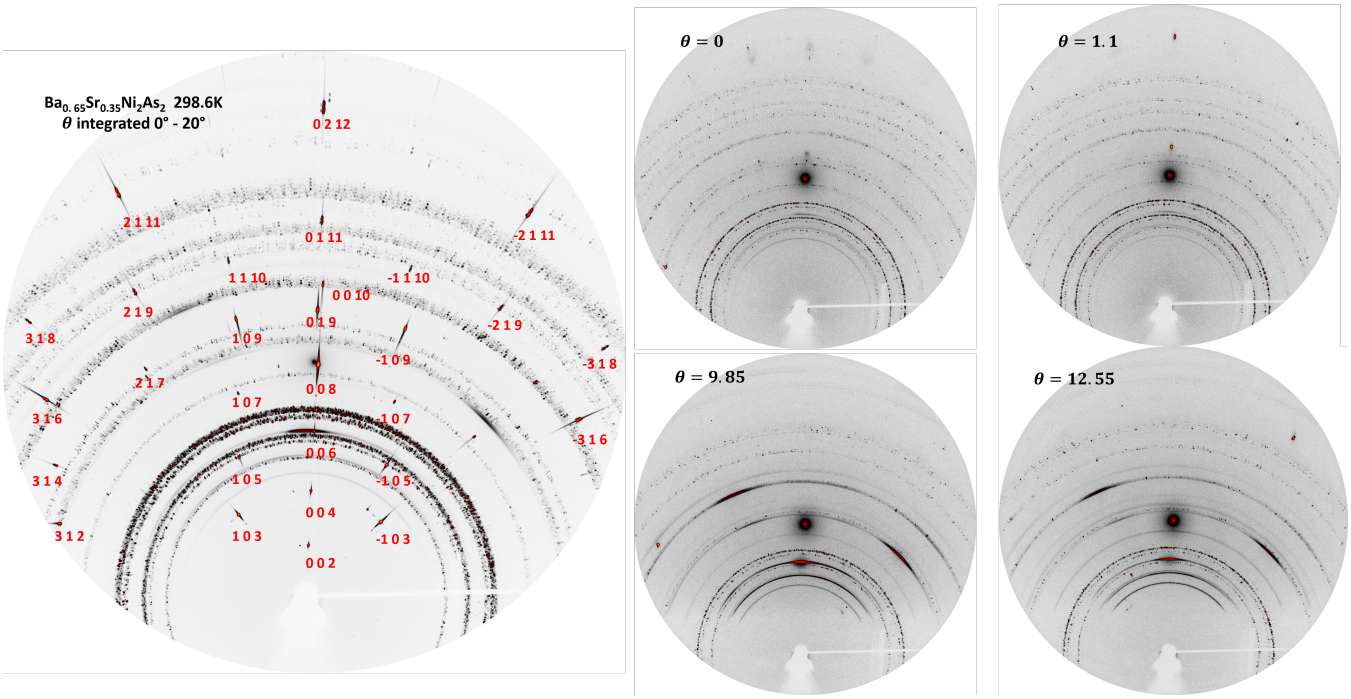

Figure 2.5: Example X-ray diffraction data of $Ba_{1-x}Sr_xNi_2As_2$ at room temperature. A full θ integrated image is shown on the left with each Bragg peak indexed. Intensity found along the rings is a powder XRD pattern from the Be dome. Four examples of individual θ diffraction images are shown on the right. A set of 400 images comprising $\theta = 0\ ^\circ$ to $\theta = 20\ ^\circ$ make up a composite θ integrated image for each temperature measured.

given in Figure 2.6. Using the direct beam position on the detector along with the distance from the sample to the detector, one can describe the position of any pixel position on the detector using the distance from the sample to that pixel, r, along with two angles showing the offset in the x and y directions, γ and δ:

$$\begin{aligned} r &= \sqrt{(x - x_0)^2 + (y - y_0)^2 + d^2} \\ \gamma &= \arcsin \frac{x - x_0}{r} \\ \delta &= \arcsin \frac{y - y_0}{d} \end{aligned} \tag{2.14}$$

Additionally, θ can be computed simply from the image number and the step size of θ between images

$$\theta = n\theta_{step} \tag{2.15}$$

With the data now given as a function of angles (δ,γ,θ) in the lab frame, we must now convert from the lab frame to the crystal's frame using the basis of $[H, K, L]$ for a given crystal using what is known as "UB" matrix formalism,

$$\mathbf{Q_l} = 2\pi UB \begin{pmatrix} H \\ K \\ L \end{pmatrix} \tag{2.16}$$

where $\mathbf{Q_l}$ is the lab frame's momentum space, B is the transformation between $[H, K, L]$ and a Cartesian coordinate system tied to the sample, and U is the transformation

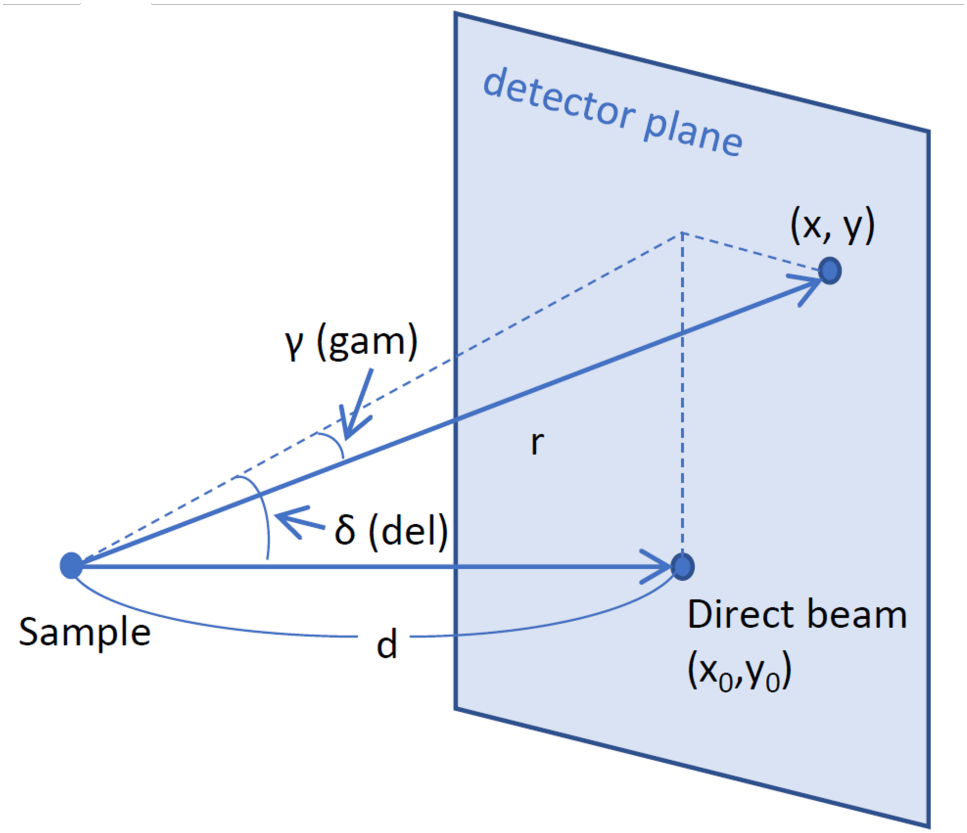

Figure 2.6: Scattering geometry used for single crystal X-ray experiments on $Ba_{1-x}Sr_xNi_2As_2$. The sample lies at a perpandicular distance from the detector, d. The direct beam position on the detector are given by the pixel coordinates (x_0,y_0). Any position on the detector, (x,y) can be described using a set of angles (γ,δ) along with a radial distance from the sample, r.

between the crystal's Cartesian coordinate system and the lab's Cartesian coordinate system. The details of this formalism are greatly spelled out in [67, 68].

I calculated the UB matrix for each X-ray data set using the X-ray software, *SPEC*. This procedure involved properly indexing (or identifying) the $[H, K, L]$ associated with each Bragg peak with their given (x_{pixel},y_{pixel},n) coordinate on the detector. The pixel coordinates of each Bragg peak are then converted to the angular lab frame coordinates, (δ,γ,θ) using equations 2.14 and 2.15. *SPEC* is then used to calculate a UB using the

indexed Bragg peaks with their respective angular positions. Once the UB matrix is calculated, the reciprocal spacing mapping procedure is complete. Any pixel coordinate position, (x_{pixel},y_{pixel},n), can now be converted to $[H, K, L]$ using the UB matrix and angular conversion equations. The conversion of pixel coordinates to $[H, K, L]$ using calculated UB matrices in this thesis was completed using custom Python software co-developed my myself and Sangjun Lee, former graduate student of Peter Abbamonte.

2.2 Cryogenic Technologies

For my measurements investigating the charge order of $BaNi_2As_2$, I needed cryogenic experimental environments capable of being tuned down to very low temperatures. All transport experiments were conducted in commercially available Physical Property Measurement Systems (PPMS) manufactured by Quantum Design, offering intuitive measurement controls for electrical transport between 1.8 K and 400 K (Figure 2.7). All x-ray diffraction measurements were performed using smaller, beamline appropriate closed cycle cryostats with x-ray transparent windows and materials. The cryostat used with UIUC's group was able to reach 11 K and the cryostat provided to me by the APS for the 16-BMD beamine was able to reach 38 K.

When using a PPMS, the sample is loaded into the chamber under a partial helium pressure of around 10 torr at room temperature. To cool the sample, cold helium gas from a liquid helium bath is pulled past the sample chamber, giving the user temperature control between 10 K and 300 K. Below 10 K, liquid helium is transferred to a 1 K pot. Helium vapor is pulled from this pot, allowing for evaporative cooling of the helium below it's

Figure 2.7: Quantum Design 14T PPMS system used to complete high pressure electrical transport measurements of $Ba_{1-x}Sr_xNi_2As_2$. Electrical transport apparatuses of measurement interest are loaded from the top down a thin cylindrical chamber. The sample environment is then purged and sealed at vacuum before beginning measurements.

natural 4.2 K boiling point to 1.8 K. Temperature and measurement control of the PPMS for my experiments were handled using their MultiVu software.

2.3 High Pressure Diamond Anvil Cell X-ray Diffraction Up to 10.5 GPa

In collaboration with the Livermore High Pressure Physics Group, EPEC, I employed the used of their diamond anvil cells (DACs) to study single crystal X-ray diffraction $BaNi_2As_2$ up to high pressures of 10.5 GPa (Figure 2.8). In these DACs, samples of interest are housed inside a gasket hole tightly confined by two co-aligned diamond culets. The culet sizes used in these DACs can range from 500 μm to around 100 μm, with smaller culets being used to reach higher pressures and smaller culets being used for lower pressures and finer pressure tuning. For experiments into $BaNi_2As_2$, 500 μm and 300 μm culet cells were prepared to reach the desired final pressures of around 10 to 12 GPa. The diamonds sat on Tungsten-carbide seats due to their X-ray transparency. Inside the gasket housing, samples of Ruby are also placed as a pressure manometer. The laser florescence of Ruby is well known as a function of temperature and pressure [69]. The gasket hole was filled with Ar gas as a pressure medium.

Pressure can be applied to the system manually by turning pistons. However for beamline operations, He gas can be used to control the pressure remotely. He gas can be fed in through a He inlet to a He membrane at the top of the DAC. If the screws are removed, pressure can be held applying He gas to the He membrane. Pressure can then be added by supplying more He gas to the membrane.

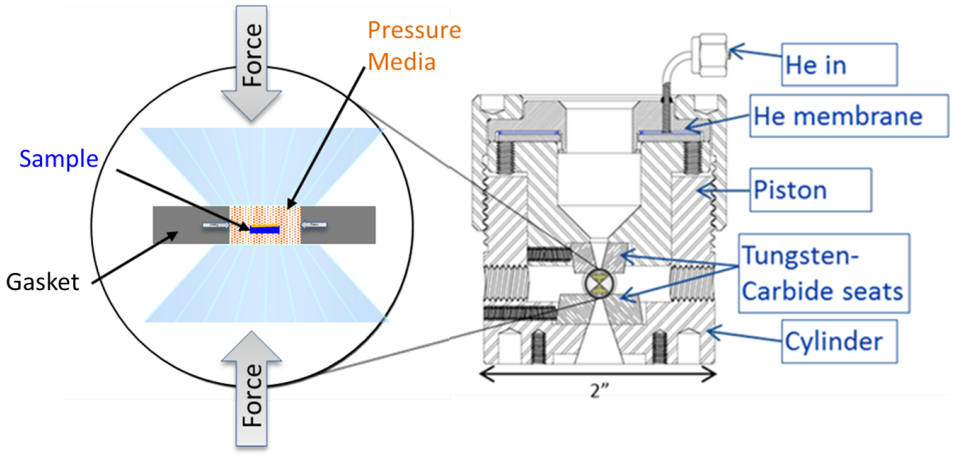

Figure 2.8: Schematic showing the major components of EPEC's DACs. A detailed description is given in the text.

2.4 High Pressure Piston Cell Electrical Transport Up to 2.5 GPa

A high pressure piston cell from C&T Factory Co. was used to to perform resistivity vs pressure and temperature measurements on $Ba_{0.30}Sr_{0.60}Ni_2As_2$(Figure 2.9). The feedthrough houses 7 twisted wire pairs that are used for 4 wire connections with the sample, A manganin coil, and a thin peice of Pb wire. The manganin coil is used a pressure manometer for room temperature. This is done by measuring the change in resistance as a function of pressure using the equation [70]

$$P = \frac{1000}{2.48}\left(\frac{R_P}{R_0 - 1}\right) \tag{2.17}$$

where P is the measured pressure in units of kbars, R_P is the resistance of the manganin coil at a pressure, P, and R_0 is the resistance of the coil at ambient pressure.

The Pb wire is used as a pressure manometer for base temperature. The pressure can

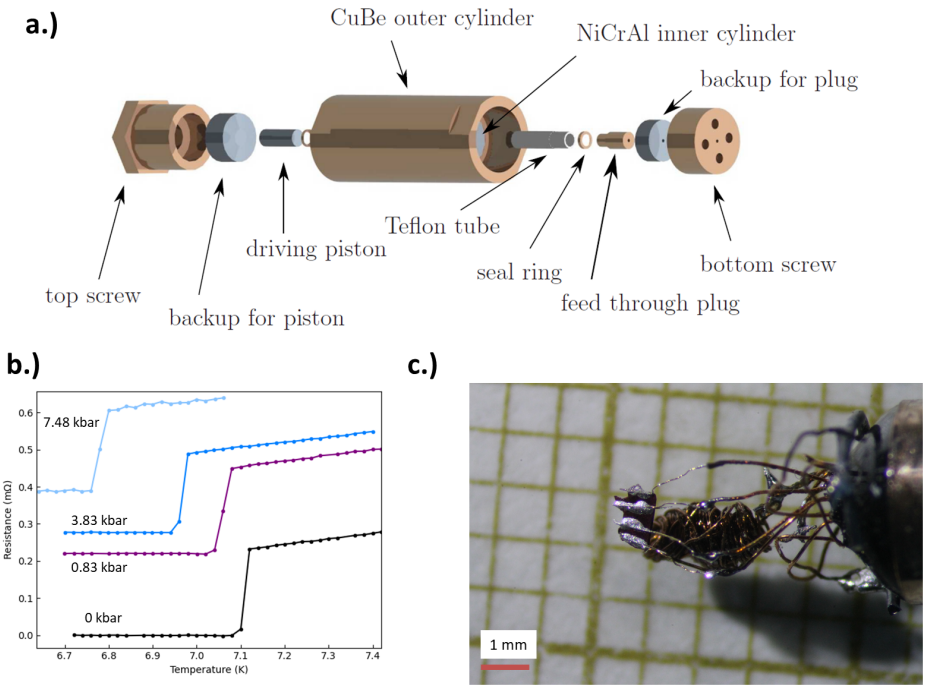

Figure 2.9: **a.)** Schematic of each part of the C&T High Pressure Piston Transport Cell. **b.)** Selected low temperature resistance measurements of a Pb wire pressure manometer showing the change in $T_c$for increasing pressure. Curves have been vertically separated for clarity. **c.)** A completed feedthrough showing a maganin coil, Pb wire, and sample wired to twisted wire pairs. The red sample shown is ReO_3.

be calculated by measuring the change in the Pb superconducting transition at pressure to ambient pressure using [71],

$$P = \frac{T_{c0} - T_{cP}}{0.0361} \tag{2.18}$$

where P is the calculated pressure in units of kbar, T_{c0} is the T_c of the Pb strip at ambient pressure, and T_{cP} is the T_c of the Pb strip at pressure, P.

Construction of the piston pressure cell begins with preparing a feedthrough plug

with 7 twisted wire pairs sealed by stycast. A manganin coil, thin lead wire, and a sample are then each wired to their own two sets of wire pairs to create 4 wire contact resistance measurements. All three components of the feedthrough as then tightly packed into a Teflon cap while submerged in Arcros Organics Perfluoro-compound FC-770™ fluid acting as the pressure medium. The feedthrough plus Teflon cap are inserted into the NiCrAl inner cylinder along with a driving piston on top. A series of top and bottom screws are inserted in the top and bottom of the cell. A hole is present in the top screw, where a hydraulic press is able to apply forces on the order of 1000's of psi to the driving piston, applying pressure to the feedthrough cap. Once a desired pressure is reached, the top screw is pushed further in to relieve force from the driving piston and maintain pressure for a measurement. Custom PPMS adaptors, fashioned by the UMD Physics machine shop, are screwed into the top and bottom screws for attachment onto a PPMS puck and use in the 14T PPMS machine.

Chapter 3: Charge Order Evolution in $Ba_{1-x}Sr_xNi_2As_2$

The following chapter will outline my work on the observation of charge density wave order via X-ray diffraction in $Ba_{1-x}Sr_xNi_2As_2$. The work presented here was performed in collaboration with Peter Abbamonte's X-ray group at UIUC and has been published in "Multiple Charge Density Waves and Superconductivity Nucleation at Antiphase Domain Walls in the Nematic Pnictide $Ba_{1-x}Sr_xNi_2As_2$" Sangjun Lee, John Collini, et. al. Physical Review Letters (2021) [3], "Absence of precursor incommensurate charge order in electronic nematic $Ba_{0.35}Sr_{0.65}Ni_2As_2$" John Collini, et. al. Physical Review B (2022) [1], and "Sixfold enhancement of superconductivity in a tunable electronic nematic system" Christopher Eckberg,...John Collini, et.al. Nature Physics (2020) [65].

3.1 Introduction to $BaNi_2As_2$ and $Ba_{1-x}Sr_xNi_2As_2$

$BaNi_2As_2$ is tetragonal and exists in the $ThCr_2Si_2$ structure (Figure 3.1). This structure consists of Ba layers spaced in-between Ni-As layers along the c-axis. $BaNi_2As_2$ is isostructual to its famous iron-based counterpart, $BaFe_2As_2$, at room temperature. At 140 K, $BaFe_2As_2$ undergoes a 1st order tetragonal to orthorhombic structural distortion [72], meaning $a \neq b \neq c$ and $\alpha = \beta = \gamma = 90°$ for this new structure. $BaNi_2As_2$ instead undergoes a first-order tetragonal to triclinic structural phase transition at $T_s = 135$ K,

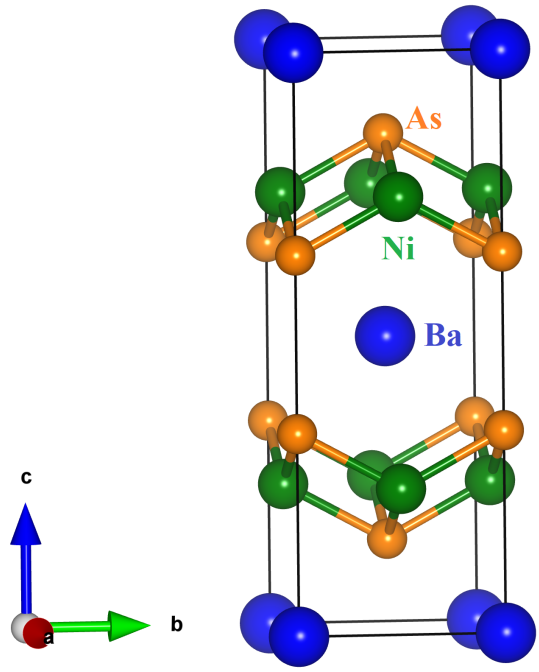

Figure 3.1: Crystal structure of room temperature $BaNi_2As_2$ in the tetragonal state.

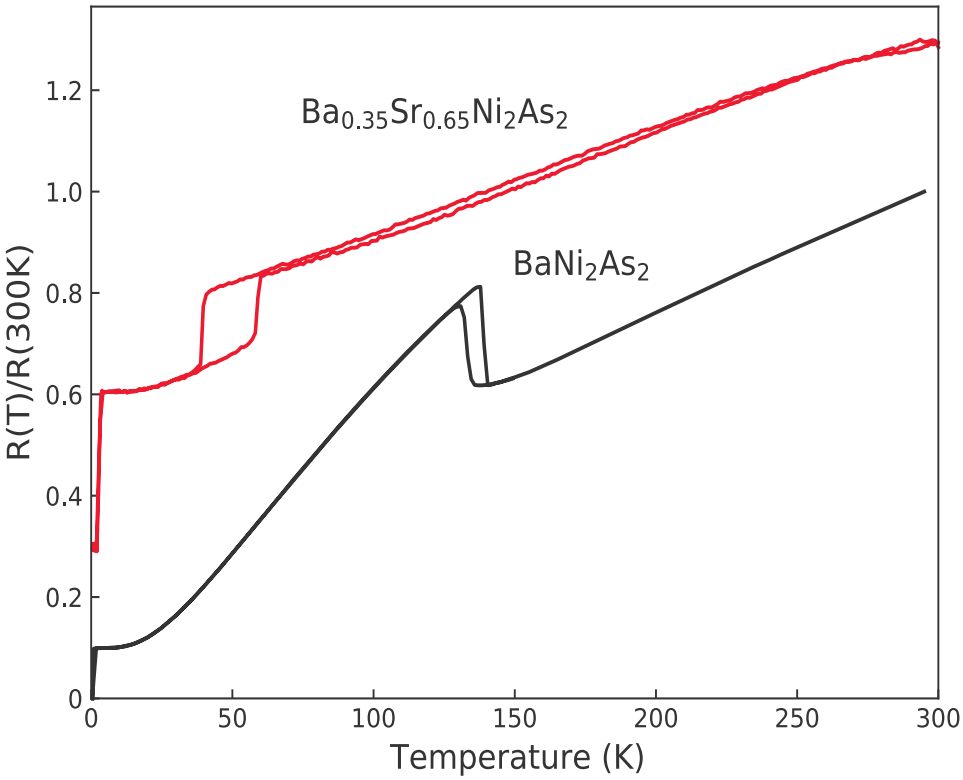

Figure 3.2: Resistance of $BaNi_2As_2$ and $Ba_{0.35}Sr_{0.65}Ni_2As_2$ normalized to 300 K data. $Ba_{0.35}Sr_{0.65}Ni_2As_2$ has been offset from $BaNi_2As_2$ for clarity. The triclinic distortion in $BaNi_2As_2$ can be seen in resistance at 135 K on cooling and at 138K on warming and in $Ba_{0.35}Sr_{0.65}Ni_2As_2$ at 40 K on cooling and at 58K on warming. The T_c of $BaNi_2As_2$ and $Ba_{0.35}Sr_{0.65}Ni_2As_2$ is measured at 0.6 K and 3 K respectfully. [1]

meaning $a \neq b \neq c$ and $\alpha \neq \beta \neq \gamma \neq 90°$ for this new structure. The onset of this transition can be seen in X-ray as well as resistance [1–3,65] (Figure 3.2). The tetragonal and triclinic phases of $BaNi_2As_2$ are denoted by sets of distinct Bragg peaks that index to the space groups of $I4/mmm$ and $P1$ respectively. Here I will use $(H, K, L)_{tet}$ and $(H, K, L)_{tri}$ separately to describe positions in momentum space for each phase.

Accompanying the orthorhombic transition in $BaFe_2As_2$ is the onset of a spin density wave (SDW) order [72]. However for $BaNi_2As_2$, neutron measurements have shown no

evidence of a magnetic structure in its low temperature phase or anywhere else [73]. $BaNi_2As_2$ also becomes superconducting at $T_c = 0.7$ K [74], and thermal conductivity measurements suggest that this superconducting state is fully gapped and likely conventional [75]. The other end member, $SrNi_2As_2$, shows no evidence for a structural distortion or magnetic order, but also superconducts below $T_c = 0.62$ K [76]. Isovalent substitution of Sr for Ba in $Ba_{1-x}Sr_xNi_2As_2$ has been shown to suppress T_s toward absolute zero temperature and enhance T_c up to a maximum value of 3.5 K at x=0.71 [65]. Additional substitutions of Co for Ni and P for As have also been studied for $BaNi_2As_2$ (Figure 3.4)

Elastoresistivity measurements of $Ba_{1-x}Sr_xNi_2As_2$ probing the B_{1g} channel, corresponding to the symmetry-breaking strain along the [100] and [010] tetragonal crystallographic directions, have revealed a large nematic susceptibility throughout the range of Sr substitution [65]. In addition, this experiment also revealed striking non-reversible hysteretic behavior in the nematic response just above the triclinic distortion between x=0 and x=0.5, implying the presence of an ordered electronic nematic in the tetragonal structural phase. With increasing Sr content, this nematic order begins to fade until a crossover to electronically driven nematic fluctuations occurs in the intermediate region around x=0.5. Further increasing Sr content to x=0.6 expels the nematic order. Continued increase in Sr content yields a strong nematic susceptibility emerging at x=0.71, just above the maximum in T_c.

X-ray measurements performed on $Ba_{1-x}Sr_xNi_2As_2$ by myself and Sangjun Lee have uncovered three separate CDW states evolving in the system as a function of x (Figure 3.3). These charge ordered states consist of an incommensurate CDW (IC-CDW) in the tetragonal state at $Q = (0.28, 0.28, 0)_{tet}$, a commensurate charge density wave state (C-CDW1) in the triclinic state at $Q = (0, 0.33, 0)_{tri}$, and an additional commensurate

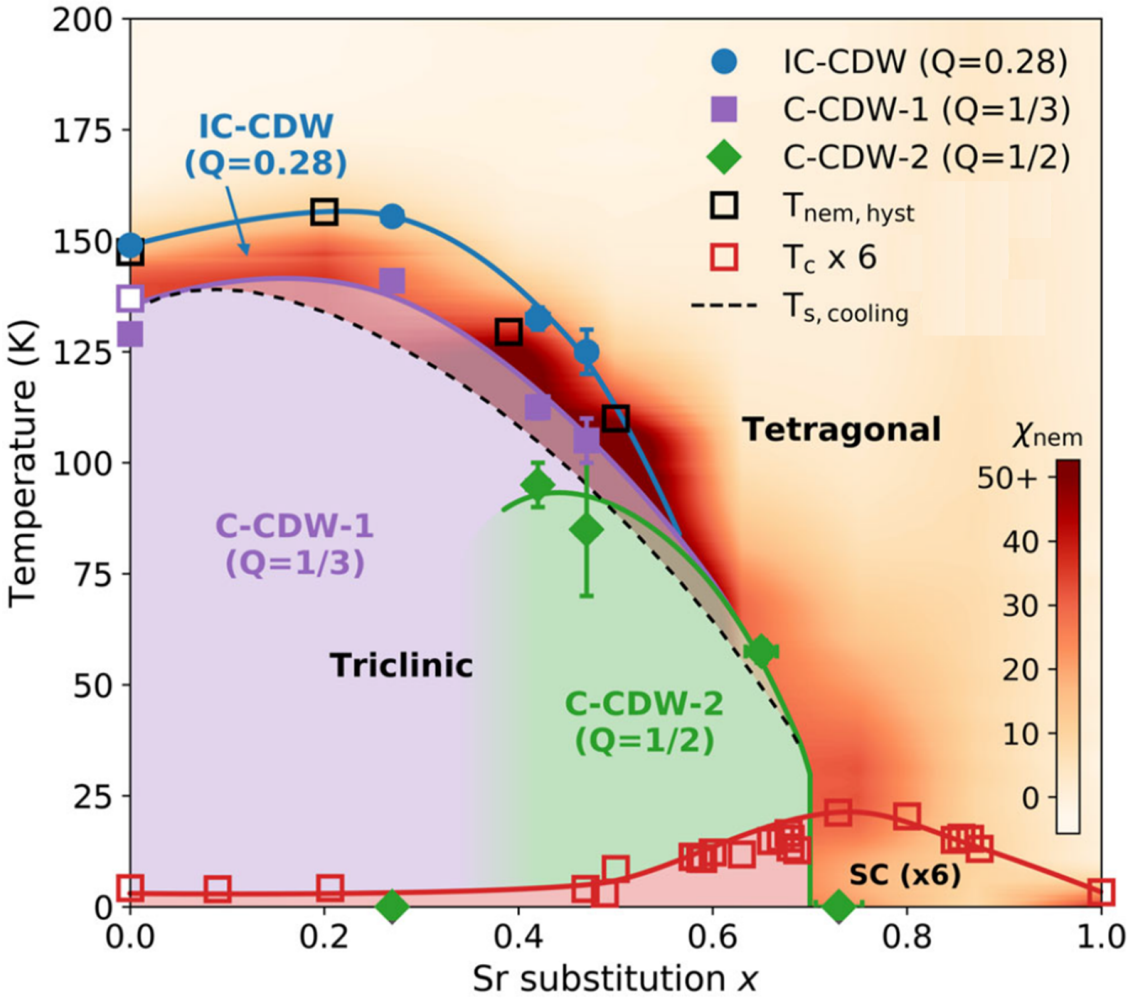

Figure 3.3: $Ba_{1-x}Sr_xNi_2As_2$ phase diagram at ambient pressure showing the triclinic state, IC-CDW, C-CDW1, C-CDW2, superconductivity state, as well as, an overlap of the nematic susceptibility. [3]

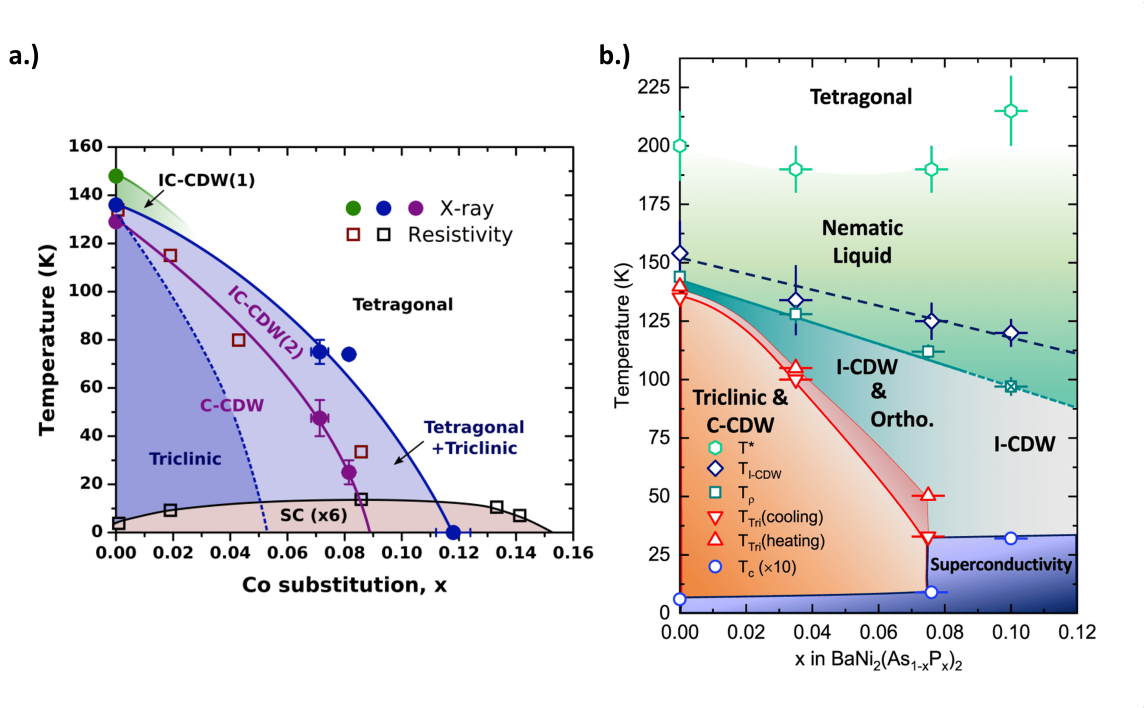

Figure 3.4: **a.)** $BaNi_{2-x}Co_xAs_2$ phase diagram [2]. **b.)** $BaNi_2As_{2-x}P_x$ phase diagrams [77]

charge density wave state (C-CDW2) in the triclinic state at $Q = (0, 0.5, 0)_{tri}$. The following sections of this chapter will spell out the appearance and evolution of these CDW states in three separate regions of the $Ba_{1-x}Sr_xNi_2As_2$ phase diagram: a low Sr content region ($0 < x < 0.4$), an intermediate Sr content region ($0.4 < x < 0.6$), and a near critical T_c Sr content region ($0.6 < x < 1$). ARPES measurements of $Ba_{1-x}Sr_xNi_2As_2$ have shown no Fermi surface nesting evidence of these charge density waves and instead show a Lifshitz transition near the critical Sr concentration, as well as, Fermi surface nesting evidence for the nematic state

Interestingly, one may also view the phase diagram shown in Figure 3.3 in reverse from x=1 to x=0.71 noting a 6 fold increase in T_c for a conventional superconductor where the only notable other change is an increase in nematic susceptibility. As discussed in Chapter 1, BSC theory for a phonon mediated pairing mechanism shows T_c being primarily driven by the Debye frequency and the density of states. Between x=1 and x=0.71, these factors remain steady and are unable to explain the large increase seen in T_c [65].

Lederer [78] has shown that nematic fluctuations coupled to a weakly interacting conventional superconductor can dramatically increase T_c. Nematic fluctuations may induce an attractive interaction between fermions for momentum transfers sufficiently larger than the nematic correlation lengths. This potential takes the the form of,

$$V_{nem}(k, q) = -h(k)\delta(k - q) \tag{3.1}$$

where $h(k)$ governs the coupling between fermions and the nematic state. Lederer

then shows a new pairing eigenvalue, $\lambda = \lambda_0 + \delta\lambda$, where λ_0 is pairing eigenvalue expected in conventional phonon-mediated pairing and $\delta\lambda$ is the additional piece coming from interactions with the nematic state. The assumption is made that $\lambda_0 > \delta\lambda$ so that phonon mediation remains the dominate pairing mechanism. The corresponding changes to T_c and the gap structure are then calculated as,

$$\frac{T_c}{T_{c0}} \approx e^{\delta\lambda/\lambda_0^2} \tag{3.2}$$

$$\frac{\Delta}{\Delta_0} \approx 1 + \left(\frac{1}{\lambda_0}\right)\left(\frac{h(k)}{v_F(k)} - \left[\frac{h(k)}{v_F(k)}\right]_{max}\right) \tag{3.3}$$

where $v_F(k)$ is the Fermi velocity. Note that T_c enhancement can become large despite $\delta\lambda/\lambda_0$ being small if $\delta\lambda \geq \lambda_0^2$. Additionally note that the introducing the nematic attraction to BCS theory has broken the inherently s-wave symmetry of the gap function.

ARPES measurements of $Ba_{1-x}Sr_xNi_2As_2$ have shown no Fermi surface nesting evidence of the charge density waves. However, they do show a Lifshitz transition near the critical Sr concentration, as well as, Fermi surface nesting evidence for the nematic state (Figure 3.5) [79].

3.2 Low Sr Content Region

Near x=0 both the IC-CDW and C-CDW1 charge density wave states can be observed in x-ray diffraction [2, 3]. Figure 3.6 shows the onset of the $Q = 0.28$ IC-CDW at 144 K, about 10 K above the triclinic structural distortion. The signal for the IC-CDW is shown

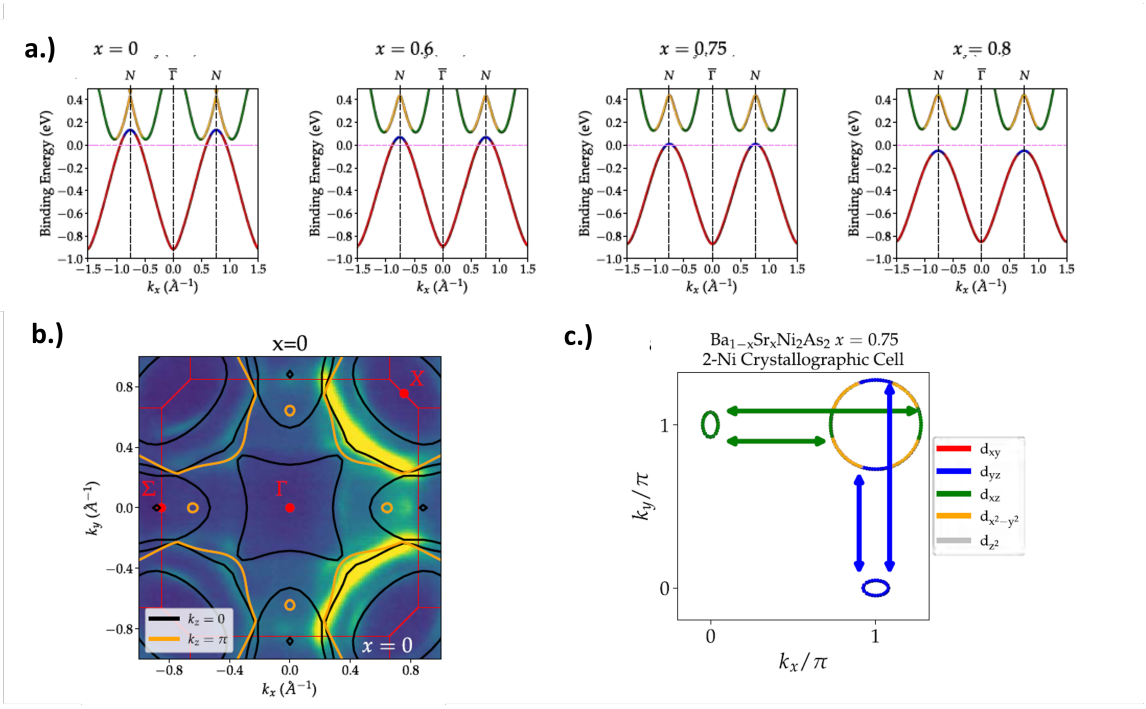

Figure 3.5: A summery of ARPES measurements on $Ba_{1-x}Sr_xNi_2As_2$ [79]. **a.)** A series of band energies for $Ba_{1-x}Sr_xNi_2As_2$ from ARPES showing a Lifshitz transition at x=0.75. **b.)** Fermi surface of $BaNi_2As_2$ showing no evidence of Fermi surface nesting for the IC-CDW or C-CDW1. **c.)** A sketch of the Fermi surface at x=0.75, showing nesting evidence for the nematic state.

via a selected CDW X-ray peak at $(2.72, -2, 9)_{tet}$, a satellite peak of the $(3, -2, 9)_{tet}$ tetragonal Bragg peak. As temperature is decreased, the IC-CDW continues to grow in intensity until a triclinic structural distortion occurs at 135 K. Concurrently to the triclinc transition, the IC-CDW abruptly vanishes and is replaced by an incommensurate CDW at $Q_{tri} = 0.31$. Quickly upon cooling, this CDW undergoes a "lock-in" transition common to many CDWs (Figure 3.6-b) [2] and shifts from $Q_{tri} = 0.31$ to $Q_{tri} = 0.33$ becoming C-CDW1. Lock-in effects are typically a consequence of lattice pinning in other CDW materials [2, 3], suggesting that pinning plays an important role for this particular CDW phase. Once C-CDW1 has locked into $Q_{tri} = 0.33$, it continues to exist down to a base temperature of 11 K.

One may assume that IC-CDW and C-CDW1 are the same charge density seen in two different coordinate systems due to having a smaller difference in Miller index value. However, the positions of IC-CDW and C-CDW1 are separated by nearly 20° and reside in very different regions of momentum space [2, 3] (Figure 3.7).

Elastoresistance measurements taken by Eckberg on $BaNi_2As_2$ in the tetragonal state have shown a clear nematic susceptibility signal along the B_{1g} $(x - y)$ symmetry channel just above the triclinic distortion (Figure 3.8) [65]. Particularly striking about this signal though is the opening of a hystersis gap. This hysteresis in elastoresistance is thought to arise due to the domain formation of an ordered nematic phase in $Ba_{1-x}Sr_xNi_2As_2$. In Figure 3.8-c, Eckberg plots the nematic susceptibility (slope of $\Delta R/R(\%)$), width of the hysteresis, and the intensity of the IC-CDW as a function of temperature for $BaNi_2As_2$. From this plot we find a strong correlation exists between the IC-CDW and the width of the hysteresis, where this width can interpreted as the strength of the nematic

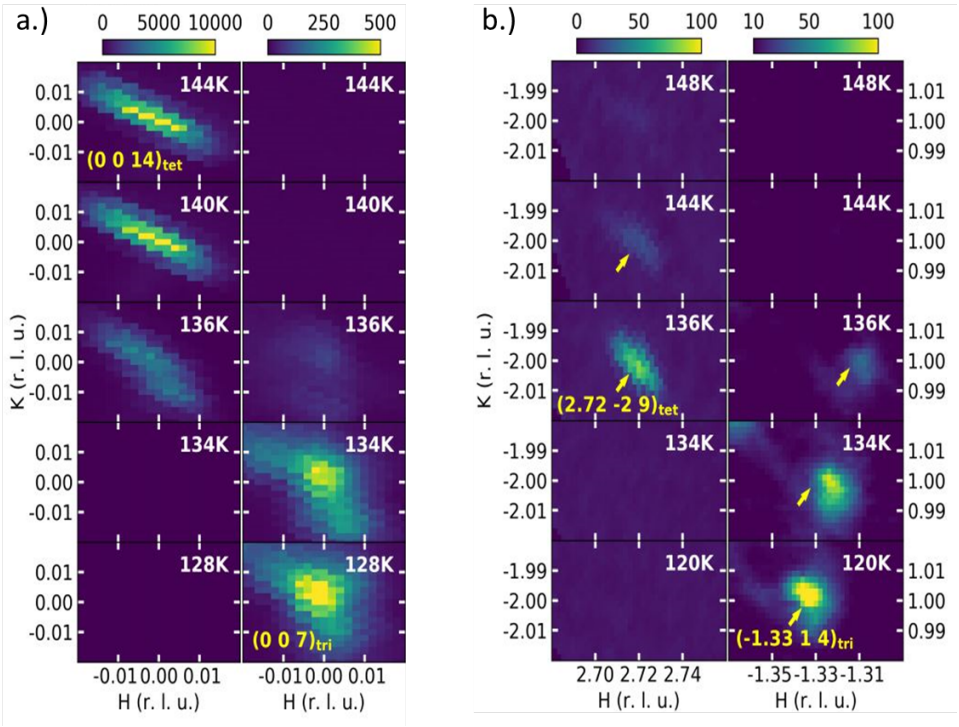

Figure 3.6: Selected x-ray diffraction data of $BaNi_2As_2$. **a.)** X-ray data showing the structural transition from tetragonal to triclinic via the disappearance of the $(0, 0, 14)_{tet}$ Bragg peak and the appearance of the $(0, 0, 7)_{tri}$ peak occurring near 135 K. **b.)** X-ray data showing the appearance and extinction of the $Q_{tet} = 0.28$ IC-CDW phase via the $(2.72, -2, 9)_{tet}$ satellite peak, as well as, the appearance and lock-in transition of the $Q_{tri} = 0.33$ C-CDW1 phase via the $(-1.33, 1, 4)_{tri}$ peak. The extinction of the IC-CDW and the appearance of the C-CDW1 occurs simultaneously with the triclinic structural distortion. [2]

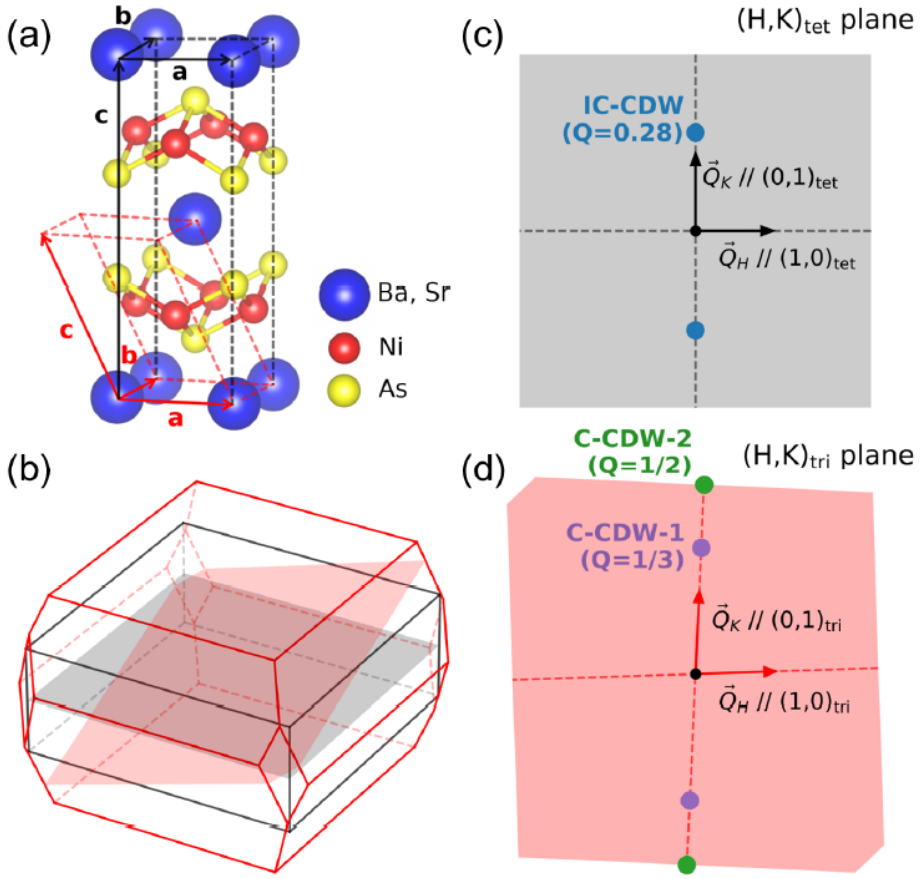

Figure 3.7: Geometric illustrations demonstrating the separate identities of C-CDW1, C-CDW2, and IC-CDW. **a.)** The unit cells for the tetragonal and triclinic phases of $Ba_{1-x}Sr_xNi_2As_2$. **b.)** The Brillouin zone boundaries of tetragonal (black lines) and triclinic (red lines) phases. The planes colored in black and red represent HK planes in the tetragonal and triclinic phases, respectively. **c.)**, **d.)** The positions in momentum space of the IC-CDW, C-CDW1, and C-CDW2 phases on the colored HK planes noted in panel **b**. [3]

order. The IC-CDW and the nematic order appear together at 148 K, scale together in intensity, and abruptly vanish at the triclinic distortion. As will be presented throughout this chapter, the correlation between the IC-CDW and the nematic order is strong and implies the two phases are related to a shared underlying mechanism.

3.3 Intermediate Sr Content Region

Between x=0.4 and x=0.6, the charge order in $Ba_{1-x}Sr_xNi_2As_2$ changes it's behavior. IC-CDW forms above the triclinic transition and then abruptly vanishes at the transition line, now lowered to about 110 K. C-CDW1 then forms in it's place. In this intermediate region however, a new charge order, C-CDW2 $Q = (0, 0.5, 0)_{tri}$, begins to form further than in temperature from C-CDW1 [3] (Figure 3.9). For a narrow window of x about x=0.45, we find that both C-CDW1 and C-CDW2 both co-exist down to base temperature (Figure 3.9-d). Towards the end of this intermediate region, C-CDW2 transition temperature rises closer to the triclinic transition line as C-CDW1 begins to disappear from the system.

As Sr content increases in this intermediate region, the window for nematic order existence above the triclinic distortion begins to narrow. The IC-CDW existence window also begins to narrow in this region. Both the IC-CDW intensity and the hysteresis width continue to scale together as a function of temperature, further implying a strong relationship between the two phases [3, 65]

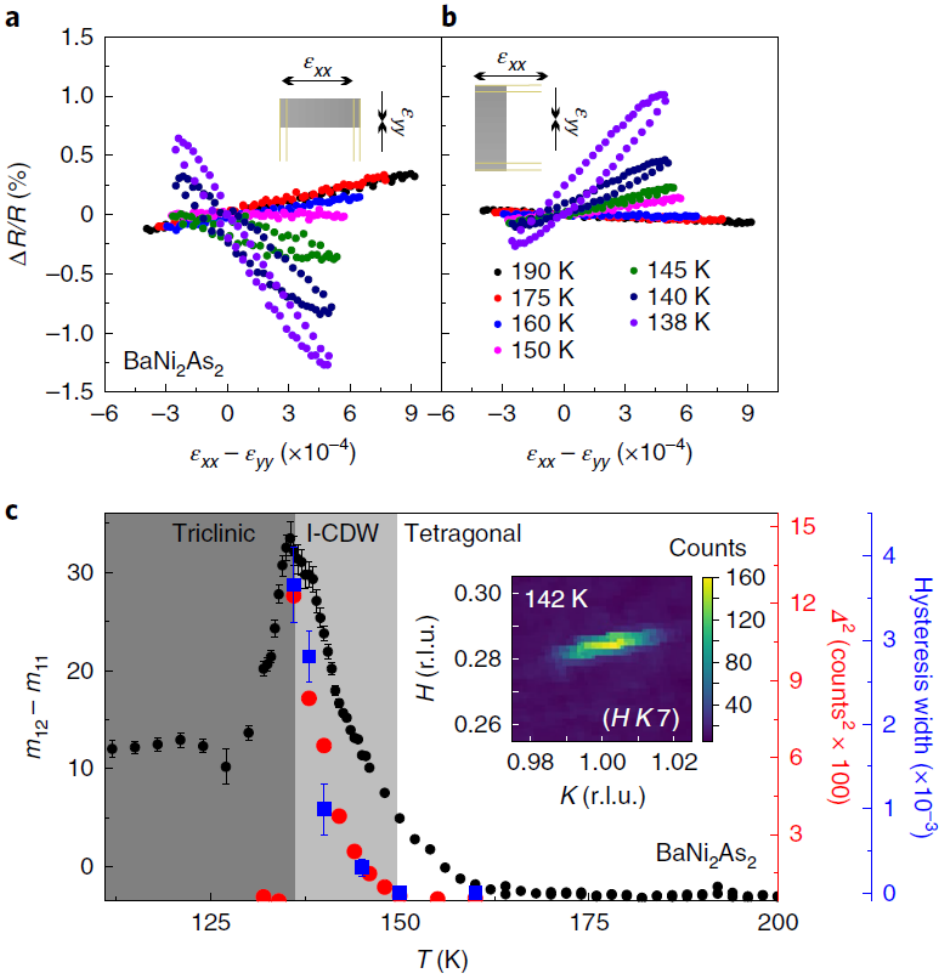

Figure 3.8: **a.)** and **b.)** Elastoresistance measurements of $BaNi_2As_2$ taken by Eckberg in two different orientations probing the B_{1g} symmetry channel. The slope in the signal of $\Delta R/R(\%)$ is a measure of the strength of nematic susceptibility. The size of the width of the hysteresis opening is a measure of the strength of nematic order. As temperature is lowered from 190 K towards the triclinic distortion at 135 K the susceptibility grows. Nematic order becomes present starting near 145 K. **c.)** Measurements of nematic susceptibility (black), IC-CDW intensity (red), and elastoresistance hysteresis width (blue) versus temperature. The temperature regions for tetragonal order, IC-CDW plus tetragonal order, and triclinic order are shown as the white, gray, and dark gray shaded regions respectively. INSERT: X-ray diffraction data of the $(0.28, 1, 7)_{tet}$ satellite peak representing the IC-CDW order. [65]

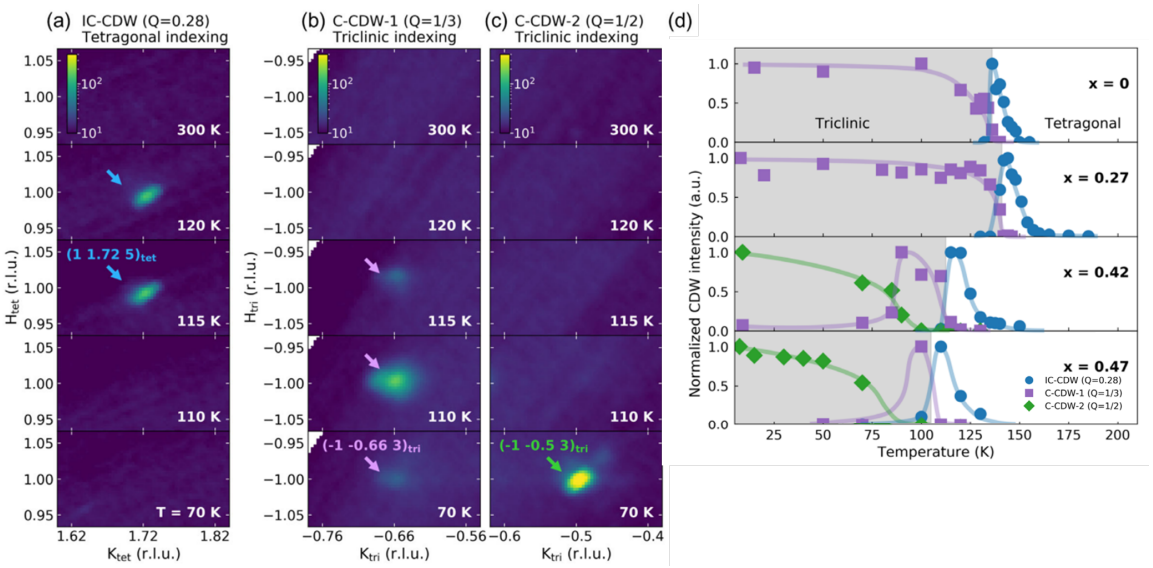

Figure 3.9: **a.)**, **b.)**, and **c.)** X-ray data of $Ba_{0.58}Sr_{0.42}Ni_2As_2$ showing the development of the IC-CDW, C-CDW1, and C-CDW2 for selected temperatures. The IC-CDW is shown to exist in a narrow range just above the triclinic distortion before vanishing. C-CDW1 appears at the triclinic distortion at 115 K but then decays as temperature is decreased. C-CDW2 is shown at 70 K, now appearing at lower temperatures and co-existing with C-CDW1. **d.)** Intensity versus temperature profiles for IC-CDW, C-CDW1, and C-CDW2 for selected values of x. For the intermediate region x values of 0.42 and 0.47, we find ranges of temperature where C-CDW1 and C-CDW2 co-exist. [3]

3.4 Near Critical Sr Content Region

Between x=0.6 and x=0.71 in the tetragonal phase, I have found that IC-CDW vanishes from the system, leaving no charge ordered states in the tetragonal phase for this region of the phase diagram [1] (Figure 3.10-a). Simultaneously for this region, Eckberg also finds that nematic order has vanished from the system [1, 65] (Figure 3.10-b), indicated by the complete reversibility of the elastoresistance signal. As shown in previous regions of the phase diagram, the IC-CDW and nematic order in $Ba_{1-x}Sr_xNi_2As_2$ are highly correlated together via the IC-CDW peak intensity and the nematic order elastoresistance hysteresis area. With the added observation that both orders vanish together, we claim that incommensurate charge order and nematic order not only scale together throughout $Ba_{1-x}Sr_xNi_2As_2$, but also mutually exist together throughout the entire phase diagram. This intimate tie between both orders suggest the possibility of a common mechanism driving both orders, requiring further study to elucidate.

When the system undergoes triclinic distortion in this region of the phase diagram, now at a reduced temperature of around 60 K, only the C-CDW2 $Q = 0.5$ order is observed [1]. This can be seen in Figure 3.11, where the triclinic order and C-CDW2 order can be seen appearing simultaneously at 60 K. The C-CDW1 order is now absent from the system, and no additional charge order can be seen in the triclinic system. Increasing Sr content beyond x=0.71 shows a vanishing of the triclinic and C-CDW2 order along with an enhancement of T_c up to 3.6 K [3, 65]. The vanishing of the IC-CDW near x=0.6 in the tetragonal phase, along with the shift of commensurate order from C-CDW1 to C-CDW2 in the triclinic phase, indicates that the charge ordered phases of $Ba_{1-x}Sr_xNi_2As_2$ develop

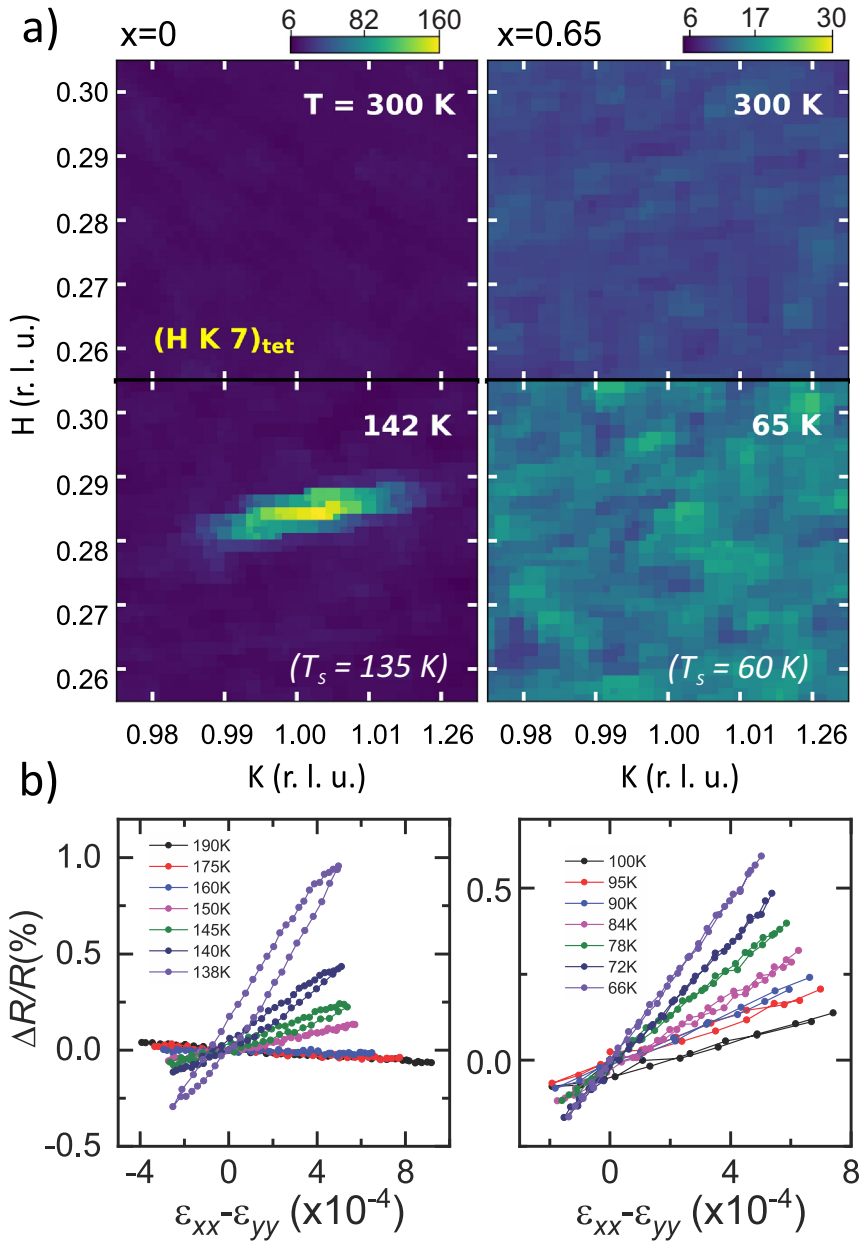

Figure 3.10: **a.)** HK cuts through momentum space centered on $(0.28, 1, 7)_{tet}$ at room temperature and relative temperatures above the triclinic structural distortion for x=0 and x=0.65 Sr concentrations. At room temperature for both concentrations no CDW is present. At x=0 the IC-CDW is observed at 142 K. At x=0.65, the IC-CDW is no longer observable above background levels. No other CDW peaks were detected in tetragonal phase for x=0.65 in all other regions of observed momentum space. X-ray data taken from supplementary figure S3 of [65]. **b.)** Elastoresitivity ratios for x=0 and x=0.63 for temperatures just above the triclinic distortion. In x=0, the signal is hysteretic with strain, indicating nematic order. In x=0.63, the signal is reversible with strain. The observation of nematic order and the IC-CDW occur simultaneously for $Ba_{1-x}Sr_xNi_2As_2$. [1]

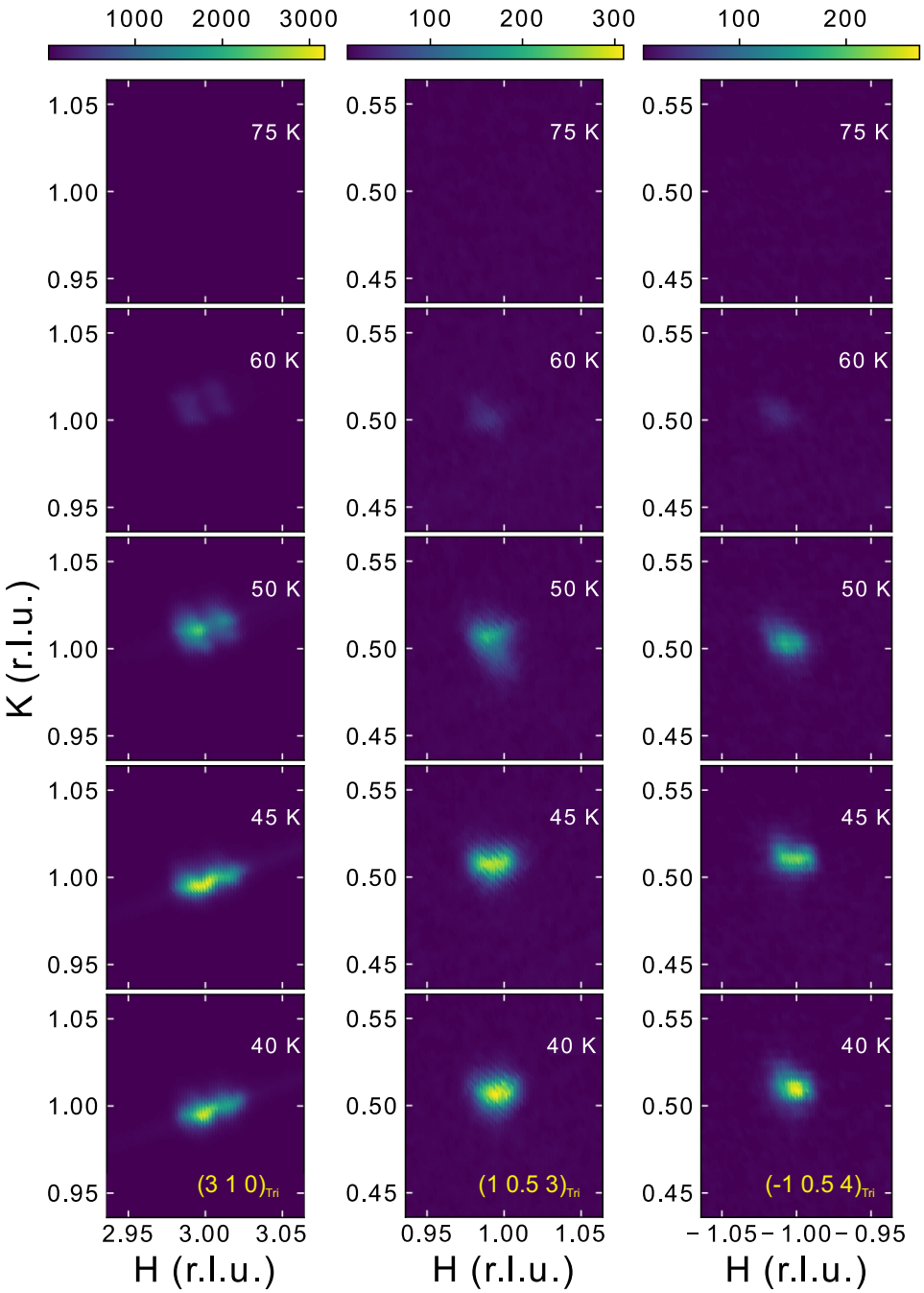

Figure 3.11: HK slices of X-ray diffraction for $Ba_{0.35}Sr_{0.65}Ni_2As_2$showing the onset of triclinic order at $(3, 1, 0)_{tri}$ and the onset of C-CDW2 at $(1, 0.5, 3)_{tri}$ and $(-1, 0.5, 4)_{tri}$.

in a complex way and are not simply tuned down to zero temperature.

Chapter 4: Charge Order Evolution in pressurized $BaNi_2As_2$

4.1 Introduction and Motivation

As demonstrated in Chapter 3, substitution of Ba for Sr in $Ba_{1-x}Sr_xNi_2As_2$ reveals a rich phase diagram containing complex charge order, nematic order, and enhanced superconductivity all while lacking any magnetism. This substitution of Sr for Ba is an example of "chemical pressure" due to Sr being smaller than Ba while also sharing the same number of valence electrons (and therefore, similar expected chemical properties). This shrinks the average unit cell while theoretically changing little about the chemical properties of the compound. With such dramatic changes occurring in $Ba_{1-x}Sr_xNi_2As_2$, natural questions arise over the role chemical pressure plays in causing these effects. To better understand this chemical pressure perturbation, I have studied and compared the effects of physically applied pressure on the charged ordered phases of $BaNi_2As_2$ via X-ray diffraction experiments using diamond anvil cells, and electrical transport measurements using piston pressure cells.

This chapter will outline my studies examining the evolution of charge order in $BaNi_2As_2$ as a function of applied pressure. The work presented here using DACs and XRD was performed in collaboration with EPEC group of Lawrence Livermore National Laboratory with X-ray data being taken at the 16-BMD beamline of Argon National

Laboratory. Work involving electrical transport and high pressure piston cells were performed here at QMC at UMD. The studies presented in this chapter have been developed into a manuscript, "Charge Order Evolution of Superconducting $BaNi_2As_2$ Under High Pressure" John Collini, et al, with submission to Physical Review B emanate. Discussion and comparison of these results with the ambient pressure studies of $Ba_{1-x}Sr_xNi_2As_2$ will be conducted in Chapter 5.

4.2 Methods

Single crystal x-ray diffraction measurements under high pressure were taken at the Argonne Advanced Photon Source (APS) 16-BMD beamline (Figure 4.1. Samples of single crystal $BaNi_2As_2$ were prepared in collaboration with the Equilibrium Physics at Extreme Conditions (EPEC) group of Livermore National Laboratory using a diamond anvil cell (DAC) with a diamond culet size of 500 m as previously outline in Chapter 2.3. The samples of $BaNi_2As_2$ were mounted on the diamond culet with their c-axis parallel to the culet's normal, parallel to the x-ray beam. Neon gas was used as a pressure medium and ruby florescence was used as a pressure manometer. A 200 μm diameter hole was drilled in the center of a stainless steel gasket. The gasket hole was filled with the sample, gas, and ruby. The starting pressure for the DAC was 2.4 GPa. A beamline mounted cryostat controlled the temperature of the DAC and had working base temperature of about 37 K. A gas membrane was used to control the pressure remotely from outside cryostat and the hutch. The workable rocking angle for the experiment (denoted Omega on 16-BMD) was limited by the gasket hole to a range of -4.5 degrees to 4.5 degrees.

Data were taken only on cooling for pressures 2.4 GPa, 5.4 GPa, 8.1 GPa, 9.5 GPA, and 10.5 GPa.

Additionally, room temperature powder X-ray diffraction measurements were taken at beamline 16-IDB of the APS by previous QMC student Daniel Campbell and myself. A rhenium gasket was indented to about 40 μm using 300 um culets, then a 100 um hole was drilled in the center. A powder of crushed BaNi2As2 crystals was loaded along with Cu powder and a ruby sphere. The ruby was used for initial offline pressure calibration, pressure during the measurement was ultimately determined from the [200] reflection of Cu using the the equation of state [80]. Mineral oil was used as the pressure medium, and a gas membrane was used to control pressure remotely from outside the hutch. High pressure electrical transport measurements were also performed up to 2.55 GPa using a piston-operated BeCu high pressure cell with Arcros Organics Perfluoro-compound FC-770™ acting as the pressure medium.

4.3 Low Pressure Region

I find that charge order in $BaNi_2As_2$ evolves under pressure in similar ways to Sr substitution with key notable differences (Figure 4.2). Starting at 2.4 GPa, I have detected all three charge orders (C-CDW1, C-CDW2, and IC-CDW) and the triclinic distortion seen previously for $Ba_{1-x}Sr_xNi_2As_2$ in chapter 3 (Figure 4.3). I find the IC-CDW onsets at 140 K, 20 K above the triclinic distortion observed here at 120 K. The IC-CDW then vanishes at 105 K in the triclinic phase. This marks a different behavior from $Ba_{1-x}Sr_xNi_2As_2$ where we would instead expect the IC-CDW to vanish very close

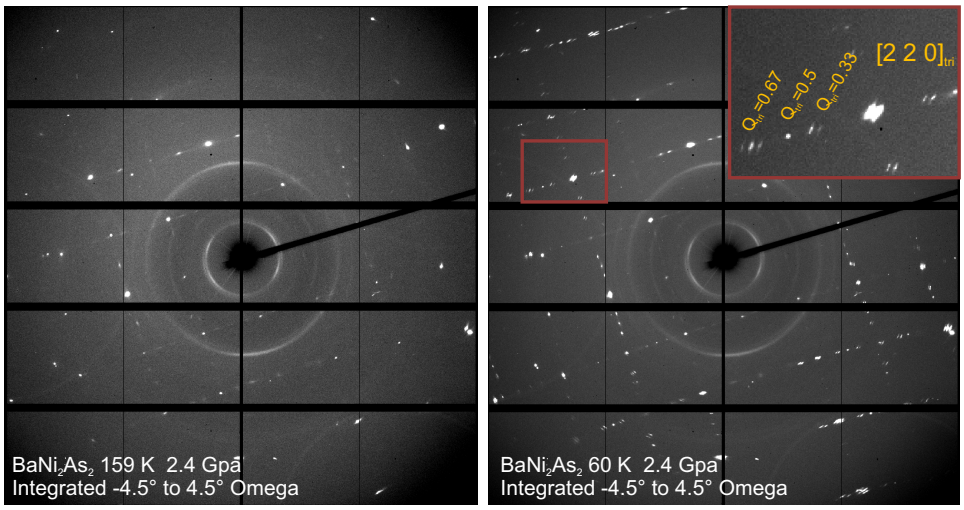

Figure 4.1: Single crystal x-ray diffraction images of $BaNi_2As_2$ at 2.4 GPa taken at (a) 159 K and (b) 60 K. Highlighted in (b) is the $[2\ 2\ 0]_{tet}$ zone. Comparing high to low temperatures, I find the introduction of satellite peaks through-out the diffraction pattern. Superlattice peaks found midway between zones are evidence for the Q=0.5 C-CDW2 and superlattice peaks found one third and two thirds to the next zone are evidence for the Q=0.33 C-CDW1. Each image was exposed while continuously rocking the sample from -4.5 to +4.5 Omega.

to the triclinic onset while still in the tetragonal phase [3]. For the commensurate charge order, C-CDW1 appears first at 110 K and C-CDW2 appears next at 105 K, both in the triclinic phase. C-CDW1 and C-CDW2 continue to coexist down to 60 K, the lowest temperature I measured for this pressure. This behavior, with the exception of a wide IC-CDW existence window in temperature, places $BaNi_2As_2$ at 2.4 GPa roughly in line with $Ba_{1-x}Sr_xNi_2As_2$ at an x between 0.4 and 0.5.

4.4 High Pressure Region and Piston Cell Resistance of $Ba_{0.30}Sr_{0.60}Ni_2As_2$

As pressure is increased, the three charge orders and the triclinic distortion have their onset temperatures decline and eventually vanish. At the next measured pressures of 5.3-5.6 GPa, C-CDW1 was not detected as far down as 49 K. C-CDW2 was first detected upon cooling at a temperature of 110 K for a pressure of 5.4 GPa. The triclinic onsets at 110 K for 5.4 GPa. Following this at 8.4 GPa, triclinic order and the C-CDW2 appeared together at 103 K (Figure 4.4). At higher measured pressures of 9.5 GPa and 10.5 GPa, the system remained tetragonal as far down as 37 K with no charge order or triclinic order detected.

In $Ba_{1-x}Sr_xNi_2As_2$, it was important to note that the extinguished C-CDW2 and triclinic distortion ended discontinuously as a function of Sr concentration before revealing the large enhancement in T_c [3,65]. As a function of pressure, we find a 8.4 GPa, 103 K C-CDW2 + triclinic state onset followed by a tetragonal only state at 9.5 GPa down to 37 K. This strongly suggests a similar discontinuous extinction of the C-CDW2 and triclinic phases. Additional evidence supporting a discontinuous vanishing can be seen in a piston

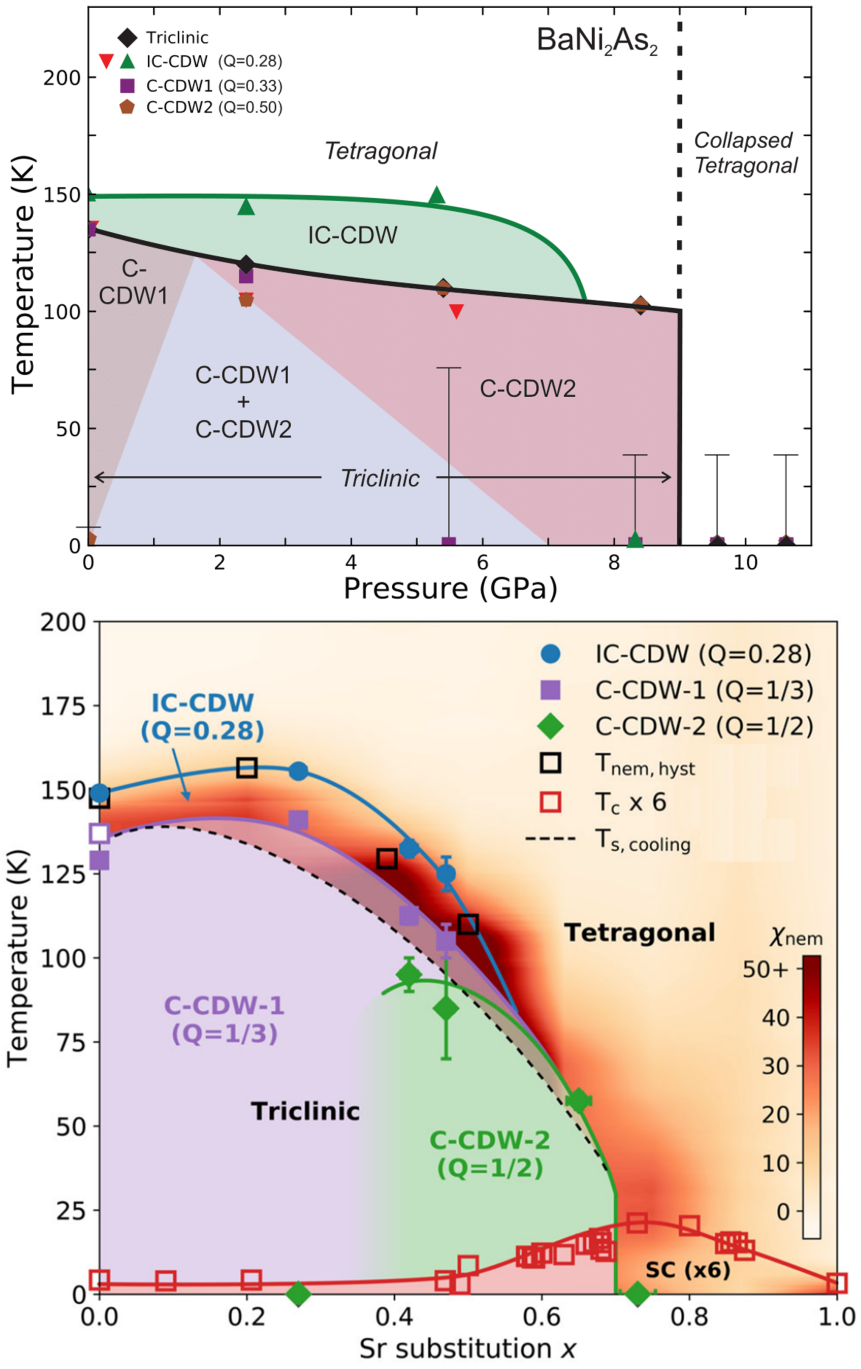

Figure 4.2: Pressure-temperature phase diagram of $BaNi_2As_2$ as determined by X-ray diffraction measurements. Highlighted are the IC-CDW, triclinic order, C-CDW1, and C-CDW2. A collapsed tetragonal phase is also highlighted and will be elaborated on in Chapter 5. The large error-bars seen at lower temperatures and higher pressures account for the absence of phases seen down to the lowest temperature measured for a given pressure. The $Ba_{1-x}Sr_xNi_2As_2$ phase diagram from Figure 3.3 is shown below it for direct comparison.

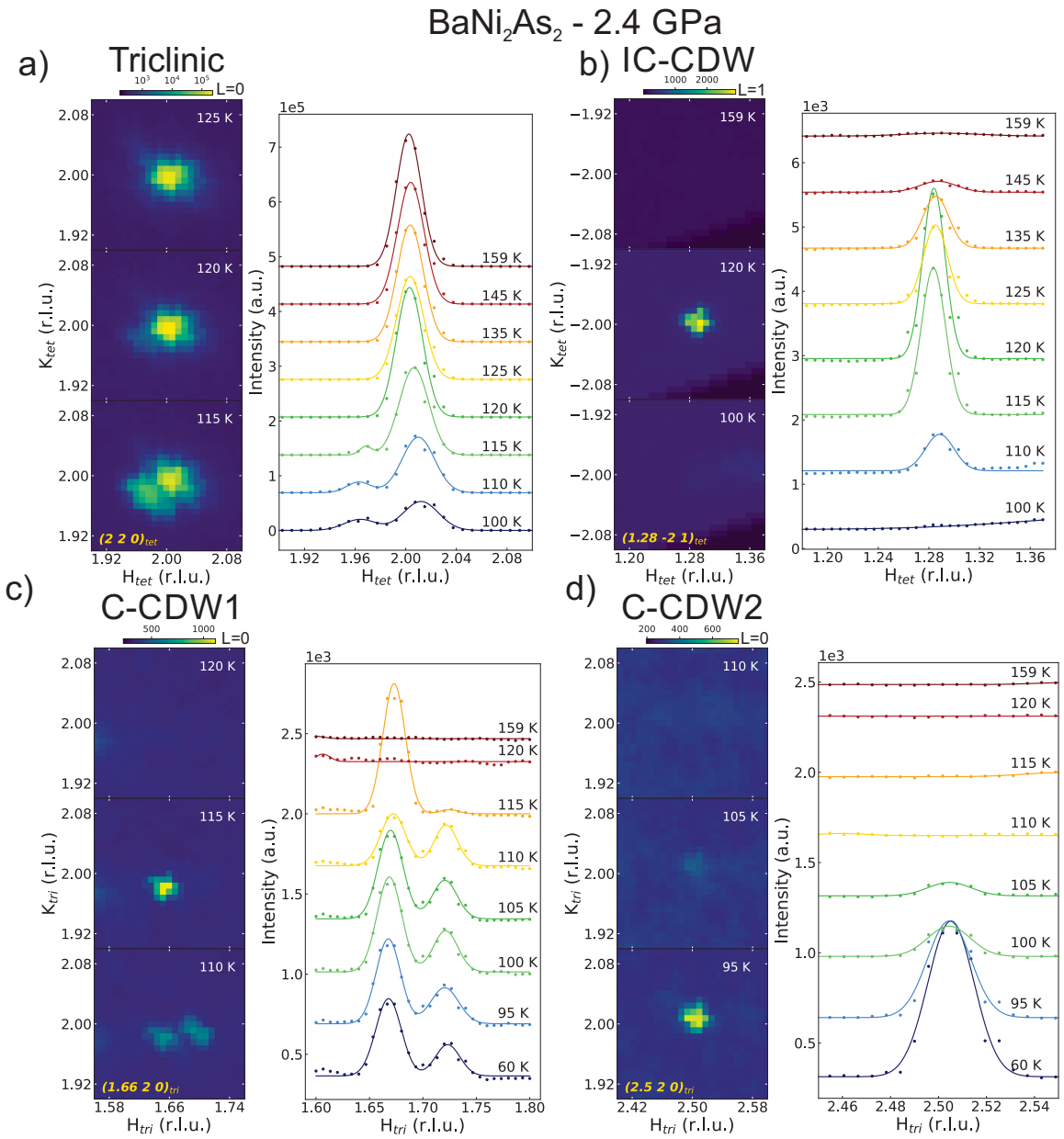

Figure 4.3: Four distinct features of $BaNi_2As_2$ at 2.4 GPa (Triclinic onset, IC-CDW, C-CDW1, and C-CDW2) shown as a function of decreasing temperature via momentum space plots and line cuts at a) $(2, 2, 0)_{tet}$, b) $(1.28, -2, 1)_{tet}$, c) $(1.66, 2, 0)_{tri}$, and d) $(2.5, 2, 0)_{tri}$. We find the IC-CDW onsets at a temperature of 145 K and a vanishes at 105 K. We find the triclinic order, C-CDW1, and C-CDW2 onset at temperature of 120 K, 110 K, and 105 K respectfully. Line cuts are presented with Gaussian fits at the peaks for guidance.

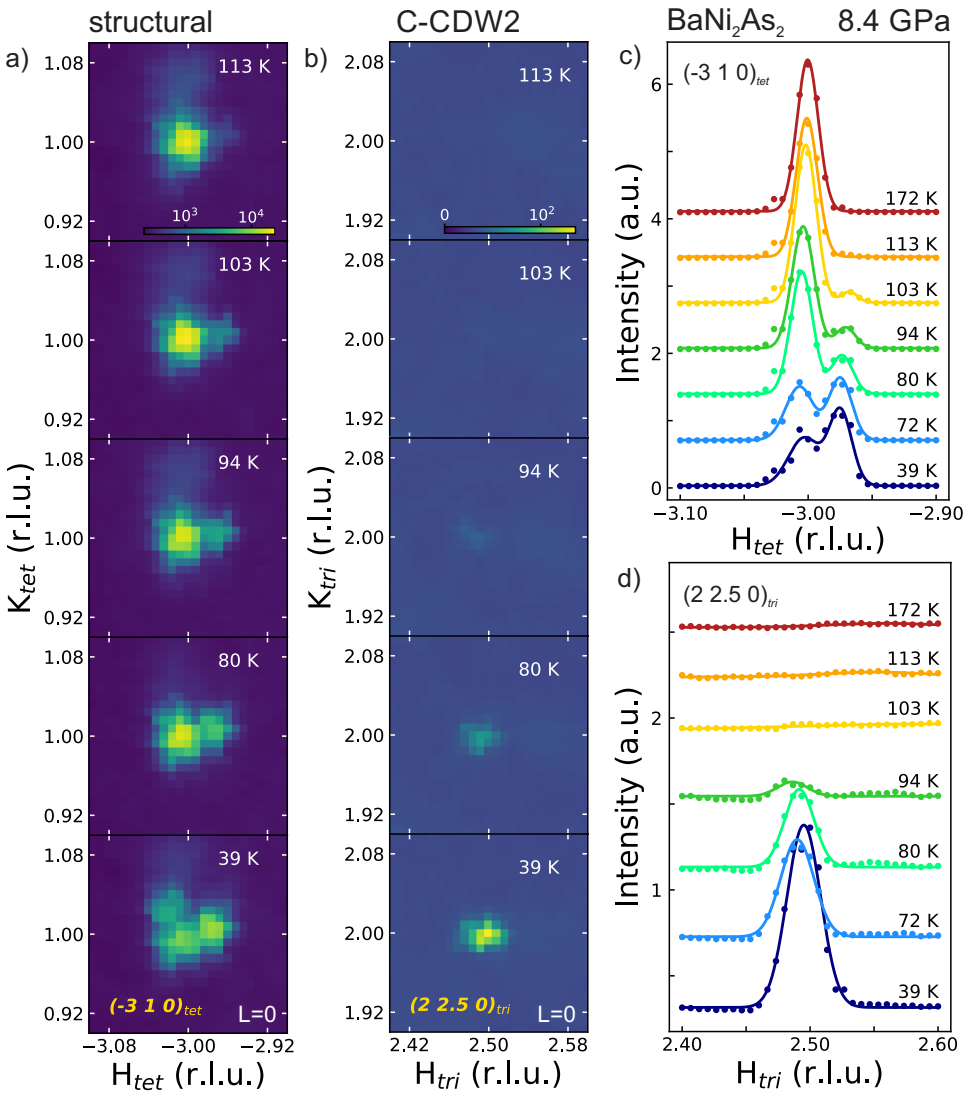

Figure 4.4: 8.4 GPa X-ray data and line scans of a) C-CDW2 and b) triclinic order as seen by the $(-3, 1, 0)_{tet}$ and $(2, 2.5, 0)_{tri}$. We find that both phases onset at 103 K.

pressure cell transport measurement of $Ba_{0.30}Sr_{0.60}Ni_2As_2$ (Figure 4.5). Between the narrowly separated pressures 0.1 GPa and 0.51 GPa, the sample of $Ba_{0.30}Sr_{0.60}Ni_2As_2$ goes from an ambient-pressure-like state of a C-CDW2 + triclinic phase with an onset temperature of 60 K to a complete vanishing of both phases followed by an enhanced superconducting temperature of 3.6 K. This enhanced T_c state persists through the highest recorded pressure of 2.55 GPa. The behavior induced in pressurized $Ba_{0.30}Sr_{0.60}Ni_2As_2$, coupled with our x-ray observations in pressurized $BaNi_2As_2$, and in previously reported ambient pressure $Ba_{1-x}Sr_xNi_2As_2$, point to there being a discontinuous phase boundary between triclinic + C-CDW2 and the enhanced superconducting state induced by a shrinking lattice caused by Sr isovalent substitution, pressure, or a combination of both.

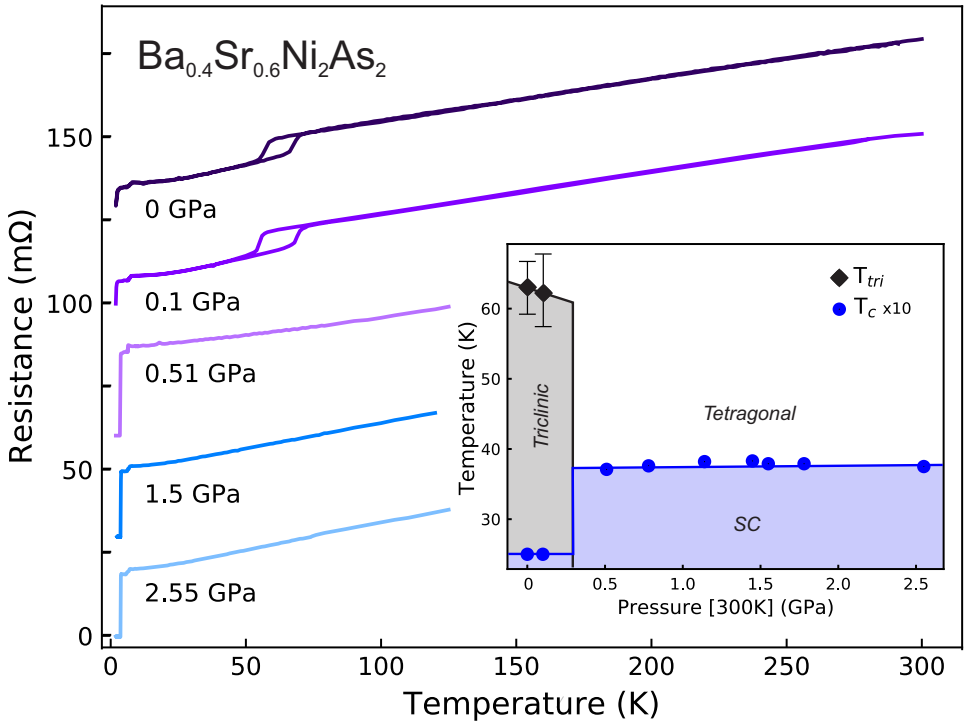

Figure 4.5: Resistance vs temperature of a $Ba_{0.30}Sr_{0.60}Ni_2As_2$ sample shown at selected pressures demonstrating the discontinuous phase boundary between the C-CDW2 + triclinic state and tetragonal state. Curves has been separated for readability. INSERT: Pressure-temperature phase diagram of $Ba_{0.30}Sr_{0.60}Ni_2As_2$ taken from the resistivity data. T_c has been amplified by 10 for visibility.

Chapter 5: Discussions and Conclusions

5.1 Comparing $Ba_{1-x}Sr_xNi_2As_2$ and pressurized $BaNi_2As_2$ to other systems

Lattice parameter studies for many systems in the 122 $ThCr_2Si_2$-type crystal structure find that the c-axis, the a-axis, and a collapsed tetragonal (CT) phase are major drivers for the interesting physics seen in their systems, such as $CaFe_2As_2$ [81–85], $BaFe_2As_2$ [86, 87], $SrFe_2As_2$ [88], $CaRbFe_4As_4$ [89], $LaRu_2P_2$ [90], and $SrCo_2As_2$ [91]. A CT phase occurs when either physical or chemical pressure is applied to a $ThCr_2Si_2$-type system and the lattice makes a sudden rigid shift in dimensions without changing the space group. For the case of the 1-2-2 Fe-pnictides, there is a rise and fall in the a-axis with a valley to peak size ranging from 0.05 Å to 0.15 Å, a discontinuous jump in the As-As interlayer distance about 3 Å, a flattening of the FeAs layer, and sometimes a discontinuous jump in the c-axis (Figures 5.1 and 5.2). This collapse quenches the Fe moment, suppressing magnetic order, and reveals high temperature superconductivity [92]. The discontinuous jump in the As-As distance for CT phases is theorized to be caused by a hybridization of the As atoms along the c direction, and is thought to be a major driver into this collapsed state.

To compare to the CT driven physics in these $ThCr_2Si_2$-type systems, lattice constants of $BaNi_2As_2$ up to 17 GPa at 300 K were measured from powder x-ray diffraction with

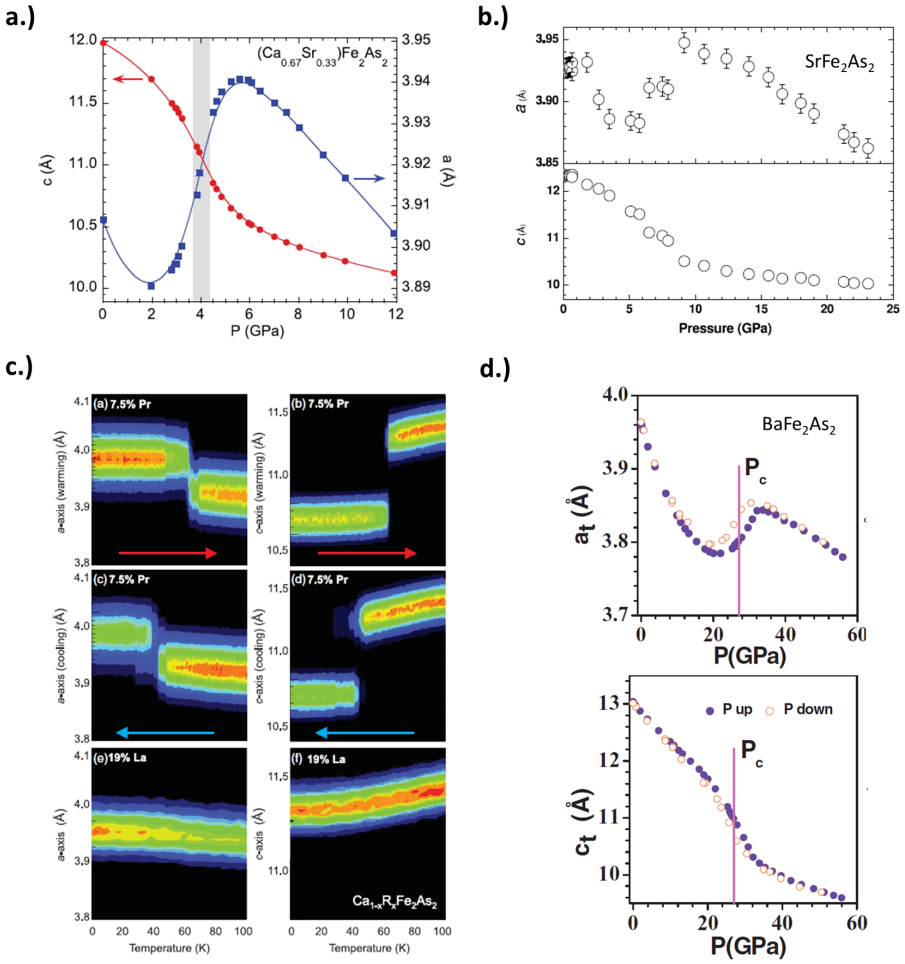

Figure 5.1: Lattice parameters showing the CT phase of various 1-2-2 Fe-pnictides taken from literature. **a.)** $Ca_{0.67}Sr_{0.33}Fe_2As_2$ CT phase under pressure [85]. **b.)** $SrFe_2As_2$ CT phase under pressure [88]. **c.)** $Ca_{1-x}R_xFe_2As_2$ (R=Rare Earth) CT phase at low temperature and ambient pressure [81]. **d.)** CT phase in $BaFe_2As_2$ under pressure [86].

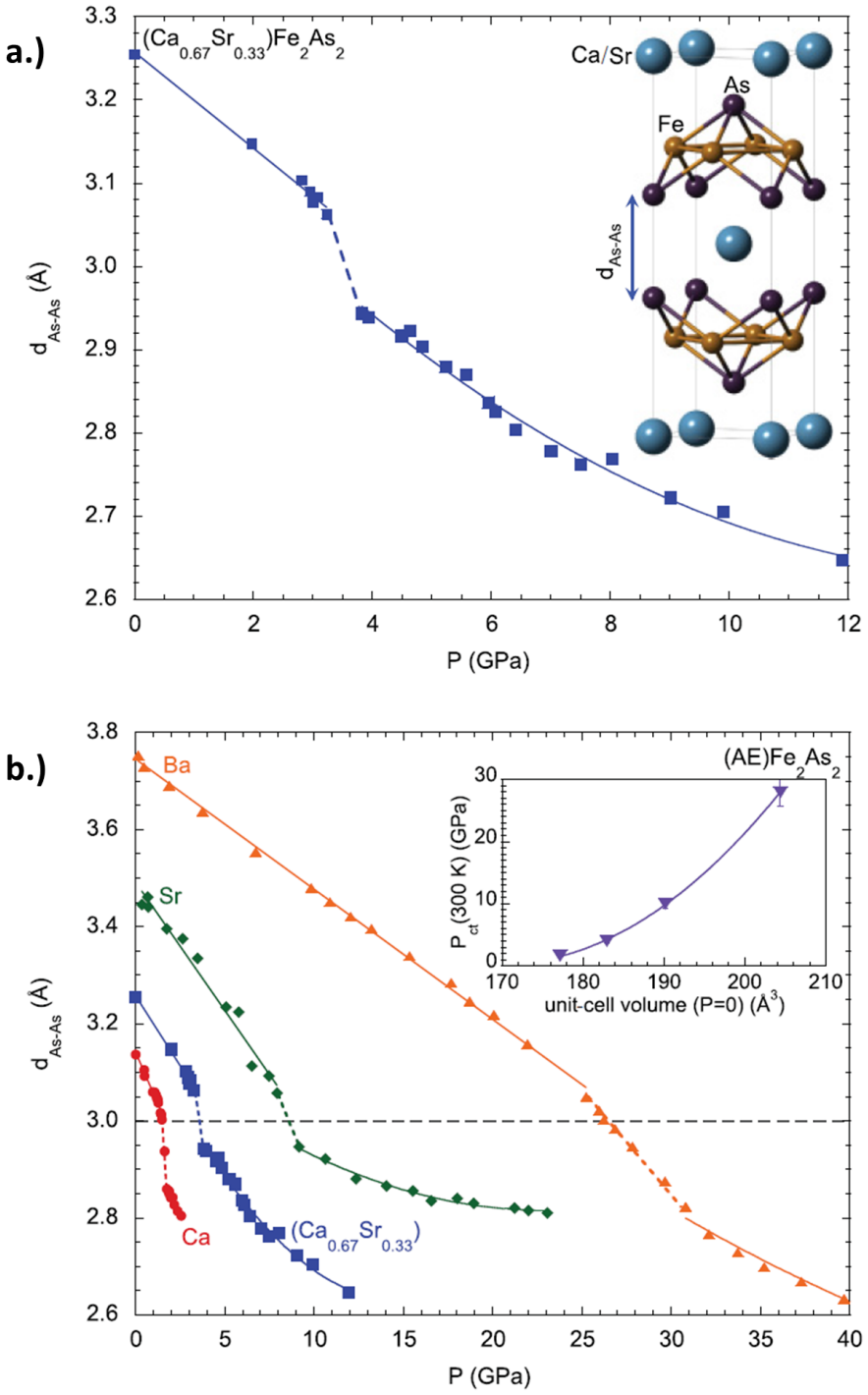

Figure 5.2: As-As spacing showing the CT phase of various 1-2-2 Fe-pnictides under pressure from literature taken from [85].

the help of previous student Daniel Campbell and compared with $Ba_{1-x}Sr_xNi_2As_2$ at 250 K (from supplement in reference [65]) and in Figure 5.3. I note the difference in temperatures between the two data sets of pressurized $BaNi_2As_2$ at 300 K and at $Ba_{1-x}Sr_xNi_2As_2$ 250 K, but argue it is not significant enough to alter any meaningful comparisons. At 300 K, $BaNi_2As_2$ has reported c-axis and a-axis values of 11.6190 Å and of 4.1474 Å respectively [93]. $SrNi_2As_2$ has reported values of 10.290 Å and 4.154 Å respectfully [94]. The 250 K $Ba_{1-x}Sr_xNi_2As_2$ lattice parameter dataset has values of 11.6423 Å and 4.1442 Å for x_{Sr}=0, as well as, 10.2515 Å and 4.1564 Å for x_{Sr}=1. The differences between 300 K and 250 K lattice parameters for $BaNi_2As_2$ and $SrNi_2As_2$ are fractions of a percent and therefore appropriate for our comparisons and discussions.

I find there is a correlation between Sr substitution and pressurization of $BaNi_2As_2$ for the c-axis. In both systems, the c-axis decreases monotonically at a similarly scaled rate. To directly compare these systems, pairs of x_{Sr} and pressure were chosen by where they have equal c-axis values. To do this, I linearly interpolated values for the c-axis $BaNi_2As_2$ pressurized data set, then, noted the x_{Sr} values in the $Ba_{1-x}Sr_xNi_2As_2$ data set where they equal the interpolate $BaNi_2As_2$ c-axis values. A line, $P(x_{Sr}) = mx_{Sr}$, is fit to this result (Figure 5.3 insert). From the fit I find m to be 13.34 ± 0.05 GPa/Sr, demonstrating a simple linear relationship between chemical pressure and physical pressure for $BaNi_2As_2$ along the c-axis. I test this correlation model with noteworthy points in x_{Sr}: the discontinuous phase boundary and maximum T_c, $x_C = 0.71$, as well as, the approximate ending point for the IC-CDW and nematic order, $x_{IC-CDW} = 0.55$. Using this linear relationship, we find $P(x_C) = 9.47$ GPa and $P(x_{IC-CDW}) = 7.34$ GPa, closely predicting the corresponding events in the pressure.

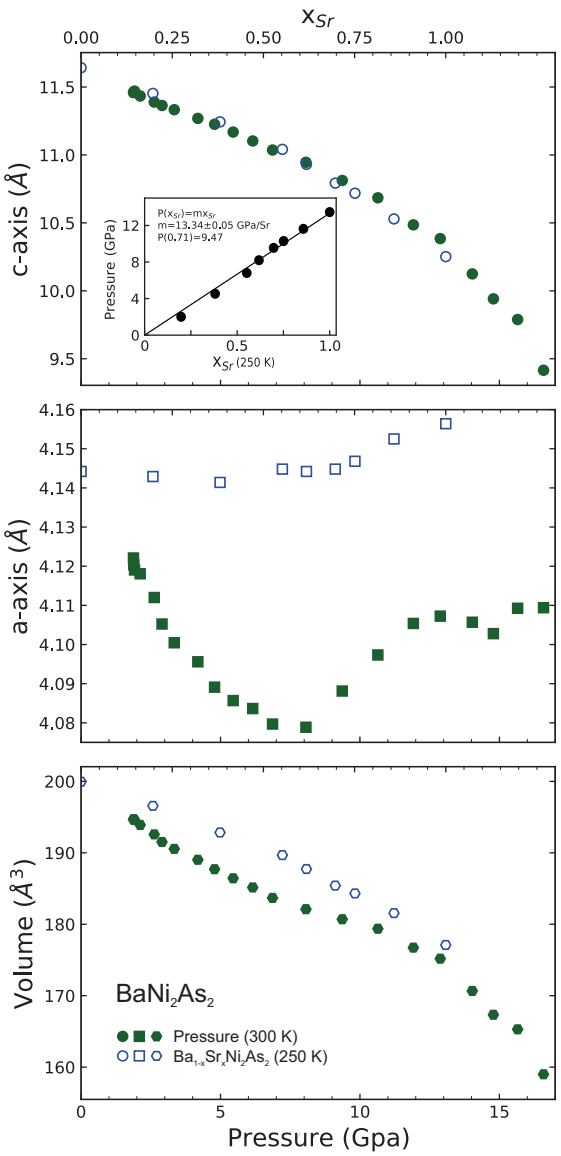

Figure 5.3: Lattice constant and unit cell volume data of 250 K $Ba_{1-x}Sr_xNi_2As_2$ (blue, open points) and 300 K pressurized $BaNi_2As_2$ (green, closed points) taken from powder x-ray data. The 250 K $Ba_{1-x}Sr_xNi_2As_2$ data were taken from the supplement of reference [65]. The 300 K $BaNi_2As_2$ data were taken from pressurized powder x-ray diffraction data using the [110] peak for the a-axis and the [112] peak for the c-axis. The $Ba_{1-x}Sr_xNi_2As_2$ scale was chosen such that the c-axis of both systems align, visually showing the correlation between the two systems. INSET: points in pressure plotted against equivalent points in Sr substitution for alike c-axis values. A line, $P(x_{Sr}) = mx_{Sr}$, is fit to the correlation, yielding $m = 13.34 \pm 0.05$ GPa/Sr as the correlation constant relating the c-axis of pressure to the c-axis of $Ba_{1-x}Sr_xNi_2As_2$.

For the a-axis I instead find a deviation between Sr and pressure (Figure 5.3). Eckberg et al have shown for $Ba_{1-x}Sr_xNi_2As_2$ the a-axis remains mostly constant until a small rise near $SrNi_2As_2$ at x_{Sr} 0.7 [65]. As a function of pressure, we find an immediate sharper decline of the a-axis, until a rise and fall is encountered between 8 GPa and 13 GPa with a valley-to-peak size of ~ 0.03 Å (Figure 5.3). The start of this pressurized a-axis expansion coincides with a small rise seen in the a-axis of $Ba_{1-x}Sr_xNi_2As_2$. These both occur when the c-axis of both systems is decreased to ~ 10.8 Å. Eckberg also noted that the rise in the a-axis seen in $Ba_{1-x}Sr_xNi_2As_2$ coincides with d_{As-As} crossing 3 Å [65], the same threshold noted for the Fe-pnictide collapsed tetragonal phases.

The a-axis expansion seen in pressurized $BaNi_2As_2$ and $Ba_{1-x}Sr_xNi_2As_2$ indicates that a CT transition is developing. The onset of this CT transition in x_{Sr} and pressure coincides with the charge and triclinic orders vanishing discontinuously. During this collapsed tetragonal transition, we speculate that the Ni-As layers begin to flatten along the ab plane for the duration of this a-axis expansion, similar to the flattening Fe-As layers in the CT phase of Fe-pnictides. We infer the CT phase in $BaNi_2As_2$ plays a key role in extinguishing charge order, enhancing nematic susceptibility, and enhancing the superconducting temperature. Open questions remain as to how this CT phase suppresses charge order for $BaNi_2As_2$, and why this CT phase is subtler than those found in the Fe-pnictides. Further study into the lattice parameters, As-As distances, and Ni-As angles for this region of pressure and temperature may shed light on the suppression mechanism for charge order and superconductive enhancement mechanism in $BaNi_2As_2$.

5.2 $BaNi_2As_2$ CDW Characterization

Within the last two years, a bevy of new studies on $BaNi_2As_2$ have emerged. In this section, I will briefly present early findings from a few of these studies that help characterize the charge order I have studied in $BaNi_2As_2$. As discussed in Chapter 2, charge density waves can roughly come in one of three different types: type I Peierls-driven, type II Q dependent EPC-driven, and type III unconventionally-driven. To disseminate the origins of each charge order in $BaNi_2As_2$, one should view the Q dependent phonon spectra, the Fermi surface, the Q dependent dielectric response, as well as, any additional measurements associated with electron-phonon coupling (Figure 5.4). Studies of the $BaNi_2As_2$ Fermi surface from ARPES have shown no evidence for Fermi surface nesting for the IC-CDW or C-CDW [95,96]. Measurements of the phonon energies from inelastic X-ray scattering meanwhile do show phonon softening at Q_{IC-CDW} in the tetragonal phase. However, the softening is wide (0.05 r.l.u. along K) and strangely, softens to zero energy starting at 180 K, which is well above the onset temperature of IC-CDW seen in X-ray [97,98]. Seemingly related to this are measurements seen in Raman spectroscopy, where it is observed that the E_{1g} activated mode begins splitting near 200 K [77], with the authors claiming this high temperature region to be an "electronic nematic liquid".

Given the lack of Fermi surface nesting and the wide Kohn's anomaly seen, one many be tempted to prematurely place the $BaNi_2As_2$ charge order into type II. However, given the clear relationship of the IC-CDW to the nematic order, the high temperature phonon softening and Raman peak splitting, and the relationship between the CT phase and C-CDW2, $BaNi_2As_2$ charge order could stem from an unconventional mechanism.

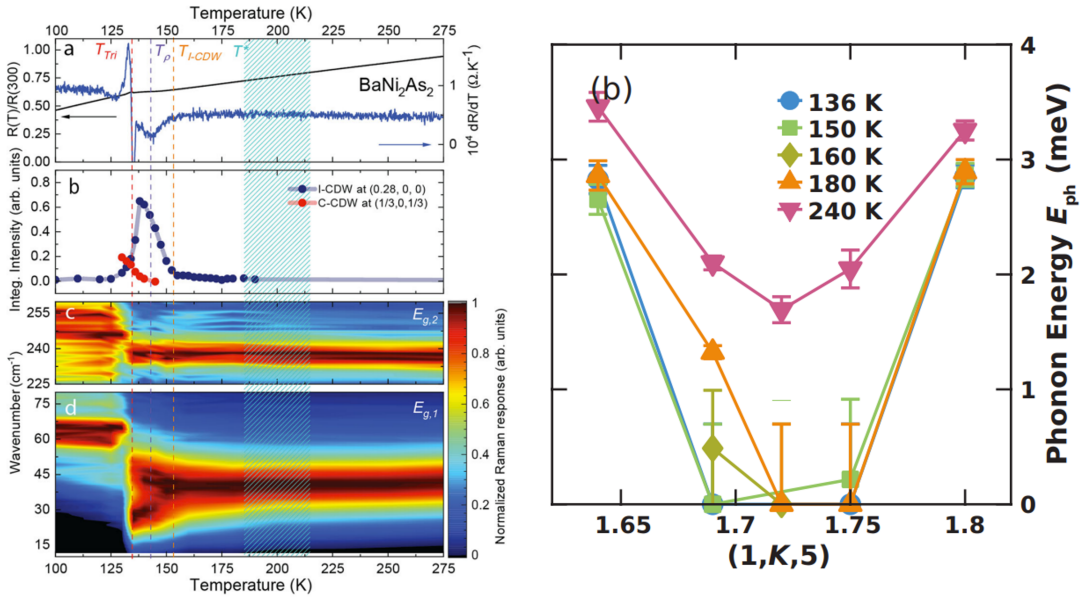

Figure 5.4: Raman measurements and phonon energies of $BaNi_2As_2$ [77].

Given the recent nature of these measurements and lack of addition probes, it is still too early to decimate the origin of charge order in $BaNi_2As_2$.

5.3 Conclusions

In conclusion, I have presented X-ray, and electrical transport measurements showing the evolution of the IC-CDW, C-CDW1, C-CDW2, and triclinic orders in $Ba_{1-x}Sr_xNi_2As_2$. I have shown that the development of the IC-CDW is strongly correlated with a previously reported nematically ordered phase. Additionally, I show an absence of long-range charge order in $Ba_{0.35}Sr_{0.65}Ni_2As_2$ that is consistent with the absence of nematic order at that same composition. The complete charge order phase diagram of $Ba_{1-x}Sr_xNi_2As_2$ helps elucidate the rich evolution of electronic degrees of freedom found in this system.

Additionally, I have presented the pressure and temperature dependence of the charge orders, the triclinic distortion, and the lattice parameters of $BaNi_2As_2$ and have compared them to results found for $Ba_{1-x}Sr_xNi_2As_2$. I find that the four phases, IC-CDW, C-CDW1, C-CDW2, and triclinic order, show slowly declining onset temperatures as a function of pressure until they eventually vanish at higher pressures. I also find that C-CDW2 and triclinic order, the final phases to survive under pressure, vanish discontinuously between 8.4 GPa and 9.5 GPa. At this point in pressure, we find a collapsed tetragonal transition in $BaNi_2As_2$ via an expanding a-axis as measured through powder x-ray diffraction. I speculate that this collapsed tetragonal phase plays a role in extinguishing charge order and enhancing superconductivity plus nematic susceptibility immediately following it. These data continue to present $BaNi_2As_2$ as a rich, non-magnetic superconducting system worthy of study.

For future study, I would first recommend a more through examination of the proposed CT state in $Ba_{1-x}Sr_xNi_2As_2$ and in $BaNi_2As_2$ under pressure near the maximum in T_c in a similar vain to the study shown in Figure 5.2 [85]. While our room temperature lattice constants give strong evidence for a CT phase occurring near the critical point, we lack refinement data that could shed light on the changing Ni-As layer and As-As distance at lower temperatures. More accurate information on the atomic positions may reveal the character of this CT phase and provide clues for why the charge order and triclinic phases discontinuously vanish. Such information could provide further evidence for comparing to the high T_c enchantment found in the iron-pnictides.

As mentioned previously, the iron-pnictides spin state undergoes a spin-state transition [99] and becomes quenched [92] when going through the CT phase. X-ray or neutron

measurements could be performed on the $BaNi_2As_2$ system near the CT phase to check for any abnormal changes to it's spin state.

I also recommend continued investigation into the origin of charge order in $BaNi_2As_2$ beyond what has been seen in Figure 5.4. The IC-CDW is clearly linked to the nematic phase. As demonstrated in Chapter 3, the nematic state likely plays a key in the large T_c enhancement seen. Better understanding of the nematic state could lie with a a better understanding of the IC-CDW order. Meanwhile, the C-CDW2 state is the final charge order to survive until a maximum in T_c is reached. Further investigation into it's origins may provide a link to the CT state and the T_c enchantment.

Bibliography

[1] John Collini, Sangjun Lee, Stella X.-L. Sun, Chris Eckberg, Daniel J. Campbell, Peter Abbamonte, and Johnpierre Paglione. Absence of precursor incommensurate charge order in electronic nematic $\mathrm{ba_{0.35}sr_{0.65}ni_2as_2}$. *Physical Review B*, 106:054107, 2022.

[2] Sangjun Lee, Gilberto De La Penã, Stella X-L Sun, Matteo Mitrano, Yizhi Fang, Hoyoung Jang, Jun-Sik Lee, Chris Eckberg, Daniel Campbell, John Collini, Johnpierre Paglione, FMF De Groot, and Peter Abbamonte. Unconventional charge density wave order in the pnictide superconductor ba(ni1xcox)2as2. *Phys. Rev. Lett.*, 122(147601):147601, 2019.

[3] Sangjun Lee, John Collini, Stella X.-L. Sun, Matteo Mitrano, Xuefei Guo, Chris Eckberg, Johnpierre Paglione, Eduardo Fradkin, and Peter Abbamonte. Multiple charge density waves and superconductivity nucleation at antiphase domain walls in the nematic pnictide ba1xsrxni2as2. *Physical Review Letters*, 127(027602):027602, 2021.

[4] John Collini, Daniel J. Campbell, Daniel Sneed, Prathum Saraf, Christopher Eckberg, Jason Jeffries, Nicholas Butch, , and Johnpierre Paglione. Charge order evolution of superconducting bani2as2 under high pressure. *Manuscript in progress*, 2023.

[5] H Kamerlingh Ones. The resistance of pure mercury at helium temperatures. *Commun. Phys. Lab. Univ. Leiden*, 120, 1911.

[6] W. Meissner and R. Ochsenfeld. Ein neuer eekt bei eintritt der supraleitfahigkeit. *Naturwissenschaften*, 21, 1933.

[7] John Bardeen, Leon Cooper, and Robert Shrieffer. Microscopic theory of superconductivity. *Phys. Rev.*, 106:162, 1957.

[8] J. G. Bednorz and K. A. Muller. Possible high tc superconductivity in the ba-la-cu-o system. *Z. Phys. B*, 64:189–193, 1986.

[9] M. Hirano Y. Kamihara, T. Watanabe and H. Hosono. Iron-based layered superconductor la[o1-xfx]feas (x = 0.05-0.12) with tc=26 k. *J. Am. Chem. Soc.*, 130:3296–3297, 2008.

[10] Michael Tinkham. Introduction to superconductivity. 1996.

[11] Richard A Dunlap. Electrons in solids. 2019.

[12] Temperature variation of electrical resistance of a superconductor. *York department of physics*, 2019.

[13] B. Keimer, S. A. Kivelson, M. R. Norman, S. Uchida, and J. Zaanen. From quantum matter to high-temperature superconductivity in copper oxides. *Nature*, 518:179, 2015.

[14] Andrey Chubukov and Peter J. Hirschfeld. Iron-based superconductors, seven years later. *Physics Today*, 68:179, 2015.

[15] L. Boeri, O. V. Dolgov, and A. A. Golubov. Is lafeaso1-xfx an electron-phonon superconductor? *Physical Review Letters*, 101:026403, 2008.

[16] B. Mansart, D. Boschetto, A. Savoia, F. Rullier-Albenque, F. Bouquet, E. Papalazarou, A. Forget, D. Colson, A. Rousse, and M. Marsi. Ultrafast transient response and electron-phonon coupling in the iron-pnictide superconductor ba(fe1xcox)2as2. *Physical Review B*, 82:024513, 2010.

[17] Wen-Min Huang and Hsiu-Hau Lin. Anomalous isotope effect in iron-based superconductors. *Scientific Reports*, 9:5547, 2019.

[18] R. E. Cohen, W. E. Pickett, , and H. Krakauer. Theoretical determination of strong electron-phonon coupling in yba2cu307. *Physical Review Letters*, 64:2575, 1990.

[19] C. 0. Rodriguez, A. I. Liechtenstein, I. I. Mazin, 0. Jepsen, and 0. K. Andersen. Optical near-zone-center phonons and their interaction with electrons in yba2cu307. results of the local-density approximation. *Physical Review B*, 42:2692, 1990.

[20] K.-P. Bohnen, R. Heid, and M. Krauss. Phonon dispersion and electron-phonon interaction for yba2cu3o7 from first-principles calculations. *Europhysicial Letters*, 64:104, 2003.

[21] T. Dahm, D. Manske, D. Fay, and L. Tewordt. Isotope effect and resistivity in the hubbard model for d-wave superconductivity. *Physical Review B*, 54:12006, 1996.

[22] C.-H. Pao and H.-B. Schuttler. Superconducting instability in the holstein-hubbard model: A numerical renormalization-group study. *Physical Review B*, 57:5051, 1998.

[23] A. Lanzara, P. V. Bogdanov, X. J. Zhou, S. A. Kellar, D. L. Feng, E. D. Lu, T. Yoshida, H. Eisaki, A. Fujimori, K. Kishio, J.-I. Shimoyama, T. Noda, S. Uchida, Z. Hussain, and Z.-X. Shen. Evidence for ubiquitous strong electron–phonon coupling in high-temperature superconductors. *Nature*, 412:510, 2001.

[24] Jinho Lee, K. Fujita, K. McElroy, J. A. Slezak, M. Wang, Y. Aiura, H. Bando, M. Ishikado, T. Masui, J.-X. Zhu, A. V. Balatsky, H. Eisaki, S. Uchida, and J. C. Davis. Interplay of electron–lattice interactions and superconductivity in bi2sr2cacu2o8+. *Nature*, 442:546, 2006.

[25] A. Greco and R. Zeyher. Electronic correlations, electron-phonon interaction, and isotope effect in high-tc cuprates. *Physical Review B*, 60:1296, 1999.

[26] T. Egami. Electron-phonon coupling in high-tc superconductors. 2005.

[27] Alexander Nazarenko and Elbio Dagotto. Possible phononic mechanism for dx2-y2 superconductivity in the presence of short-range antiferromagnetic correlations. *Physical Review B*, 53:2987, 1996.

[28] Miodrag L. Kulić. Possible phononic mechanism for dx2-y2 superconductivity in the presence of short-range antiferromagnetic correlations. *Physics Report*, 338, 2000.

[29] J. Paglione and R. Greene. High-temperature superconductivity in iron-based materials. *Nature Physics*, 6(7538):645–658, 2010.

[30] G. Yu, Y. Li, E. M. Motoyama, and M. Greven. A universal relationship between magnetic resonance and superconducting gap in unconventional superconductors. *Nature Physics*, 5:873, 2009.

[31] S. Lederer, Y. Schattner, E. Berg, and S. A. Kivelson. Enhancement of superconductivity near a nematic quantum critical point. *Physical Review Letters*, 114(097001):097001, 2015.

[32] S. Lederer, Y. Schattner, E. Berg, and S. A. Kivelson. Superconductivity and non-fermi liquid behavior near a nematic quantum critical point. *Proc. Natl. Acad. Sci.*, 114(19):4905–4910, 2017.

[33] Xuetao Zhu, Yanwei Cao, Jiandi Zhang, and Jiandong Guo. Classification of charge density waves based on their nature. *The Proceedings of the National Academy of Sciences*, 112(8):2367–2371, 2015.

[34] Xuetao Zhu, Jiandong Guo, Jiandi Zhang, and E. W. Plummer. Misconceptions associated with the origin of charge density waves. *Advances in Physics X*, 2(3):622–640, 2017.

[35] C. M. Varma and A. L. Simons. Strong-coupling theory of charge density waves. *Physical Review Letters*, 51(2):138–141, 1983.

[36] G. Gruner. The dynamics of charge density waves. *Review of Modern Physics*, 60(4), 1988.

[37] M. D. Johannes and I. I. Mazin. Fermi surface nesting and the origin of charge density waves in metals. *Physical Review B*, 77:165135, 2007.

[38] R.E. Peierls. Quantum theory of solids. page 108, 1955.

[39] Steven H. Simon. The oxford solid state basics. pages 99–107, 2013.

[40] Moritz Hoesch, Alexey Bosak, Dmitry Chernyshov, Helmuth Berger, and Michael Krisch. Giant kohn anomaly and the phase transition in charge density wave zrte3. *Physical Review Letters*, 102:086402, 2009.

[41] C. W. Chu, J. M. E. Harper, T. H. Geballe, and R. L. Greene. Pressure dependence of the metal-insulator transition in tetrathiofulvalinium tetracyanoquinodimethane (ttf-tcnq). *Physical Review Letters*, 1491:121401, 1973.

[42] Kenji Koizumi, Kyoko Ishizaka, Takayuki Kiss, Mario Okawa, Reizo Kato, and Shik Shin. Pressure dependence of the metal-insulator transition in tetrathiofulvalinium tetracyanoquinodimethane (ttf-tcnq). *Journal of the Physical Society of Japan*, 82:025004, 2013.

[43] H. A. Mook and Jr. Charles R. Watson. Neutron inelastic scattering study of tetrathiafulvalene tetracyanoquinodimethane (ttf-tcnq). *Physical Review Letters*, 36:801, 1976.

[44] H. A. Mook, G. Shirane, and S. M. Shapiro. Re-examination of the inelastic neutron scattering in tetrathiafulvalene-tetracyanoquinodimethane (ttf-tcnq). *Physical Review B*, 16:5233, 1977.

[45] Syuma YASUZUKA, Keizo MURATA, Taro ARIMOTO, and Reizo KATO. Temperature-pressure phase diagram in ttf-tcnq: Strong suppression of charge-density-wave state under extremely high pressure. *Journal of the Physical Society of Japan*, 76(3):033701, 2007.

[46] Z. Z. Wang, J. C. Girard, C. Pasquier, D. Jérome, and K. Bechgaard. Scanning tunneling microscopy in ttf-tcnq: Phase and amplitude modulated charge density waves. *Physical Review B*, 67:121401, 2003.

[47] M. H. Lee, C. H. Chen, C. M. Tseng, C. S. Lue, Y. K. Kuo, H. D. Yang, and M.-W. Chu. Concomitant charge-density-wave and unit-cell-doubling structural transitions in dy5ir4si10. *Physical Review B*, 89:195142, 2014.

[48] F. Weber, S. Rosenkranz, J.-P. Castellan, R. Osborn, R. Hott, R. Heid, K.-P. Bohnen, T. Egami, A. H. Said, and D. Reznik. Extended phonon collapse and the origin of the charge-density wave in 2h-nbse2. *Physical Review Letters*, 107, 2011.

[49] D. W. Shen, B. P. Xie, J. F. Zhao, L. X. Yang, L. Fang, J. Shi, R. H. He, D. H. Lu, H. H. Wen, and D. L. Feng. Novel mechanism of a charge density wave in a transition metal dichalcogenide. *Physical Review Letters*, 99, 2007.

[50] T. Valla, A. V. Fedorov, P. D. Johnson, P-A. Glans, K. E. Smith C. McGuinness, E. Y. Andrei, and H. Berger. Quasiparticle spectra, charge-density waves, superconductivity, and electron-phonon coupling in 2h-nbse2. *Physical Review Letters*, 92:086401, 2004.

[51] C. J. Arguello, E. P. Rosenthal, E. F. Andrade, W. Jin, P. C. Yeh, N. Zaki, S. Jia, R. J. Cava, R. M. Fernandes, A. J. Millis, T. Valla, R. M. Osgood Jr., and A. N. Pasupathy. Quasiparticle interference, quasiparticle interactions, and the origin of the charge density wave in 2h-nbse2. *Physical Review Letters*, 114:037001, 2015.

[52] Sajedeh Manzeli, Dmitry Ovchinnikov, Diego Pasquier, Oleg V. Yazyev, and Andras Kis. 2d transition metal dichalcogenides. *Nature Review Materials*, 2, 2017.

[53] Masahiko Yokoi, Satoshi Fujiwara, Tomoya Kawamura, Tomonori Arakawa, Kazushi Aoyama, Hiroshi Fukuyama, Kensuke Kobayashi, and Yasuhiro Niimi. Negative resistance state in superconducting nbse2induced by surface acoustic waves. *Science Advances*, 6, 2010.

[54] D. J. Rahn abd S. Hellmann, M. Kallane, C. Sohrt, T. K. Kim, L. Kipp, and K. Rossnagel. Gaps and kinks in the electronic structure of the superconductor 2h-nbse2 from angle-resolved photoemission at 1 k. *Physical Review B*, 85:224532, 2012.

[55] Yaofeng Xie, Yongkai Li, Philippe Bourges, Alexandre Ivanov, Zijin Ye, Jia-Xin Yin, M. Zahid Hasan, Aiyun Luo, Yugui Yao, Zhiwei Wang, Gang Xu, and Pengcheng Dai. Electron-phonon coupling in the charge density wave state of csv3sb5. *Physical Review Letters B*, 105:L140501, 2022.

[56] J. Tranquada, J. Axe B. Sternlieb, Y. Nakamura, and S. Uchida. Evidence for stripe correlations of spins and holes in copper oxide superconductors. *Nature*, 375:561, 1995.

[57] S. A. Kivelson, I. P. Bindloss, E. Fradkin, V. Oganesyan, J. M. Tranquada, A. Kapitulnik, and C. Howald. How to detect fluctuating stripes in the high-temperature superconductors. *Review of Modern Physics*, 75:1201, 2003.

[58] J. E. Hoffman, E. W. Hudson, K. M. Lang, V. Madhavan, H. Eisaki, and S. Uchida andJ. C. Davis. A four unit cell periodic pattern of quasi-particle states surrounding vortex cores in bi2sr2cacu2o81d. *Science*, 295:466, 2002.

[59] W. D. Wise, M. C. Boye, Kamalesh Chatterjee, Takeshi Kondo, T. Takeuchi, H. Ikuta, Yayu Wang, and E. W. Hudson. Charge-density-wave origin of cuprate checkerboard visualized by scanning tunnelling microscopy. *Nature Physics*, 4:696, 2008.

[60] J. Chang, E. Blackburn, A. T. Holmes, N. B. Christensen, J. Larsen, J. Mesot, Ruixing Liang, D. A. Bonn, W. N. Hardy, A. Watenphul, M. v. Zimmermann, E. M. Forgan, and S. M. Hayden. Direct observation of competition between superconductivity and charge density wave order in yba2cu3o6.67. *Nature Physics*, 8:871, 2012.

[61] R. Comin, A. Frano, M. M. Yee, Y. Yoshida, H. Eisaki, E. Schierle, E. Weschke, R. Sutarto, F. He, A. Soumyanarayanan, Yang He, M. Le Tacon, I. S. Elfimov, Jennifer E. Hoffman, G. A. Sawatzky, B. Keimer, and A. Damascelli. Charge order driven by fermi-arc instability in bi2sr2xlaxcuo6+d. *Science*, 343:390, 2014.

[62] Kazuhiro Fujitaa, Mohammad H. Hamidiana, Stephen D. Edkins, Chung Koo Kima, Yuhki Kohsakae, Masaki Azumaf, Mikio Takanog, Hidenori Takagic, Hiroshi Eisakij, Shin ichi Uchidac, Andrea Allaisk, Michael J. Lawler, Eun-Ah Kim, Subir Sachdevk, and J. C. Séamus Davis. Direct phase-sensitive identification of a d-form factor density wave in underdoped cuprates. *The Proceedings of the National Academy of Sciences*, 111(30):E3026, 2014.

[63] Christopher Eckberg. Superconducting enchantment and electronic nematicity in substituted bani2as2. *University of Maryland, College Park thesis*, 2019.

[64] Jiun-Haw Chu, Hsueh-Hui Kuo, James G. Analytis, and Ian R. Fisher. Divergent nematic susceptibility in an iron arsenide superconductor. *Science*, 337, 2012.

[65] Chris Eckberg, Daniel J Campbell, Tristin Metz, John Collini, Halyna Hodovanets, Tyler Drye, Peter Zavalij, Morten H Christensen, Rafael M Fernandes, Sangjun Lee, Peter Abbamonte, Jeffrey Lynn, and Johnpierre Paglione. Sixfold enhancement of superconductivity in a tunable electronic nematic system. *Nature Physics*, 16:346–350, 2020.

[66] Changyong Park, Dmitry Popov, Daijo Ikuta, Chuanlong Lin, Curtis Kenney-Benson, Eric Rod, Arunkumar Bommannavar, and Guoyin Shen. New developments in micro-x-ray diffraction and x-ray absorption spectroscopy for high-pressure research at 16-bm-d at the advanced photon source. *Review of Scientifici Instruments*, 86:072205, 2015.

[67] W. R. Busing and H. A. Levy. Angle calculations for 3- and 4-circle x-ray and neutron diffractometers. *Acta Crystallographica*, 22, 1967.

[68] M. Lohmeier and E. Vlieg. Angle calculations for a six-circle surface x-ray diffractometer. *Journal of Applied Crystallography*, 26, 1993.

[69] Agnès Dewaele, Marc Torrent, Paul Loubeyre, and Mohamed Mezoua. Compression curves of transition metals in the mbar range: Experiments and projector augmented-wave calculations. *Physical Review B*, 78:104102, 2008.

[70] N. Fujioka, O. Mishima, S. Endo, and N. Kawai. Electrical resistance of manganin under high static pressures. *Journal of Applied Physics*, 49:4830, 1978.

[71] M. J. Clark and T. F. Smith. Pressure dependence of tc for lead. *Journal of Low Temperature Physics*, 32:495, 1978.

[72] Marianne Rotter, Marcus Tegel, Dirk Johrend, Inga Schellenberg, Wilfried Hermes, and Rainer Pöttgen. Spin-density-wave anomaly at 140 k in the ternary iron arsenide bafe2as2. *Physical Review B*, 78:020503, 2008.

[73] K Kothapalli, F Ronning, E D Bauer, A J Schultz, and H Nakotte. Single-crystal neutron diffraction studies on ni-based metal-pnictide superconductor bani2as2. *J Physics: Conf. Series*, 251(012010):012010, 2010.

[74] F Ronning, N Kurita, E D Bauer, B L Scott, T Park, T Klimczuk, R Movshovich, and J D Thompson. The first order phase transition and superconductivity in bani2as2 single crystals. *J. Phys. Conden. Matt.*, 20(34):34, 2009.

[75] N Kurita, F Ronning, Y Tokiaw, E D Bauer, A Subedi, D J Singh, J D Thompson, and R Movshovich. Low-temperature magnetothermal transport investigation of a ni-based superconductor $bani_2as_2$. *Phys. Rev. Lett.*, 102(147004):147004, 2009.

[76] E D Bauer, F Ronning, B L Scott, and J D Thompson. Superconductivity in $srni_2as_2$ single crystals. *Phys. Rev. B*, 78(172504):172504, 2008.

[77] Yi Yao, Roland Willa, Tom Lacmann, Sofia-Michaela Souliou, Mehdi Frachet, Kristin Willa, Michael Merz, Frank Weber, Christoph Meingast, Rolf Heid, Amir-Abbas Haghighirad, Jörg Schmalian, and Matthieu Le Tacon. An electronic nematic liquid in bani2as2. *Nature Communications*, 13:4535, 2022.

[78] S. Lederer, Erez Berg, and Eun-Ah Kim. Tests of nematic-mediated superconductivity applied to ba1xsrxni2as2. *Physical Review Research*, 2:023122, 2020.

[79] Dushyant M. Narayan, Peipei Hao, Rafal Kurleto, Bryan S. Berggren, A. Garrison, Linn, Christopher Eckberg, Prathum Saraf, John Collini, Peter Zavalij, Makoto Hashimoto, Donghui Lu, Rafael M. Fernandes, Johnpierre Paglione, , and Daniel S. Dessau. Lifshitz transition at optimal substitution in nematic pnictide ba1–xsrxni2as2. *Manuscript submitted for review*, 2023.

[80] Agnès Dewaele, Paul Loubeyre, and Mohamed Mezouar. Equation of state of six metals above 94 gpa. *Physical Review B*, 70(094112):094112, 2004.

[81] S. R. Saha, N. P. Butch, J. Magill T. Drye, S. Ziemak, K. Kirshenbaum, P. Y. Zavalij, J. W. Lynn, and J. Paglione. Structural collapse and superconductivity in rare-earth-doped cafe2as2. *Physical Review B*, 85(024525):024525, 2012.

[82] Milton S. Torikachvili, Sergey L. Bud'ko, Ni Ni, and Paul C. Canfield. Pressure induced superconductivity in cafe2as2. *Physical Review Letters*, 101(057006):057006, 2008.

[83] Tuson Park, Eunsung Park, Hanoh Lee, T Klimczuk, E D Bauer, F Ronning, and J D Thompson. Pressure-induced superconductivity in cafe2as2. *Journal of Physics: Condensed Matter*, 20(322204):322204, 2008.

[84] K. Prokeš, A. Kreyssig, B. Ouladdiaf, D. K. Pratt, N. Ni, S. L. Bud'ko, P. C. Canfield, R. J. McQueeney, D. N. Argyriou, and A. I. Goldman. Evidence from neutron diffraction for superconductivity in the stabilized tetragonal phase of cafe2as2 under uniaxial pressure. *Physical Review B*, 81(180506(R)):180506(R), 2010.

[85] J. R. Jeffries, N. P. Butch, K. Kirshenbaum, S. R. Saha, G. Samudrala, S. T. Weir, Y. K. Vohra, , and J. Paglione. Suppression of magnetism and development of superconductivity within the collapsed tetragonal phase of ca0.67sr0.33fe2as2 under pressure. *Physical Review B*, 85(184501):184501, 2012.

[86] Walter Uhoya Andrew Stemshorn Georgiy Tsoi, Yogesh K. Vohra Athena S. Sefat, Brian C. Sales, Kevin M. Hope, and Samuel T. Weir. Collapsed tetragonal phase and superconductivity of bafe2as2 under high pressure. *Physical Review B*, 82(144118):144118, 2010.

[87] R. Mittal, S. K. Mishra, S. L. Chaplot, S. V. Ovsyannikov, E. Greenberg, D. M. Trots, L. Dubrovinsky, Y. Su, Th. Brueckel, S. Matsuishi, H. Hosono, and G. Garbarino. Ambient- and low-temperature synchrotron x-ray diffraction study of bafe2as2 and cafe2as2 at high pressures up to 56 gpa. *Physical Review B*, 83(054503):054503, 2011.

[88] Walter O Uhoya, Jeffrey M Montgomery, GeorgiyMTsoi, Yogesh K Vohra, M A McGuire, Athena S Sefat, Brian C Sales, and Samuel T Weir. Phase transition and superconductivity of srfe2as2 under high pressure. *Journal of Physics Condensed Matter*, 23(122201):122201, 2011.

[89] Ryan L. Stillwell, Xiangfeng Wang, Limin Wang, Daniel J. Campbell, Johnpierre Paglione, Samuel T. Weir, Yogesh K. Vohra, and Jason R. Jeffries. Observation of two collapsed phases in carbfe4as4. *Physical Review B*, 100(045152):045152, 2019.

[90] Gil Drachuck, Aashish Sapkota, Wageesha T. Jayasekara, Karunakar Kothapalli, Sergey L. Bud'ko, Alan I. Goldman, Andreas Kreyssig, and Paul C. Canfield. Collapsed tetragonal phase transition in laru2p2. *Physical Review B*, 96(184509):184509, 2017.

[91] W. T. Jayasekara, U. S. Kaluarachchi, B. G. Ueland, Abhishek Pandey, Y. B. Lee, V. Taufour, A. Sapkota, K. Kothapalli, N. S. Sangeetha, G. Fabbris, L. S. I. Veiga, Yejun Feng, A. M. dos Santos, S. L. Bud'ko, B. N. Harmon, P. C. Canfield, D. C. Johnston, A. Kreyssig, and 2 A. I. Goldman1. Pressure-induced collapsed-tetragonal phase in srco2as2. *Physical Review B*, 96(184509):184509, 2015.

[92] Long Ma, G. F. Ji, J. Dai, S. R. Saha, J. Paglione, and Weiqiang Yu. Quenched fe moment in the collapsed tetragonal phase of ca1-xprxfe2as2. *Chinese Physics B*, 22(5):057401, 2013.

[93] Athena S. Sefat, Rongying Jin, Michael A. McGuire, Brian C. Sales, David Mandrus, Filip Ronning, E. D. Bauer, and Yurij Mozharivskyj. Structure and anisotropic properties of bafe2-xnixas2 (x = 0, 1, 2) single crystals. *Physical Review B*, 79:094508, 2009.

[94] Martin Pfisterer and Günter Nagorsen. Zur struktur ternärer Übergangsmetallarsenide/on the structure of ternary arsenides. *Zeitschrift für Naturforschung B*, 35, 01 1980.

[95] Yucheng Guo, Mason Klemm, Ji Seop Oh, Yaofeng Xie, Bing-Hua Lei, Sergey Gorovikov, Tor Pedersen, Matteo Michiardi, Sergey Zhdanovich, Andrea Damascelli, Jonathan Denlinger, Makoto Hashimoto, Donghui Lu, Sung-Kwan Mo, Rob G. Moore, Robert J. Birgeneau, David J. Singh, Pengcheng Dai, and Ming Yi. Spectral evidence for unidirectional charge density wave in detwinned bani2as2. *arXiv:2205.14339*, 2022.

[96] Nikita S. Pavlov, Timur K. Kim, Alexander Yaresko, Ki-Young Choi, Igor A. Nekrasov, and Daniil V. Evtushinsky. Weakness of correlation effect manifestation in bani2as2: An arpes and lda + dmft study. *Journal of Physical Chemistry C*, 125:28075, 2021.

[97] Yu Song, Shan Wu, Xiang Chen, Yu He, Hiroshi Uchiyama, Baizhuo Li, Saizheng Cao, Jiayu Guo, Guanghan Cao, and Robert Birgeneau. Phonon softening and slowing-down of charge density wave fluctuations in bani2as2. *Physical Review B*, 107:041113, 2023.

[98] S. M. Souliou, T. Lacmann, R. Heid, C. Meingast, M. Frachet, L. Paolasini, A.-A. Haghighirad, M. Merz, A. Bosak, and M. Le Tacon. Soft-phonon and charge-density-wave formation in nematic bani2as2. *Physical Review Letters*, 129:247602, 2022.

[99] H. Gretarsson, S. R. Saha, T. Drye, J. Paglione, Jungho Kim, D. Casa, T. Gog, W. Wu, S. R. Julian, and Young-June Kim. Spin-state transition in the fe pnictides. *Physical Review Letters*, 110:047003, 2013.